Università degli Studi di Napoli "Federico II"

Scuola Politecnica e delle Scienze di Base

Dottorato di ricerca in Scienze Chimiche XXX ciclo

Models and Methods to understand ultrafast dynamics in photochemistry

Ph.D. Student:
Maria Gabriella Chiariello

Supervisor:
Prof. Nadia Rega

Novembre 2017

Summary

The present work of thesis aims at the development of a computational protocol for simulating and interpreting the ultrafast phenomena occurring upon the interaction of molecules with light. Nowadays, thanks to the development of high resolution time resolved spectroscopic techniques we are able to follow photoinduced chemical reactions on the time scale of nuclear motions, and potentially to reveal their coupling with electronic density redistribution.

In this context, time resolved vibrational spectroscopies play a key role; indeed this advanced technique allows for 'watch' nuclear motions of molecules in real time upon excitation, revealing at atomistic level the reaction mechanism triggered by photoexcitation. The resulting experimental spectra are often very complex, and the disentanglement of the information hidden in the signals is not a simple task. In this sense, the atomistic picture provided by theoretical-computational approaches can be an excellent support, not only to establish a direct link between the experimental signal and the molecular motion producing it, but also to reveal what are actually the electronic/nuclear motions at the origin of the photoreactivity. However, the predictive and interpretative ability of a smart theoretical strategy can be exploited to achieve this challenging goal. On this ground, the present Ph.d project has been developed.

One of the most widespread example of photoreactivity is given by the excited state proton transfer reaction (ESPT), which was also deeply investigated by these advanced time-resolved spectroscopic techniques. Generally, ESPT takes place between a so-called photoacid molecule, acting as proton donor, and a solvent molecule, acting as proton acceptor. Within the class of photoacid molecules, Pyranine (8-hydroxypyrene-1,3,6- trisulfonic acid, HPTS) represents a fascinating and particular case (see figure 1a). Pyranine is a commonly used photoacid, showing in water a pKa value of 7 that drops to 0 upon excitation. Pyranine is also a weak photoacid, showing a slower ESPT kinetics when compared to other photoacids. Specifically, in the excited state pyranine donates a proton to a nearby solvent water molecule with time constants of 3 and 90 ps. Previous studies demonstrated that pyranine photoacidity cannot be simply interpreted and explained in terms of the electronic density redistribution responding to the external perturbation. Time resolved vibrational spectroscopy experiments revealed that in the electronic excited state HPTS chromophore undergoes a transient and sequential activation and decay of low fre-

quency (< 1000 cm^{-1}) skeleton modes. This peculiar vibrational activity precedes and apparently promotes the ESPT reactive event. Indeed, these modes seem to play a key role in activating the ESPT, although a direct demonstration of this connection has not been given yet. As first stage of the project, we focused on the photoreactivity of pyranine in pure water solution. In particular, we analyzed the vibrational fingerprints of the photoexcited HPTS in a time window of 0-1000 femtoseconds (fs). To this aim, we adopted an integrated computational approach including ab-initio molecular dynamics (AIMD) to simulate the HPTS in aqueous solution in both the ground and the excited state. As a key tool of our computational strategy, we developed and adopted a time resolved vibrational analysis, based on the wavelet tranform, of the AIMD trajectories. With this approach we will be able to understand whether the photoinduced nuclear rearrangement of the chromophore can be considered the actual driving force of the ESPT reaction.

For the simulation of the solute (HPTS)-solvent (water) system an hybrid explicit/implicit solvation method enforcing non-periodic boundary conditions was adopted. By this approach, it is possible to retain the specific interactions between the solute and the solvent and accurately reproduce the solvent dynamics in proximity of the HPTS molecule. Figure 1a shows our model. The HPTS solute is treated at quantum mechanical (QM) level, while the explicit water molecules are modeled by molecular mechanics. Moreover, in the case of photoactivated nuclear motions of pyranine we deal with collective low frequency modes, probably coupled to the solvent. In this context, the choice of explicit treatment of the solvent effect around the pyranine solute is mandatory. The nuclear photorelaxation of pyranine is finely controlled by the sequential activation of transient vibrational modes. Starting from the photoexcitation, the time window of 1 ps is a suitable time to watch the low frequency modes lifetime. All the modes have a quite complex composition, involving all the molecular skeleton. The wavelet maps reproduce the sequential activation of the main vibrational modes, in fair agreement with the experimental findings. The method employed is able to provide an accurate picture about the time evolution of the photoactivated vibrational modes, matching in all cases the kinetics time constants of the experimental signals. Moreover, they have the key role of optimizing the structural arrangement with the hydrogen bonded water molecule. In particular, some low frequency modes such as the ring breathing mode (190 cm^{-1}), ring out of plane wagging (108 cm^{-1}) or the ring deformation mode (280 cm^{-1}) are involved in modulation of intermolecular distances and orientation with the water solvent molecule hydrogen bonded to phenolic group of pyranine. A rational analysis of the structural parameters involved in ESPT reaction in both ground and excited state, revealed that the hydrogen bond distance between pyranine and the water molecule is optimized in excited state, resulting in a stronger hydrogen bond between the proton-donor acceptor couple. Moreover, the excitation induces the arrangement of the heavy atoms involved in ESPT reaction to oscillate around planarity values, as expressed by the time behavior of two key dihedral angles

($CCOH_{pyr}$ and CCO_{pyr}-O_w).

HPTS chromophore is very sensitive to the environment, and if a base like acetate is present in water solution the reaction became faster (sub-ps). Depending on the acetate concentration, different ESPT mechanisms can be modelled, in particular a direct ESPT reaction from pyranine to acetate is promoted at high concentration of acetate base. Otherwise, one or more intervening water molecules can directly modulate the proton hop from pyranine to acetate. The ESPT reaction involving both *pyranine-acetate* and *pyranine-water-acetate* cluster surrounded by several water shells was investigated.

Five excited state trajectory for simulate the direct ESPT reaction from pyranine to acetate have been collected, employing the same QM/MM recipe (see figure 1b). The excited state proton transfer reaction occurs in sub-ps time scale and it strictly depends on the choice of the starting point. In particular, the solvation around the phenolic oxygen of pyranine and relative orientation of pyranine-acetate are the two factors identified as crucial to accelerate the ESPT reaction.

The excited state proton transfer reaction involving the *pyranine-water-acetate* cluster is an intermediate situation between pyranine in pure water and *pyranine-acetate*. In the first case, before the ESPT event the sequential activation of low frequencies vibrational modes is necessary to induce a structural optimization between the proton donor-acceptor pair. On the other hand for the pyranine-acetate system the reaction is basically barrierless and the nuclear rearrangement is not required. The presence of acetate, for the *pyranine-water-acetate* cluster, obviously makes the ESPT faster, but the central water suggests that low frequencies skeleton modes have to optimize as well the structural arrangement of the reactive site. Ring breathing and out of plane wagging modes have been identified and recognized again as a key modes coupled to the motion of hydrogen bonded water molecule.

The time resolved analysis was extended and tested to study the anharmonic coupling between vibrational modes. In general, a time resolved vibrational signal can have characteristic intensity and frequency oscillations over the time. These oscillations can be ruled and modulated by low frequency vibrational modes. The time behavior of a vibrational signal provides indication about the interactions between normal modes. The case study is represented by a diarylethenes photochromic molecule (see figure 1d), that in excited state undergoes an opening ring reaction. The characteristic intensity oscillations of some vibrational signals appear clearly in the wavelet maps. This suggests an anharmonic coupling with some low frequency modes. In particular, our findings support the idea that the coupling between high and low frequency modes localized on the central cyclohexadiene ring would promote the opening reaction.

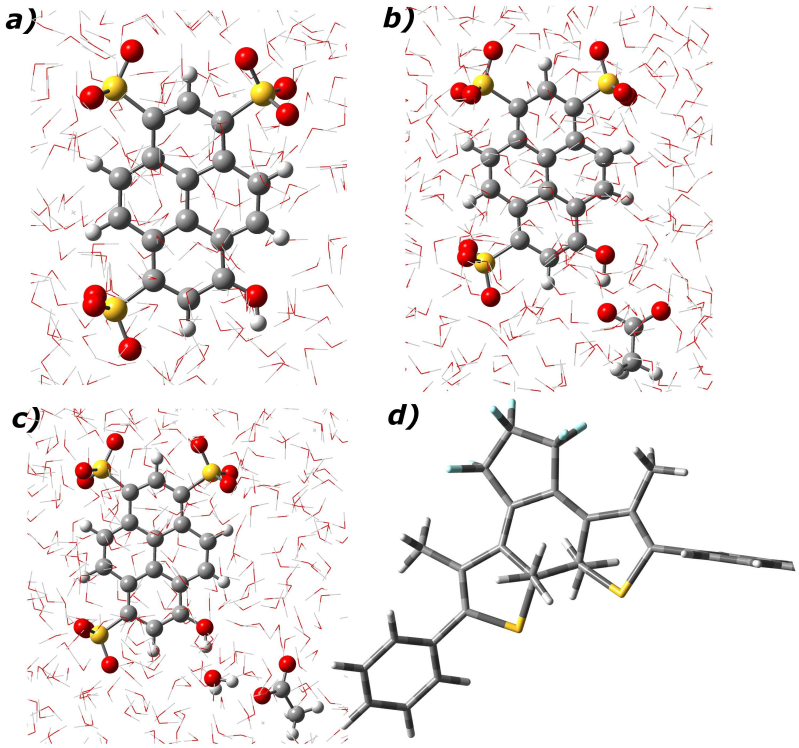

Fig. 1: a) HPTS (or pyranine) chromophore in water solution. The solute (pyranine or HPTS) is treated at quantum mechanical level (ball and stick graphical representation), while the remaining explicit solvent molecules are modeled by molecular mechanics (stick graphical representation). b) *pyranine-acetate* cluster in water solution. The QM region is composed by pyranine and acetate. c) *pyranine-water-acetate* cluster in water solution. The QM region includes in addition a solvent water molecule. d) Structure of 1,2-bis(2,4-dimethyl-5-phenyl-3-thienyl)perfluoro-cyclopentene, a popular diarylethene showing photochromic properties.

Contents

Introduction

The interaction with light can dramatically affect the well-known ground state reactivity of molecules, resulting in an unexpected and almost new photoinduced chemistry [1–8]. That's one of the reasons why the photochemistry is, nowadays, one of the most fascinating and promising research field in chemistry.

Following the photoexcitation, a chromophore lies on higher electronic potential energy surface and it may undergo different pathways. A popular picture of the possible photophysical processes is presented in Figure 2, starting from the absorption of radiation until a de-excitation makes the chromophore drop down to the ground state throughout a radiation or radiationless decay. Indeed, once photoexcited, a chromophore can relax toward the minimum energy structure on excited state surface, or it can react with other photoexcited molecules. Moreover, crossings between electronic surfaces may take place giving rise to the so-called non-adiabatic reactivity [9–11]. A photochemical process can be considered as the result of the electronic and nuclear dynamics responding to the external perturbation, i.e. the photoirradiation with light. These far-for equilibrium dynamics occur on different time scales: the electronic redistribution happens on attoseconds time scales [12–14]

and the subsequent nuclear rearrangement requires instead picoseconds (ps) scales.

Following in real time the photoinduced nuclear dynamics is definitely fundamental to rationalize the structural driving forces at the origin of photoreactivity. Among the approaches turned suitable to this challenge purpose, we mention: the non-linear vibrational spectroscopy techniques [15–17] and the ab-initio molecular dynamic (AIMD) methods [18–20]. The advent of ultrafast pulsed laser techniques has given a new point of view on the photochemistry. In particular, the time resolved vibrational spectroscopies, like the Femtosecond Stimulated Raman Spectroscopy (FSRS) [21–25], allow to *watch* the time evolution of the vibrational modes upon excitation. FSRS was crucial to elucidate the mechanism of photochemical reaction involving chromophore even in complex environment, such as the excited proton transfer reaction (ESPT) of the green fluorescent protein [26–30]. Moreover, the analysis of the oscillating behavior of the time resolved vibrational bands is often performed to unveil the coupling between modes [31]. Otherwise quantitative measure of correlations between vibrational modes can be available by means of the 2-dimentional infrared spectroscopy (2D-IR) experiments [32–35], another non-linear spectroscopic technique providing structural insights such as anharmonicities and coupling between the normal modes.

On the other hand, the interpretative and predictive skills of a smart theoretical-computational protocol based on AIMD are essential to fulfill information that are not accessible to the experiment. By means of AIMD methods the atomistic pic-

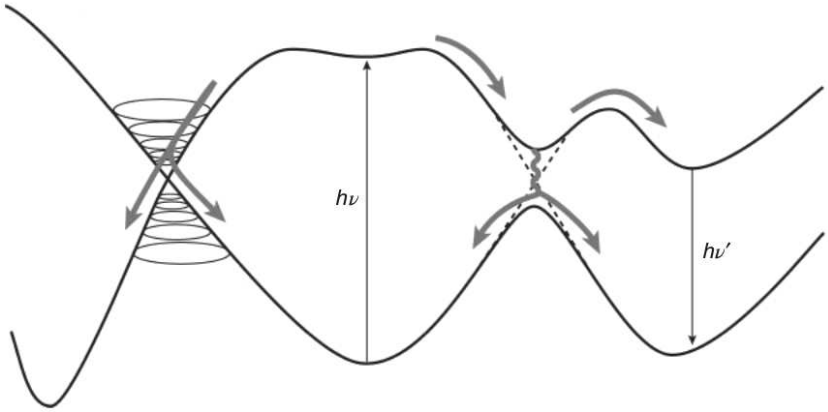

Fig. 2: Schematic representation of the common photophysical processes occruring on excited potential energy surfaces, from [1].

ture is never lost and the molecular response to the photoexcitation is monitored in real time [36–39]. Nevertheless, AIMD has to be combined with a rational vibrational analysis having the ability to keep the temporal information contained in the collected trajectories.

On this ground, the target of this thesis is to provide an integrated theoretical-computational procedure to study the nuclear dynamics of photoexcited chromophores in their realistic environment. The method employed is essentially based on excited state AIMD together with a time resolved vibrational analysis. The molecular systems under investigation relax on excited state potential energy surface (PES), defined on-the-fly by means of an ab-initio electronic potential, which is obtained at time dependent density functional theory (TD-DFT) [40–42] level of theory.

The molecular response to the photoexcitation is carried out by the evolution of the vibrational modes. The standard method to solve the vibrational problem,

based on the diagonalization of the hessian matrix, is not suitable in combination with dynamics simulations. Indeed, it is difficult to be used on large system (like chromophores in solution) and the frequencies generally obtained in the harmonic approximation, even on the excited state equilibrium geometry, do not report about the transient nature of the normal modes. We propose a vibrational analysis completely based on the so-called generalized vibrational modes extracted from dynamics [43, 44]. The method basically involves the analysis of the velocities fluctuations collected in the ground and excited state trajectories. It can be easily applied to large molecular system also when the molecular system is separated according to a quantum mechanics (QM)/ molecular mechanics (MM) hybrid scheme [45, 46].

Because of the transient nature of the vibrational processes triggered by the photoexcitation the computational procedure needs a time resolved analysis tool. To address this issue a multiresolution vibrational analysis based on the *Wavelet Tranform* (WT) [47] was adopted. So far WT has found few but successful applications in chemistry. In partcular, *Wavelet Tranform* was already employed in combination with AIMD simulations to disentagle the evolution of a simulated Stokes Shift [48] or the dipole moment in exciton dynamics [49], and to analyze the evolution of structural parameters in the frequency domain. The simulated vibrational signals can be be plotted in 2-dimention maps where the time and frequency information are both reteined. Following this procedure, a direct comparison with the experimental time resolved signals is therefore possible.

As a first case study to test the developed methodology, the pyranine molecule (8-hydroxypyrene-1,3,6-trisulfonic acid, HPTS) was chosen [50, 51]. HPTS is a popular photoacid chromophore, that found many applications as pH probe and fluorescent tag [52–54] . This kind of molecules upon excitation increases hugely acidity and an ESPT reaction takes place. More closely, pyranine has a pka of 7 in electronic ground state that drops to 0 in excited state, and in water solution where a solvent molecule acts as proton acceptor, the ESPT reaction occurs in 3 and 90 picoseconds [55, 56]. Pyranine is usually identified as weak photoacid [57] because of the comparison with other photoacids molecules, which show ESPT kinetics on sub-ps time scales. Experimental studies revealed how in excited state a sequential activation of low frequencies skeleton modes take place [58–60] . It was hypothesized that they could be essential in promoting the ESPT reaction toward a water solvent molecule.

The second chapter will focus on the transient vibrational features of photoexcited pyranine in pure water. In our model, pyranine chromophore is surrounded by several water shells treated explicitly. It will be shown how a characteristic activation of low frequencies modes can induce structural optimization, involving both the chromophore skeleton and the water of the firs solvation shell, promoting the ESPT reaction. Pyranine chromophore is very sensitive to the environment, and if a base like acetate is present in water solution the reaction became faster (sub-ps) [61]. This will be the subject of the chapter three, where the ESPT reaction between pyranine and acetate is considered. Depending on the acetate concentration, different ESPT

mechanisms can be modelled, in particular a direct ESPT reaction from pyranine to acetate is promoted at high concentration of acetate base. Otherwise, one or more intervening water molecules can directly modulate the proton hop from pyranine to acetate. The ESPT reaction involving both pyranine-acetate and pyranine-water-acetate cluster surrounded by several water shells will be discussed in chapter three. It will be interesting to observe how pyranine vibrational features change when the ESPT reaction become ultrafast.

In last chapter, the time resolved analysis will be extended and tested to study the anharmonic coupling between vibrational modes. In general, a time resolved vibrational signal can have characteristic intensity and frequency oscillations over the time. These oscillations can be ruled and modulated by low frequency vibrational modes. The time behavior of a vibrational signal provides indication about the interactions between normal modes. The case study is represented by a diarylethenes photochromic molecule [62, 63], that in excited state undergo an opening ring reaction. The characteristic intensity oscillations of some vibrational signals appear clearly in the wavelet maps. This suggests an anharmonic coupling with some low frequency modes. It will be discussed how the coupling can promote the open ring reaction. The diarylethenes reactivity is unfortunately recognized to be non-adiabatic and controlled by a crossing between electronic energy surfaces [64]. TD-DFT is not able to provide a complete picture of the whole open ring reaction. The first part of the work was therefore aimed at defining the PES regions, in which the

non-adiabatic coupling is low and the Born-Oppenheimer (BO) approximation still holds. Here, a TD-DFT based dynamics sampling is allowed and employed. For the sake of completeness, a study on a diarylethenes model system, has been conducted with a post Hartree-Fock electronic method [65, 66], in order to characterize the non-adiabatic crossing point between the electronic states.

The next chapter contains the methodological development about the extraction of generalized vibrational modes from dynamics and the wavelet transform based analysis, together with the computational details of the ground and excited state ab-initio dynamics and the hybrid model adopted.

Chapter 1

Trick of the trade: Methods and Models

1.1 Ab-initio molecular dynamics (AIMD)

The molecular dynamics simulations allow for reproducing the behavior of complex chemical and biological system, under equilibrium and far-for equilibrium conditions [67–70]. Understanding the mechanism underling a specific chemical process at molecular level would lead to predict the behavior, driving the experimental and applications studies. The big issue at the heart of any molecular dynamics approach is how to describe the interatomic interactions. The classical molecular dynamics are extremely fast, even when large system like proteins, nucleic acids and molecules in solution are treated. The potential energy ruling the dynamics is usually decomposed in terms of parametrized functions [71–74], accounting for bonded interactions, electrostatic and Van der Waals interactions etc. The potential energy based on parametrized force field are unable to describe processes involving bond braking and formation.

On the other hand, the advent of the ab-initio molecular dynamics was a revolution in the field of computer simulations. Indeed, AIMD combines the accurate ab initio electronic structure theory with the classical molecular dynamics scheme. Within the validity of the Born-Oppenheimer (BO) approximation, the nuclear and electronic degrees of freedom are separated. The basic idea of the ab-initio dynamics scheme relies on the classical simulation of the nuclear motion. The nuclear degrees of freedom are propagated according to the Newton equation of motion. The energies and the forces acting on the nuclei are computed from electronic structure calculation performed on-the-fly at every step of the dynamics trajectory [75, 76].

For solving the electronic structure problem the most used approach are represented by the Kohn-Sham density functional theory [77–79] and the post Hartree-Fock methods [65, 66].

The Born-Oppenheimer, Ehrenfest and Car-Parrinello approaches belong to family of ab-initio molecular dynamics methods.

The Ehrenfest dynamics [80–82] involves to solve the time dependent Schrodinger equation on-the-fly as the nuclear trajectory is propagated according to the classical mechanics. Moreover, Ehrenfest approach accounts for non-adiabatic effects and it allows therefore for investigate reactions, involving non-adiabatic process, i.e. multiple potential energy surfaces.

The BO approach [48, 83–85] is based on the assumption that a single surface rules the dynamics. Energies, gradients and molecular properties are computed on-

the-fly solving the time independent, stationary Schrodinger equation at every step of the nuclei classical propagation. The BO dynamics is less demanding that the Ehrenfest approach, allows for simulate reactions happening on longer time scale (ps).

To overcome the problem of the computational expenses due to the calculation of electronic structure at each step of the molecular dynamics trajectories, the CP approach was developed. In the framework of an extended lagrangian formalism, the electrons are considered as active degrees of freedom propagated as classical particles, with the inclusion of suitable constrains. The CP idea had a huge impact on the field of ab-initio dynamics simulation and it inspired generation of scientists [86–89]. An alternative formalism to the CP is represented by the Atom centered density matrix propagation (ADMP) method. ADMP [90–94] employs atom centered Gaussian basis sets and the single particle density matrix within the extended lagrangian formalism, in place of the plane-wave basis sets chosen as dynamics variables in the CP algorithm.

This family of molecular dynamics methods was widely validated and employed to the study of molecular system in their ground electronic state. Nowadays, many efforts are devoted to found the best dynamics scheme to investigate the electronic excited state.

In this work of thesis, we propose a recipe based on BO dynamics scheme to collect the excited state trajectories, in combination with the time dependent version

of DFT (TDDFT) in linear response formalism [95–97], for solving the electronic structure problem. According to the linear response theory, the excited state wavefunction is not explicitly computed. The energies and the properties of the excited state are obtained by means of the ground reference state to a time dependent perturbation. TD-DFT was remarkably successful at providing an understanding of molecular excited state, with an acceptable computational cost.

In conclusion, for the simulation of the molecules under investigation in their realistic environment the BO/TDDFT dynamics scheme is combined with an hybrid quantum mechanics (QM)/ molecular mechanics (MM) scheme.

1.2 Vibrational Problem from AIMD

The vibrational analysis here employed is a method for obtaining generalized vibrational modes (or quasi-normal or quasi-harmonic) from fluctuations calculated by an AIMD QM/MM simulation [43, 98, 99].

The underling idea is that atomic fluctuations, can be related to an effective force constant matrix relative to the average dynamics structure, from which vibrational modes can be extracted [100, 101]. The effective force constant matrix and the fluctuations matrix are inversely proportional, so that they share the same eigenvectors, i.e. the quasi-harmonic vibrational modes. Moreover, these modes can be different from the standard normal modes, because the anharmonicity effects are naturally taken into account. It is so not required the computation of force constant matrix, but it is sufficient to diagonalize the mass weighted fluctuation matrix to obtain

modes and frequency.

A similar analysis can be carried out in momenta subspace [44, 102, 103] instead of the configuration space. It has been shown that normal mode directions obtained from velocities and coordinate fluctuations are very similar. The assumption is that at any temperature, the 3N generalized modes Q correspond to uncorrelated momenta, and can be obtained by diagonalizing the K matrix of the mass weighted atomic velocities $\dot{q}$ with elements:

$$K_{ij} = \frac{1}{2} < \dot{q}_i \dot{q}_j > \tag{1.1}$$

where i and j run over the 3N atomic coordinates and $< .. >$ indicates an average over the time. Modes velocities can be therefore calculated by projecting atomic velocities along normal-like directions:

$$\dot{Q}(t) = L^{\dagger} \dot{q}(t) \tag{1.2}$$

Finally, the fourier transform (FT) of the $\dot{Q}$ time correlation functions provides the associated frequencies:

$$P(\omega) = \int dt e^{i\omega t} < \dot{Q}_i(t) \dot{Q}_j(t) > \tag{1.3}$$

So far we described what is usually done for an equilibrium analysis. Actually, the aim is investigate far from equilibrium events, specifically the transient vibrational signals appearing upon electronic excitation. We assume that, at least in the

ultrafast part, the L matrix is an acceptable approximation of the vibrational modes composition. Therefore, once the photorelaxation process has been simulated by excited state (ES) trajectories, evolution in the time of Q_{ES} modes are obtained from extracted mass weighted atomic velocities $\dot{q}_{ES}$, according to the transformation

$$\dot{Q}_{ES}(t) = L^{\dagger}\dot{q}_{ES}(t) \tag{1.4}$$

In order to obtain the vibrational frequency values along the time, we adopted a multiresolution vibrational analysis based on the Wavelet Transform (WT) [104]. Here, for the first time, we use WT to obtain transient vibrational signals corresponding to the $\dot{Q}_{ES}(t)$ modes extracted from AIMD. We adopt the continuous WT expression

$$W(a,b) = \int \dot{Q}_{ES}(t)\psi_{a,b}(t)dt \tag{1.5}$$

The time dependent signal $\dot{Q}_{ES}(t)$ is analyzed and decomposed in terms of wavelet basis $\psi_{a,b}$. The details of the wavelet transform are given in next section.

1.3 Time resolved analysis: Wavelet Transform

The Fourier transform performed on a time dependent signal can be seen as a signal decomposition in terms of sine and cosine functions. On the other hand, according to the wavelet transform [47, 104–106], the time dependent signal is decomposed into a set of another kind of basis functions, the wavelets. Recalling the previous

equation:

$$W(a,b) = \int C(t)\psi_{a,b}(t)dt \tag{1.6}$$

where C(t) is a generic time dependent function and $\psi_{a,b}$ are the wavelet basis obtained from a prototype wavelet (called mother wavelet) from dilatation, contraction and translation. As mother wavelet we used the Morlet wavelet, having the form:

$$\psi(t) = \pi^{-\frac{1}{4}} e^{i\omega_0 t} e^{-\frac{t^2}{2}} \tag{1.7}$$

It is basically a plane wave modulated by a gaussian function and ω_0 is the nondimensional frequency, usually taken to be 6 to satisfy the admissibility condition. In figure 1.1, the Morlet wavelet together with the dilated and translated wavelet are shown. The scale parameter a, proportional to the inverse of frequency, regulates the dilatation and contraction of the mother wavelet and extracts the different frequencies hidden in the time-dependent signal. While the translation of the wavelet basis, ruled by the b parameter, ensure the localization of the frequencies in time domain.

The application of the wavelet transform to chemical problem, in particular to far-for equilibrium [48, 49, 107, 108] process is an appealing choice. The far-for equilibrium process, such as the nuclear response to the photoexcitation, are typically transient events, having a lifetime. The far-for equilibrium events give rise to non-

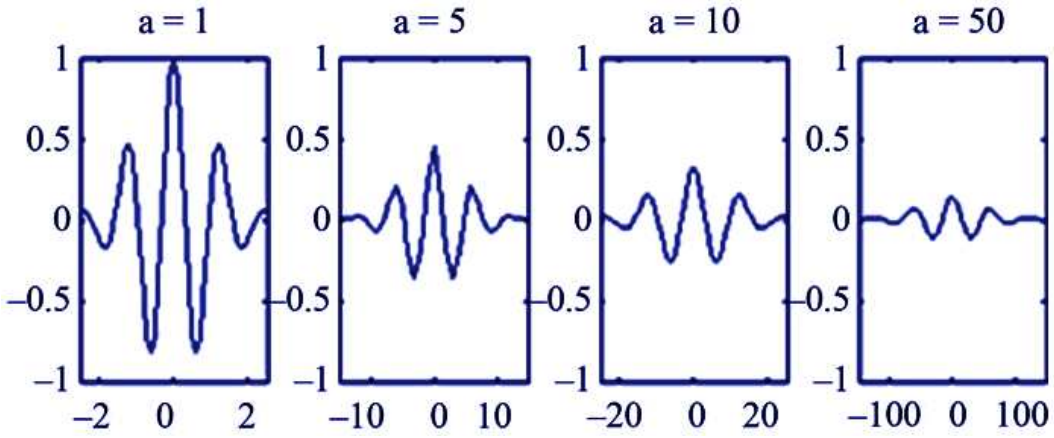

Fig. 1.1: Morlet mother wavelet, with dilated wavelet version.

stationary signals. A non-stationary signal may appear only in a short time interval. Using the FT, this local information is separated into a large number of bases and these signals are averaged over the whole time domain. The FT is not an appropriate tool for the time analysis of the non-stationary signals. The analysis of non-stationary time series should be done localizing the signals in both frequency and time domain. The Short Time Fourier Transform (STFT) [109] could be, in principle, used to this aim. Nevertheless, the STFT employs a time-frequency window, having a fixed width. A time dependent signal can oscillating according to high and low frequencies. The low frequency oscillations should be analyzed by a wide time window, while the high frequency oscillations require a narrow time window. STFT, using a window with fixed width, could be unable to simultaneously detect the high and low frequency of a complex time dependent signal. On the other hand, the WT is characterized by a no-fixed time-frequency window. The time dependent signal, instead, is decomposed into components with different scales [109, 110]. The flexible

time window allows for a simultaneous analysis of the high and low frequencies oscillation, with an acceptable resolution. Thanks to wavelet transform, a complex time dependent signal, even of non-stationary nature can be analyzed and decomposed to obtain the corresponding frequencies. The frequencies are resolved in time, so that it is possible to recognize when the frequency rises and decays. The application to the vibrational modes of photoexcied pyranine, allows us to follow and watch the lifetime of the vibrational modes.

Chapter 2

Following in real time nuclear photorelaxation: pyranine photoacid in aqueous solution

2.1 Introduction to photoacids class: pyranine case

The excited state proton transfer reaction (ESPT) is one of the most widespread example of photoreactivity [111–113]. The absorption of radiation can hugely increase the acidity of particular molecules, called photoacid, which dissociate at the excited state transferring a proton to a nearby solvent molecule or to a strong base present in solution. The understanding of the intermolecular ESPT reaction requires the investigation of several elementary steps composing the overall process. The ultrafast electronic redistribution upon the photoexcitation, the nuclear relaxation, the hydrogen bonds rearrangement and the solvation dynamics finely control the kinetics and thermodynamics of the ESPT event [114,115]. Despite the detailed information provided by the advanced spectroscopic [116–118] techniques, the understanding of the ESPT reactivity at molecular level remains difficult to extrapolated, especially

at the fast and the ultrafast timescale. As a matter of fact, the kinetics of the ESPT toward a solvent molecule covers a wide range of timescales, going from femto- to nanoseconds. Beneath different kinetics there are, of course, different ESPT mechanisms. A classification of the photoacid molecules into four regimes, according to their pKa* values and ESPT rate, was recently proposed [57]. When going from regime I to regime IV the strength of the photoacid and the ESPT increase, while the pKa* value diminishes.

The 8-hydroxy-1,3,6-pyrenetrisulfonate (HPTS or pyranine) is a widely used photoacid [119,120], that found many applications as pH probe and fluorescent tag even in complex biological matrix. Pyranine is usually classified as weak photoacid and it belongs therefore to the first regime. In water, it has a pKa of 7 that drops to 0 upon excitation. Pyranine has a slower ESPT kinetic, compared with other photoacid molecules where the ESPT happens in sub-ps time scales [121, 122].

Specifically, in the excited state pyranine donates a proton to a nearby solvent water molecule with time constants of 3 and 90 ps. Moreover, the photoinduced behavior of HPTS chromophore is very sensitive to change of the environment. In particular, the ESPT reaction is absent when for example methanol is used as solvent [123]. On the other hand, if a base, like acetate, is present in water solution the ESPT kinetic becomes faster (sub-ps time scale) [61]. Acetic acid has a dissociation constant, pKa of 4.76 in the middle of the pKa value of pyranine in ground (pKa 7) and excited state (pKa* 0). At the ground state a spontaneous proton transfer from

pyranine to acetate does not occur, while the electronic excitation should promote a barrierless proton transfer reaction toward acetate.

Pyranine was the subject of several spectroscopic studies, aiming at elucidate the electronic and nuclear mechanisms driving its photoreactivity. In particular, Femtosecond stimulated Raman Spectroscopy [58, 61, 123, 124] was employed to investigate the mechanism of pyranine ESPT in different environmental conditions. The time resolved FSRS spectra in water revealed that in the excited state HPTS chromophore undergoes a transient and sequential activation and decay of low frequency (< 1200) skeleton modes. This peculiar vibrational activity precedes and accompanies the ESPT reactive event, indeed, these modes seem to play a key role in activating and promoting the ESPT.

In this chapter we deal with the nuclear relaxation of photoexcited pyranine in water solution, in particular the time resolved vibrational procedure, based on generalized modes extracted from dynamics and wavelet transform, will be adopted to simulate and interpret the vibrational fingerprint of pyranine in water.

For the simulation of the solute(HPTS)-solvent(water) system, an explicit/implicit solvation method was employed [125–127]. This approach allows to retain the specific interactions between the solute and the solvent and accurately reproduce the solvent dynamics in proximity of the HPTS molecule. Moreover, many of the vibrational modes of interest have a collective nature involving all the four ring aromatic system and they are probably coupled to the solvent molecules directly bound to

phenolic group of pyranine. Modes extracted from dynamics come from the sampling of the molecule in its realistic environment, so these modes naturally take into account of the coupling with solvent explicitelly treated.

The photoacidity weakness of the pyranine can be explain supposing that the electronic re-arrangement over the HPTS chromophore is unable alone to provide the conditions for proton transferring to a water solvent. The nuclear motions responding to the new electronic arrangement has to be considered essential to promote the ESPT reaction. In the nest sections, we will see how the composition and the sequential activation of the characteristic HPTS low frequency skeleton modes trigger a structural optimization with the solvent water molecules (proton acceptor) hydrogen bound to phenolic group of pyranine (proton donor).

2.2 Ground state equilibrium sampling

In order to take into account solvent effects on the photorelaxation of the pyranine chromophore, we adopted an hybrid explicit/implicit solvent scheme within non periodic boundary conditions (NPBC). [125–127] The explicit description of the water solvent molecules is indeed necessary to account for solute-solvent specific interactions, especially those involving the polar (phenolic) and charged (sulfonic) groups of pyranine. Moreover, it has been hypothesized that some low frequencies skeleton modes of photoexcited pyranine play a key role in promoting the excited state proton transfer reaction toward the water molecule that is hydrogen bonded to the phenolic acid group of pyranine. Therefore, the explicit description allows for

the analysis of pyranine vibrational modes that are naturally coupled to the water molecule motions (vide infra).

We start our analysis with the characterization of the solvent microsolvation around the acid group of the pyranine solute, at equilibrium in the ground state. In Figure 2.1 radial distribution functions (RDFs) of the pyranine acid oxygen-water oxygen (O_{pyr}-O_w) and the pyranine acid hydrogen-water oxygen (H_{pyr}-O_w) distances are reported, respectively. In both the cases a well defined peak, corresponding to the first solvation shell around the phenolic acid group, is recognizable. Peaks are centered at around 1.7 and 2.5 Å for H_{pyr}-O_w and O_{pyr}-O_w RDFs, respectively, according to the typical hydrogen bond distances. The first peak is limited by a pronounced minimum in both the RDFs, reaching a zero value for the (H_{pyr}-O_w) RDF. This is a clear indication that there is no exchange of water molecules from and toward the first solvation shell during the sampling period (10 ps). It is noteworthy that the integration number of this peak (black dashed line in Figure 2.1) indicates that one water molecule is hydrogen bonded to the pyranine acid group during the simulation time.

In Figure 2.1 we report the time evolution of the main hydrogen bond structural parameters between the phenolic O-H group of pyranine and the H-bonded water molecule, namely the intermolecular distances H_{pyr}-O_w, H_{pyr}-O_w and the intermolecular angle H_{pyr}-O_{pyr}-O_w. Intermolecular H_{pyr}-O_w and O_{pyr}-O_w distances oscillate around 1.7 and 2.4 Å values, while the H_{pyr}-O_{pyr}-O_w, which reports about

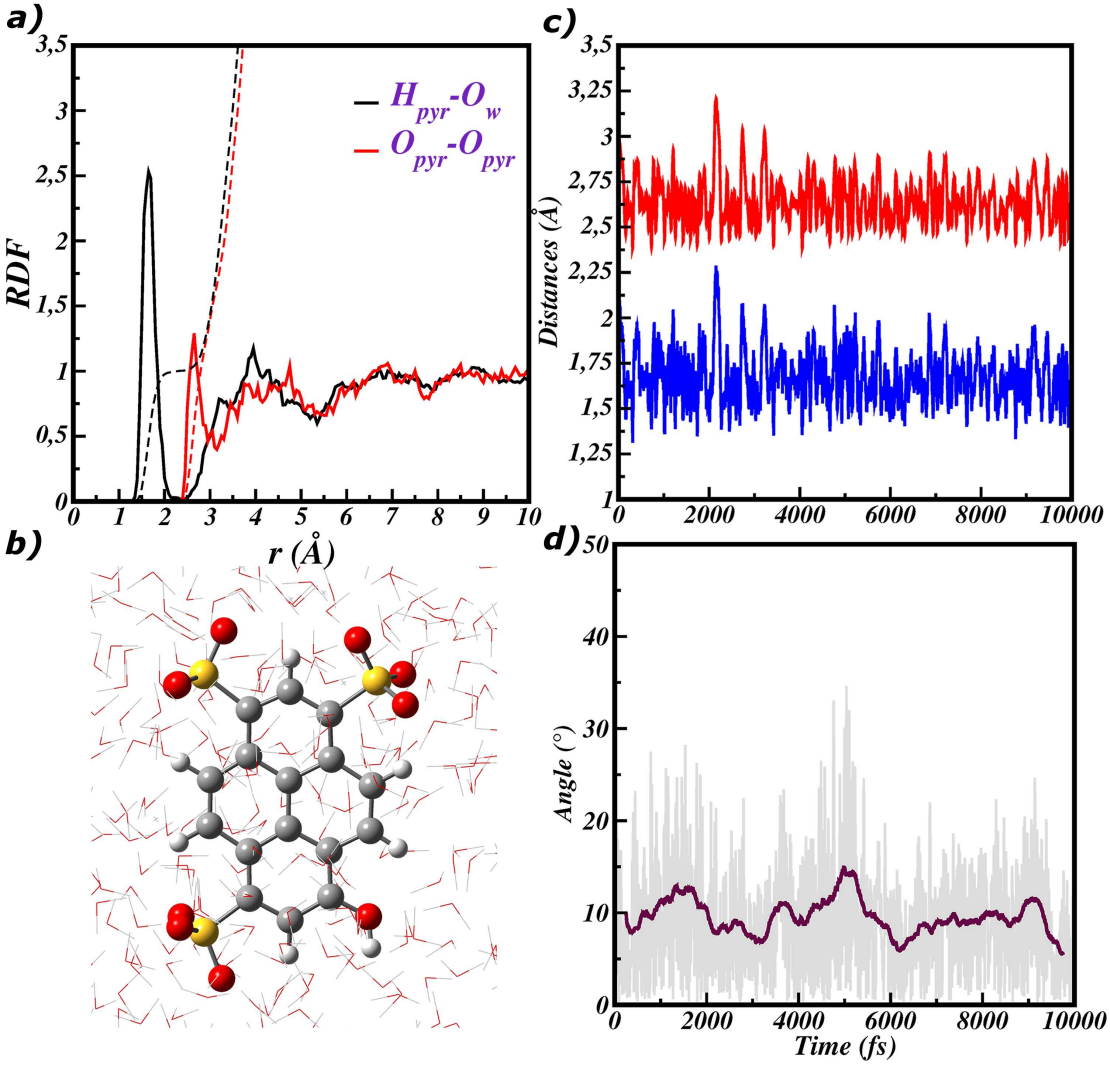

Fig. 2.1: a) H_{pyr}-O_w (black) and O_{pyr}-O_w (red) radial distribution functions b) the pyranine chromophore surrounded by water molecules c) Ground state time evolution of H_{pyr}-O_w (blue) and O_{pyr}-O_w (red) intermolecular distances. d) Ground state time evolution of H_{pyr}-O_{pyr}-O_w angle (grey, the dark line indicates average values over the time).

the orientation of the hydrogen bond, also assumes small values, below 30∘. A strong hydrogen bond between pyranine and water is therefore retained during the whole simulation time.

The resulting solvation layout represents the equilibrium conditions in ground state. A representative configuration of this equilibrium was chosen as starting point for the simulation in the excited state.

2.3 Photoexcited pyranine features

The S_1 excited state of pyranine is obtained from S_0 by a single HOMO-LUMO excitation, with π-$\pi*$ character. Contours of the involved frontier orbitals are shown in Figure 2.2, as obtained by a TD-DFT calculation on the ground state energy minimum of the HPTS molecule, including solvent effects in implicit way according the polarizable continuum model in its conductor-like version.

From a simple inspection of HOMO and LUMO contours, we note that the charge transfer character of the transition is low, also in proximity of the acid group. That means, the depletion of electronic density on the acid group associated to the electronic transition is not able alone to induce an immediate dissociation of the proton, as it can be expected from the weak photoacidity of pyranine. Instead, upon the excitation an electronic redistribution occurs over the whole nuclear skeleton, involving an exchange of alternating bond order among C-C bonds. In particular, the overall reorganization mainly corresponds to the π electronic density depletion on C-C bonds aligned with the red arrows shown in Figure 2.2, while the π electronic

density on C-C bonds that are almost perpendicular to the red arrows increases when going from the ground to excited state.

Therefore, we can expect a C-C elongation (lowering of the bond order) and a C-C shortening (increasing of the bond order) in the first and second case, respectively, when going from the ground to excited state. Overall, the excitation leads to the lengthening of the whole molecule along the axis approximately aligned with OH bond.

We investigated the photoinduced relaxation of the pyranine rings by comparing the evolution in S_0 and S_1 of the same initial configuration (coordinates and momenta) for about 1 ps. We then analyzed the time relaxation of C-C bonds in the excited state in the frequency domain by means of the wavelet analysis.

In Table 2.1 we report average values of C-C distances calculated from AIMD trajectories in the ground and the excited state. As expected, upon the excitation we observe elongation of up to 0.04 Å for C-C bonds 1, 3, 5, 6, 8 and 10, and a shortening of about 0.02 Å for the remaining ones.

As an example, in Figures 2.3a and 2.3c we show the time evolution in both the ground and the excited state of 1 and 2 C-C distances, which in the excited state become longer and shorter respectively. We can recognize how the C-C 1 distance in the excited state oscillates around greater values when compared to the corresponding evolution in the ground state. An opposite behavior is instead

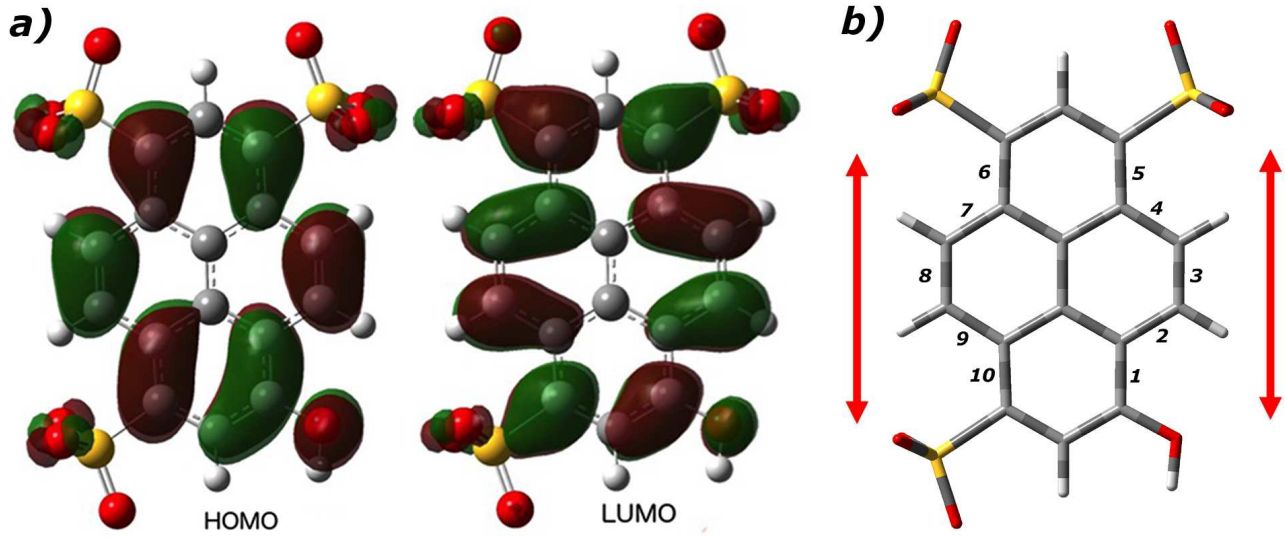

Fig. 2.2: a) HOMO-LUMO contours of pyranine computed at B3LYP/6-31g(d,p)/C-PCM level of theory. b) Labels used to tag C-C bonds analyzed in the present work.

C-C bond	S_0 average distance	S_1 average distance
1	1.41	1.44
2	1.43	1.41
3	1.36	1.40
4	1.44	1.42
5	1.42	1.45
6	1.42	1.44
7	1.44	1.42
8	1.36	1.39
9	1.44	1.42
10	1.41	1.44

Table 2.1: Average C-C distances (Å) obtained from AIMD simulations of pyranine in aqueous solution in the ground and the first singlet excited state. Standard deviations are 0.02 Å and 0.03 Å for S_0 and S_1 trajectories, respectively. See Figure 4.2 for the numbering of C-C bonds.

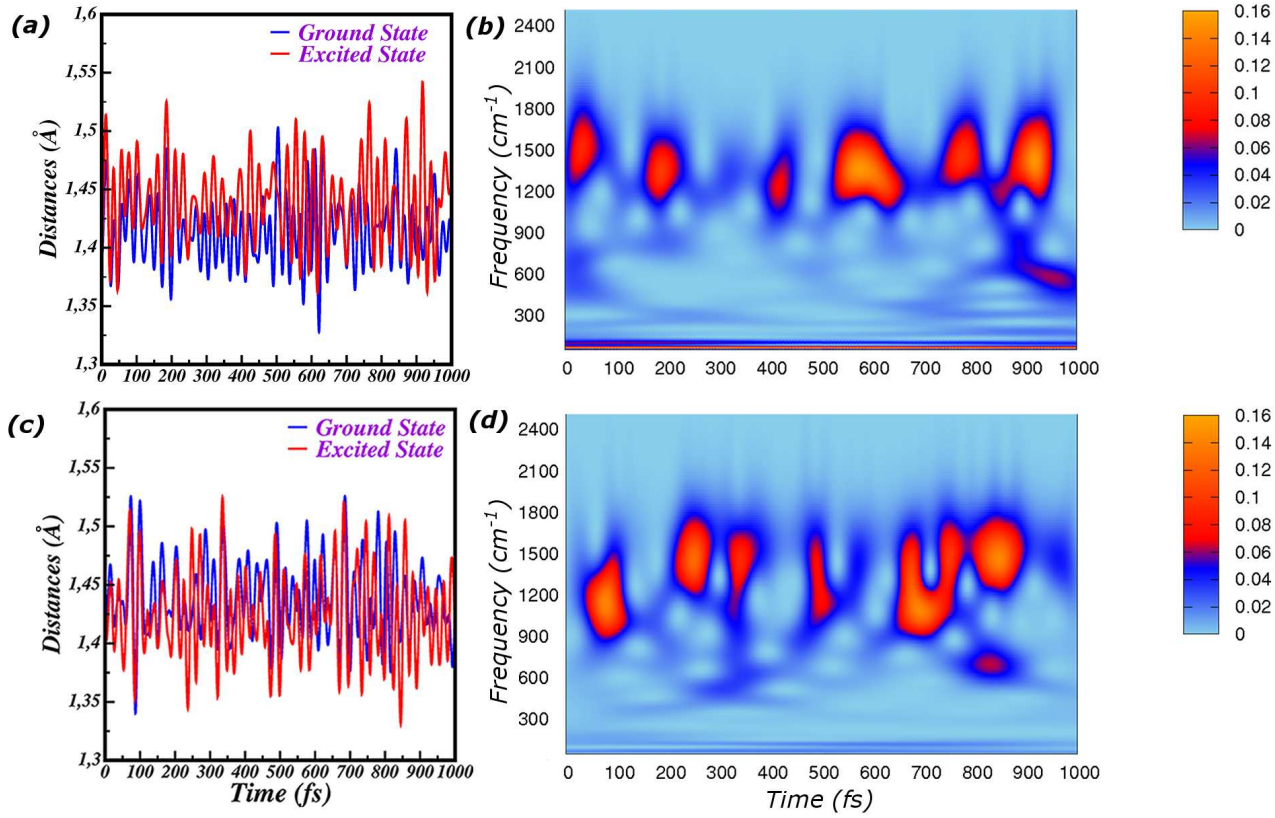

Fig. 2.3: a) Ground (blue) and excited (red) state time evolution of the C-C 1 distance. b) 2D wavelet map of the C-C 1 distance in excited state. c) Ground (blue) and excited (red) state time evolution of the C-C 2 distance. d) 2D wavelet map of the C-C 2 distance in excited state.

observed for the C-C 2 distance.

Time resolved vibrational analysis in the excited state of C-C bonds 1 and 2 have been perfomed by computing corresponding wavelet spectra, which are reported as time-frequency 2-dimentional maps in Figures 2.3b and 2.3d, respectively.

From inspection of Figure 2.3 several interesting features of the pyranine photoinduced vibrational dynamics can be inferred. In the ultrafast part of the relaxation, namely for times below 100 fs after the excitation, signals associated to the C-C distances 1 and 2 are centered around 1500 and 1200 cm^{-1} respectively, i.e. around

values close to those adopted in the ground state. Then, clear blue and red shifts are observed in the two cases, testifying an exchange of force constants associated to the two bonds. Notably, the overall relaxation toward values adopted in the excited state takes about 500 fs to complete. This time is in nice agreement with what observed by FSRS experiments, indicating about 600 fs as the time necessary to carry out most of the pyranine relaxation on the excited potential energy surface. [58, 124]

Another important observation regards the evolution of the intensity of both signals. Indeed, the vibrational dynamics shows a clear oscillatory behaviour. In particular, periods between intensity maxima strongly suggest that the pyranine skeleton relaxation is modulated by low frequency modes (below 200 cm^{-1}), possibly collective ring modes, which accompany the electronic redistribution of the molecule, and the consequent rearrangement of forces among nuclei.

Moreover, the C-C 1 and 2 vibrational bands are almost out of phase, indicating that rearrangement of forces in bonds with alternating order are anticorrelated in the time. A similar oscillatory and out of phase trend has been already experimentally observed in the photorelaxation of C-O and C-N stretching modes of the Green Fluorescent Protein chromophore. [26] Therefore, our results also suggest that the anticorrelated relaxation modulated by collective low frequency modes could be a common motif in photoinduced vibrational dynamics of aromatic or conjugate systems.

2.4 Vibrational fingerprint of pyranine

The pyranine ESPT reaction involves the motion of the proton from the photoacid molecule to a solvent molecule of the first solvation shell, and from here to the bulk through the diffusion process along hydrogen bond networks. The first and essential step, even before the proton hopping, is the formation of a tight proton donor-acceptor couple, i.e. the photoexcited pyranine and an hydrogen bonded water molecule.

Upon excitation, the pyranine molecule undergoes a remarkable vibrational dynamics. FSRS results highlighted a characteristic and transient Raman activity in the excited state, associated to the sequential activation of low frequency vibrational modes. Several efforts have been made in order to individuate, among the complex sequence of activation/decay of vibrational signals, possible driving forces for the pyranine photoacidity. It has been hypothesized that low frequencies skeleton modes of photoexcited pyranine play a key role in promoting the excited state proton transfer reaction toward the water molecule hydrogen bonded to the phenolic acid group.

Here, we analyzed the structural rearrangement involving the pyranine and the water molecule hydrogen bonded to the acid O-H group. Moreover, we individuated the generalized normal modes that are mainly involved in the pyranine-water relaxation, and analyzed their vibrational dynamics in the excited state.

As already mentioned in models and methods section the modes composition is

obtained by the equilibrium sampling, according to equation 1.2 and they are shwon in figure 2.4 and 2.5. The time dependent signal that account for the vibrational photorelaxation on which the wavelet transform is performed, is instead obtained from equation 1.4. The left colum of figure 2.4 and 2.5 depict the corresponding 2D wavelet maps.

The three vibrational modes shown in figure 2.4, have a collective nature, involving the motion of the whole four ring aromatic system. In particular, the mode associated to the frequency of 900 cm^{-1} is an in plane ring deformation with a strong hydrogen out of plane component (see figure 2.4). In figure 2.4 b is depicted the 310 cm^{-1} mode, which it's again an in plane ring deformation, but it's also composed by a phenolic -COH rocking component. Lastly, the lowest frequency mode (figure 2.4 c) is described as a symmetric skeletal breathing mode, experimentally found at 191 cm^{-1}. This is an in plane collective mode engaging all the 4-aromatic rings. The breathing mode basically entails the lengthening of the whole molecule, pushing the phenolic acid group toward the proton acceptor, i.e. the hydrogen bonded water molecule.

The wavelet maps, obtained according to equation 1.4, are plotted in a frequencies ranges of 0-1800 cm^{-1} and 0-1400 cm^{-1}, respectively for the 900 and 310 cm^{-1} modes and for 191 cm^{-1} mode, because at higher frequencies there are not signals of considerable intensity.

The deformation mode at 900 cm^{-1} starts to rise a little bit after the electronic

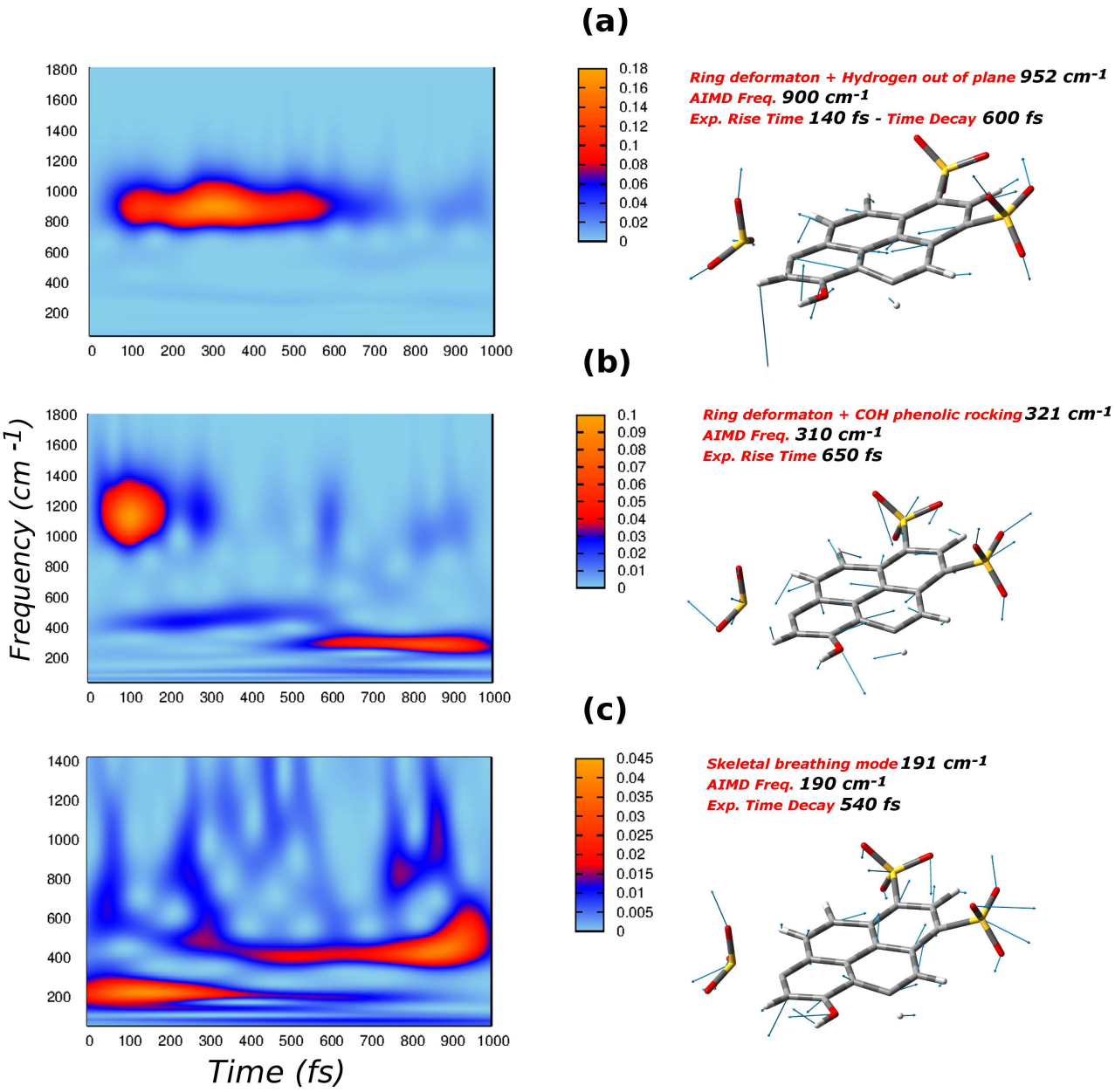

Fig. 2.4: Q modes (right panels) and corresponding 2D wavelet power spectra (left panels). a) Ring deformation mode combined with hydrogens out of plane motion, with an AIMD frequency of 900 cm^{-1}; b) Ring deformation modes associated to a strong -COH phenolic rocking, the AIMD frequency is 310 cm^{-1}; c) Skeletal breathing mode, with AIMD frequency of 190 cm^{-1}

excitation, at about 100 fs and the wavelet spectrum shows a decay at the time of 600 fs. This behaviour is in perfect agreement with the experimental evidences of kinetics costants of 140 fs (rise) and 600 fs (decay) [58].

The wavelet spectrum of the 310 cm^{-1} deformation mode, depicted in figure 2.4 , also shows interesting features. The signal at 310 cm^{-1}, associated to the deformation mode with experimental frequency of 321 cm^{-1}, appears at the time of 600 fs, well reproducing again the experimental rise time of 650 fs [58]. Another main signal is instead centered around 1100 cm^{-1}. That's basically the -COH phenolic rocking mode, experimentally found at 1138 cm^{-1} [58]. The 310 cm^{-1} mode , is overall composed by a four rings collective deformation, associated to a strong phenolic -COH motion. Nevertheless, the -COH rocking mode alone is located at 1138 cm^{-1}. In other words, the 310 cm^{-1} mode is also composed by phenolic -COH rocking and if one considers this motion alone, it has a frequency of 1138 cm^{-1}. During the dynamical simulation, the sampling of the 310 cm^{-1} mode involves naturally also the -COH rocking motion, so that the wavelet spectrum ends up to show both the frequencies at 310 cm^{-1} and 1138 cm^{-1}.

Lastly, in figure 2.4 , the wavelet spectrum of the lower frequency ring breathing mode is shown. It's quite easy to recognize a component below 200 cm^{-1}, associated to the breathing mode. Following the electronic excitation, this mode quickly starts to rise and decays before 600 fs. This feature is in excellent agreement with the spectroscopic experimental signal, showing a decay time constant for this mode of

540 fs [58]. In addition the spectrum shows another important band appearing at about 500 fs and centered around 450 cm^{-1}. This latter signal can be associated to a mode experimentally found at 460 cm^{-1}, with a risetime of 600 fs [58].

The mode at 456 cm^{-1} is similar to the breathing mode in terms of collective motion of the 4-aromatic rings system. The dynamical simulation made possible to sample and isolate the 191 cm^{-1} breathing mode, that is naturally and sequentially coupled to the 460 cm^{-1}. In the excited state wavelet spectrum the frequencies are resolved in time, and we can see how the 460 cm^{-1} mode appears simultaneously to the breathing decay, qualitatively reproducing the experimenatal risetime of 600 fs.

The method employed is able to provide an accurate picture about the time evolution of the photoactivated vibrational modes, matching in all cases the kinetics time constants of the experimental signals. Beyond that, it's noteworthy that the sequential trend with which the modes vanish and appear, is in perfect agreement with the experimental one. In case of photoexcited pyranine, the time window of 0-600 fs is clearly a key time in the context of the overall relaxation process. Indeed, that's the time in which the decay of the 190 and 900 cm^{-1} modes and the rise of 310 and 460 cm^{-1} modes, happens simultaneously.

A deeper analisys of the composition of these three modes shows how all of them have important contribution localized to the phenolic acid group. In particular while for the lower frequency modes (190 and 310 cm^{-1}), these are basically -COH phenolic rocking motion, the 900 cm^{-1} mode has a clear phenolic hydrogen out of

plane contribution. As vibrational modes are exctracted from dynamics trajectory, where the water solvent molecules are explicitly take into account, it's possible that they are coupled to the motion of the solvent in first solvation shell. More closely, during the simulation time we found that just one water molecule remains close, hydrogen bonded, to the acid group of pyranine, i.e. there is no exchange of water molecules between the solvation shells around the pyranine phenolic group.

In figure 2.6 we compare the time evolution in the ground and the excited state of the intermolecular distances between the pyranine phenolic oxygen and the H-bonded water oxygen (O_{pyr}-O_{wat}), and between the pyranine acid group hydrogen the water oxygen (H_{pyr}-O_{wat}). It can be noted that in the excited state these distances are shorter since about 50 fs, indicating that the phototriggered relaxation induces a tighter arrangement of the proton donor-acceptor couple. It is interesting also to observe in the frequency domain the trend shown by the H_{pyr}-O_{wat} distance as extracted from the excited state trajectory. Indeed, the wavelet spectrum in Figure 2.6 of the H_{pyr}-O_{wat} distance shows a band around 180 cm^{-1} that is activated in the ultrafast part of the spectrum, with a time decay of about 400 fs.

A pyranine low frequency mode photoactivated at about 280 cm^{-1} has been extensively investigated by FSRS techniques, and an important role played in promoting the pyranine photoacidity has been pointed out. [58,124] Here, we extracted a collective deformation mode involving all the 4-rings of the molecule with an important contribution from the phenolic O-H stretching. It is reasonable to expect,

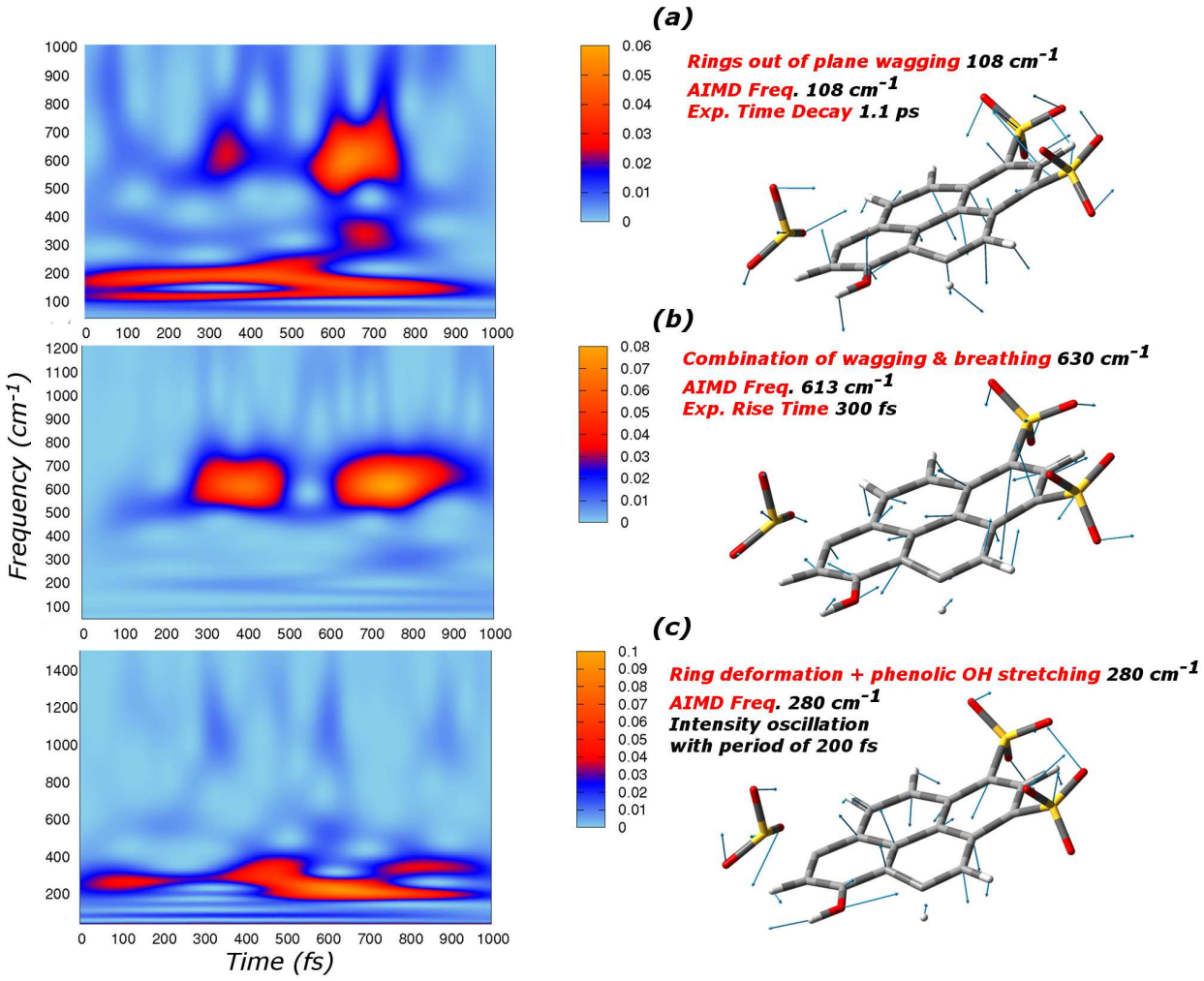

Fig. 2.5: Q modes (right panels) and corresponding 2D wavelet power spectra (left panels). a) Ring out of plane wagging mode, with an AIMD frequency of 113 cm^{-1}; b) Combination of wagging and breathing mode r, the AIMD frequency is 613 cm^{-1}; c) Ring deformation associated to a phenolic OH stretching component, with AIMD frequency of 280 cm^{-1}

therefore, that the activation of this band is mainly responsible of the early tightening of the pyranine-water couple. Composition of the mode and corresponding wavelet spectra in the excited state are reported in Figure 2.5 c.

The vibrational dynamics shown by this mode is quite involved. We observe a signal at about 280 cm^{-1} appearing in the ultrafast time of the pyranine relaxation, showing several raise and decay episodes with constant times of about 200 fs. Moreover, another strong band very close in frequency appears at about 500 fs.

In Figure 2.7 we show the time evolution in both ground and excited state of dihedral angles involving the O-H phenolic group of pyranine and the H-bonded water molecules, namely the CCOH and the CCOO angles shown. These structural parameters describe the relative orientation between the photoacid and the H-bonded water molecule.

We observe that in the excited state (red lines in Figure 2.7) both angles oscillate around values lower than in the ground state. In both cases, average values become close to 180°. Therefore, the excitation induces a more planar arrangement of the pyranine-water molecule, which is more suited for the proton transfer. Importantly, at variance of the ground state evolution, oscillations of these dihedral angles in the excited state are modulated by a low frequency mode, which we can individuate at about 108 cm^{-1} from time periods between maximum values.

From AIMD of pyranine in water we extracted a collective four ring out of plane mode of the pyranine, involving in particular the out of plane motion of the O-H

group. In Figure 2.5 a we report the composition of the mode and the corresponding wavelet spectra calculated in the excited state. Also in this case the spectrum is quite complex. The lowest frequency component is indeed at 108 cm^{-1}, and it is active along the time window of 1 ps. Along the time, however, coupling to bands at about 190, 300 and 600 cm^{-1} can be observed. Notably, a similar mode is experimentally found at 108 cm^{-1}, with a decay time constant of about one ps.

The wavelet map in Figure 2.5 a shows an other important contribution coming from the band centered at about 600 cm^{-1}. It was associated to a mode that has in plane and out of plane features, experimentally described as 'combination of wagging and breathing' [58]. The combination mode was isolated alone and its composition is shown in figure 2.5 b , with the corresponding wavelet map on the left panel. The AIMD frequency of 613 cm^{-1} is in nice agreement with the experimental one at 630 cm^{-1} and the experimental rise time of 300 fs is also well reproduced in 2D wavelet map.

In summary, we observe a structural reorganization of the couple formed by the pyranine and the H-bonded water molecule in the first picosecond of the photoinduced relaxation. Both intermolecular distances and relative orientation are more favorable for the future proton transfer. From our analysis, this rearrangement is mainly modulated by two low frequency skeleton modes at 108 cm^{-1} and 280 cm^{-1}, affecting the water orientation and proximity, respectively. The importance of the mode at 280 cm^{-1} has been already experimentally revealed, while the role played

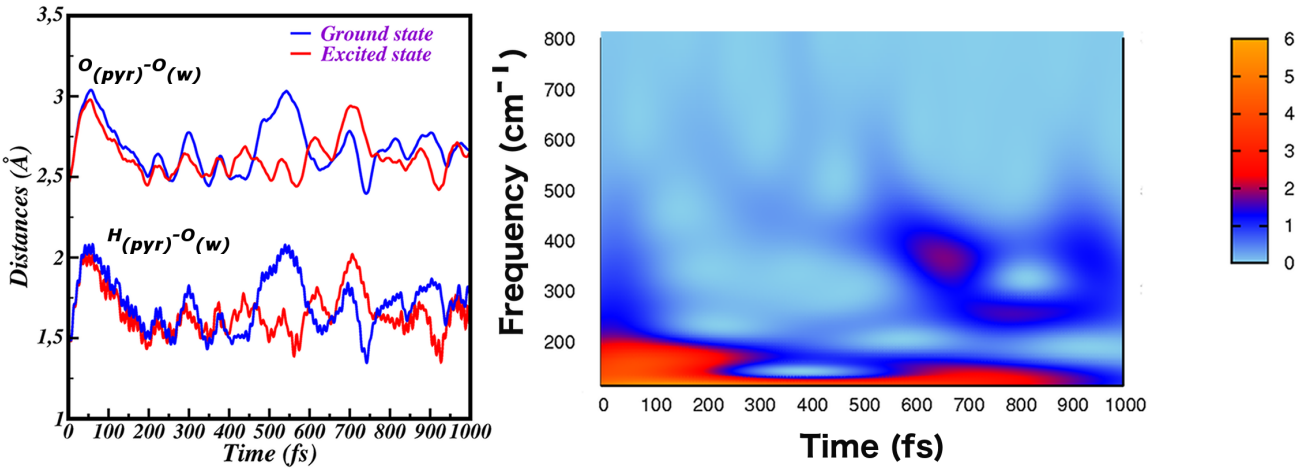

Fig. 2.6: Left panel: Time evolution in both the ground (blue) and excited state (red) of the intermolecular distances between pyranine and water of the first solvation shell, H_{pyr}-O_w and O_{pyr}-O_w. Right panel: 2D wavelet map of the intermolecular H_{pyr}-O_w stretching in excited state.

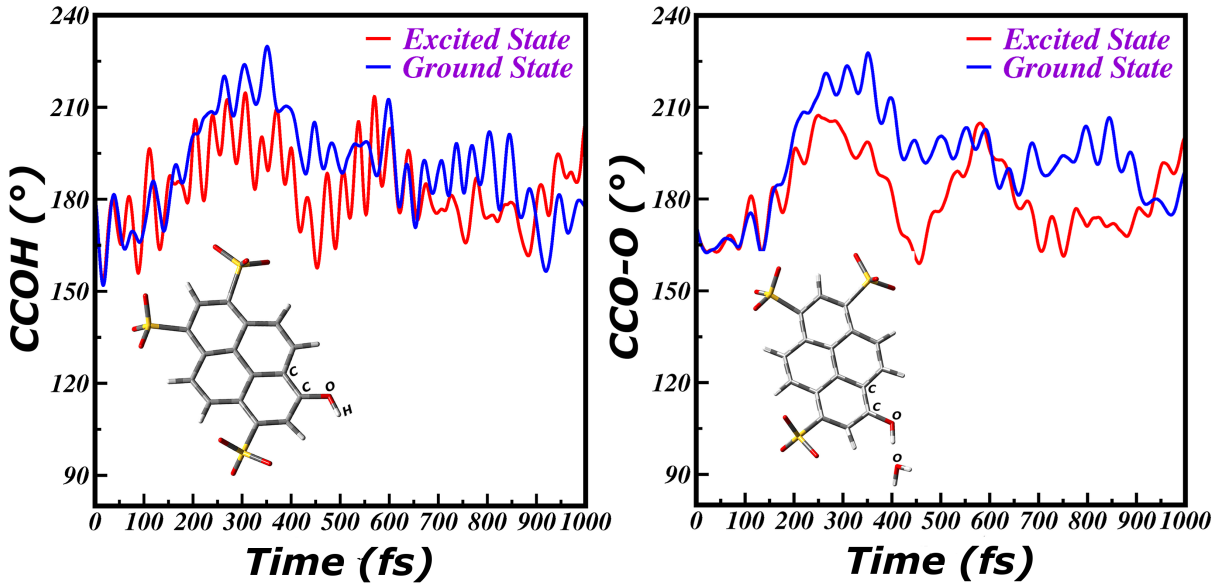

Fig. 2.7: Comparison between the ground (blue lines) and excited (red lines) state behaviour of the CCOH (left panel) and the CCOO (right panel) dihedral angles.

by the vibrational mode at 108 cm^{-1} is proposed here for the first time. Indeed, this mode appears to be essential in the proton donor acceptor couple rearrangement that is preparatory for the photoreactivity.

Within the class of photoacid molecules, pyranine is classified as weak. Indeed, the origin of pyranine photoreactivity cannot be simply interpreted and explained in terms of the electronic density redistribution responding to the external perturbation. On the other hand, nuclear dynamics turns out to be preparatory and essential in promoting the ESPT reaction.

Our findings support the hypothesis that the nuclear photorelaxation of pyranine is finely controlled by the activation of transient vibrational modes at low frequency. The most important stage of the skeleton relaxation is completed in about 500 fs, in agreement with FSRS data. In particular, the exchange of the order among C-C bonds occurs according to a complex vibrational dynamics, showing oscillatory patterns that are out of phase and modulated by modes below 200 cm^{-1}.

We also individuated modes playing a role in optimizing the structural rearrangement of the pyranine and water molecule hydrogen bonded to the O-H group. In particular, a ring out of plane wagging (108 cm^{-1}) and a ring deformation mode (280 cm^{-1}) support the rearrangement of the intermolecular orientation and distances. As a consequence of the ultrafast relaxation, the pyranine-water couple is tighter and better oriented for the ESPT, occurring at later times.

Chapter 3

Exploring excited state reactivity of pyranine-acetate system in aqueous solution

3.1 Introduction to pyranine photoreacitivity in presence of acetate

The pyranine molecule is classified as weak photoacid. It is acknowledged that in water solution HPTS chromophore transfers a proton to a water solvent molecule at the excited state, with time constants of 3 and 90 ps [58]. Analysis of the frontiers orbitals involved in the interested electronic transition, HOMO-LUMO, showed how the whole charge transfer character is not significant, especially around the phenolic acid group. This means that the main driving force of the ESPT process should not be ascribed to the electronic redistribution triggered by photoirradiation, but rather the nuclear response to the new electronic arrangement must be considered fundamental. In the previous chapter we showed how some photoactivated normal modes are crucial to induce a structural optimization with the water molecule of the

first solvation shell. The pyranine ESPT rate is very sensitive to the environment. For example in methanol the ESPT is inhibited [123]. Nevertheless, if a base, like acetate, is present in water solution the ESPT kinetic becomes faster (sub-ps time scale) [61]. Acetic acid has a dissociation constant pKa of 4.76 between the pKa value of pyranine in the ground (pKa 7) and the excited state (pKa 0). Modeling this kind of reaction is not a simple task, because different ESPT mechanism could be hypothesized depending on the acetate concentration. In particular, a direct ESPT from HPTS to acetate molecule could be considered at high acetate concentration. Otherwise, the ESPT could involve one or more intervening water molecules between the proton donor (pyranine) and the final proton acceptor (acetate). Both the direct and indirect (modulated by one water molecule) ESPT have been considered here. The absorption spectra (404 nm) of the neutral HPTS does not change in presence of acetate, and the electronic transition has the same $\pi - \pi*$ character of the HPTS chromophore in water solution. In order to get a first insight about the PES(s) involved in ESPT process, constrained energetic profiles were computed in both ground and excited state to model the following reactions:

$$HPTS + CH_3COO^- \longrightarrow PTS^- + CH_3COOH$$

$$HPTS + H_2O + CH_3COO^- \longrightarrow PTS^- + H_2O + CH_3COOH$$

In the first case the *OH* distance of pyranine phenolic group was chosen as reaction coordinate; the distance was scanned with a step 0.05 Å in the 1.05-1.55 Å range of values, while relaxing all the others degrees of freedom. Modeling the

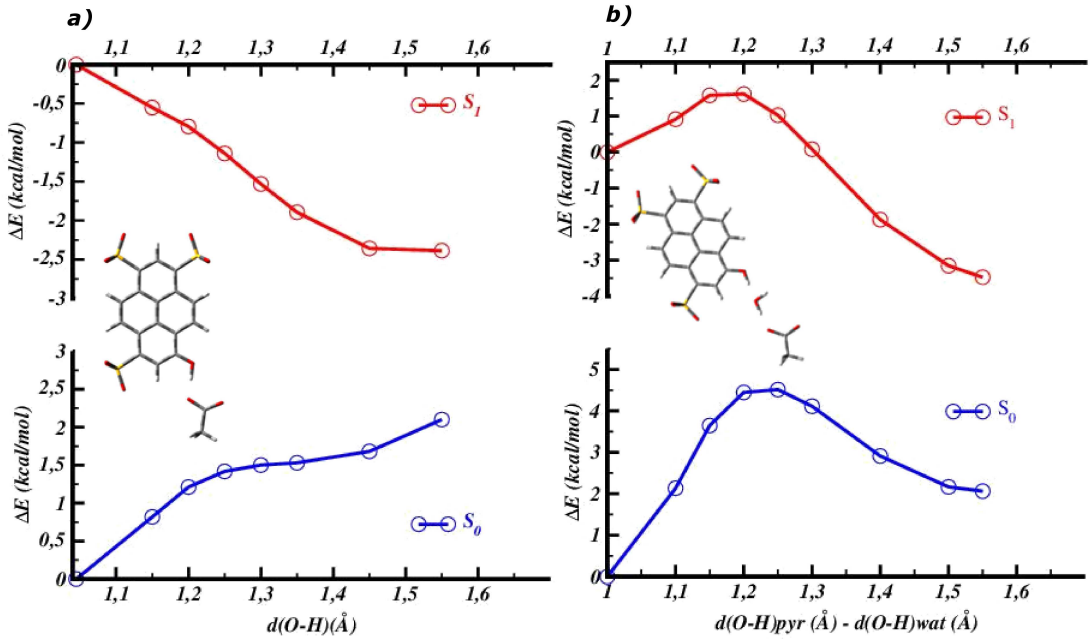

Fig. 3.1: a)Ground (blue) and excited (red) constrained energy profiles calculated for the *pyranine-acetate* ESPT reaction at B3LYP/6-31g(d,p)/C-PCM level of theory. b)Ground (blue) and excited (red) constrained energy profiles calculated for the *pyranine-water-acetate* ESPT reaction at the same level of theory.

ESPT with one intervening water molecule required a double and concerted scan of the OH_{pyr} and OH_w distances. In both cases the energies of the first points, corresponding to a neutral HPTS and a deprotonated acetate, were set to zero. PT and ESPT energy profiles for *pyranine-acetate* and *pyranine-water-acetate* systems in water solution are shown in figure 3.1a,b.

At the ground state , it's possible to observe a monotonic increase of the relative energy of about 2.5 kcal/mol along the OH_{pyr} distance, in case of a direct PT from pyranine to acetate. At the excited state a very different reactivity is observed, with the anionic product stabilized of about 2.5 kcal/mol with respect to the reagent. Namely, at the ground state the PT does not spontaneously occur, while the ESPT

proceeds barrierless. The excited state potential energy profiles associated to the non-direct ESPT mechanism (see Figure 3.1b) show a little barrier of 2 kcal/mol before reaching the anionic ESPT product stabilized of about 3.5 kcal/mol with respect to the neutral reactant. In this case the reaction is not barrierless, according to the experimental evidences [61] that ascribe the ultrafast component of the ESPT (340 fs) to the direct proton shuttle and the slower but more probable component (1 ps) to the mechanism in which there is one or more intervening water molecules. A first glance can be obtained by this minimal molecular representation of the species involved in the reactivity, with an averaged account of the bulk solvent. Nevertheless, in order to rationalize the ultrafast kinetics involved in different mechanisms and to found a structural origin of the pyranine photoreactivity in presence of acetate, a dynamical approach is mandatory. That will be the subject of the next sections.

3.2 Modeling Pyranine-acetate cluster in aqueous solution

3.2.1 Ground state equilibrium sampling

An explicit treatment of the water solvent, according to a molecular mechanics force field is here adopted, just as in the case of the pyranine in pure water. The solvent molecules are not mainly involved in a direct ESPT reaction between pyranine and acetate, but the proton donor-acceptor couple, defining the QM region, has polar and charged groups establishing specific interactions with the surrounding water molecules, modelled according to the MM force field. The atomistic description

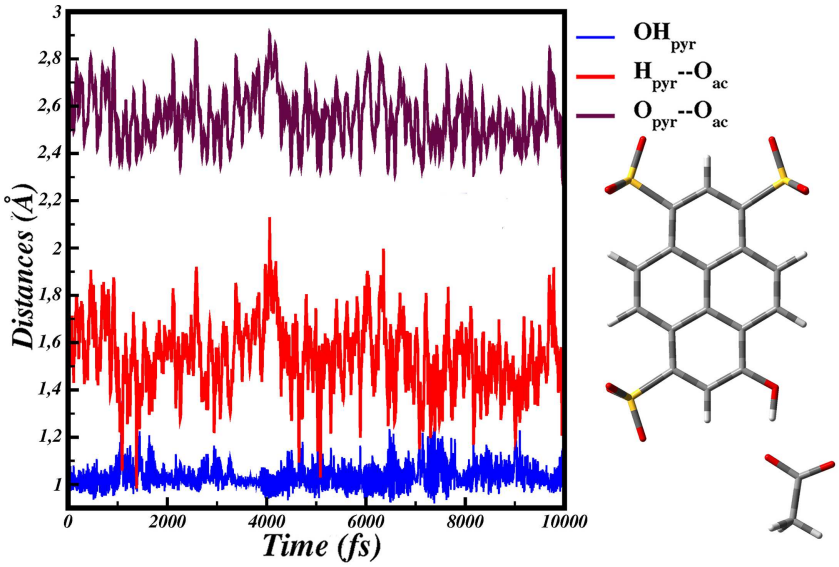

Fig. 3.2: Time evolution of OH_{pyr} (blue), H_{pyr}-O_{ac} (red) and O_{pyr}-O_{ac} (indigo) extracted from the ground state trajectory.

of the solvent is mandatory to get its correct structuration around the pyranine-acetate cluster, in particular around the oxygen atoms of acetate and pyranine. We performed a ground state ab-inito dynamics of the couple *pyranine-acetate*, treated at B3LYP/6-31g(d,p) level of theory, surrounded by 1020 water solevent molecules trated by TIP3P model. The trajectory was 10 ps long, with a time step of 0.2 fs. In figure 3.2 the time evolution of the bonds and the intermolecular distances involved in the PT reaction are shown, namely OH_{pyr}, H_{pyr}-O_{ac} and O_{pyr}-O_{ac}.

Brief proton hopping are observed in some time ranges, around 1000, 5000, 7500 fs. More closely, the proton is here shared between the two heavy atoms of pyranine and acetate. Nevertheless, a proton transfer event from pyranine to acetate does not occur during the simulation time of 10 ps. The dynamical simulation basically

confirms that in the ground state, under equilibrium condition, the proton shuttle does not spontaneously occur, according to the aforementioned constrained energetic profiles and to the pKa values of acetate (4.5) and pyranine (7) in the ground state.

In order to unveil the structuration of the solvent around the pyranine-acetate QM cluster, the radial distribution functions (RDF) between the charged and the polar groups of the QM cluster and the water molecules are calculated and depicted in figure 3.3 . In particular figure 3.3 a,b shows the RDF between the oxygen atoms of acetate and the solvent molecules, the RDF of the phenolic oxygen of pyranine is instead presented in figure 3.3 c.

In figure 3.3 a, we show RDFs of the distances between the acetate oxygen that is hydrogen bonded to pyranine (O_1) and the water oxygen (O_w) and hydrogen (H_w), respectively.

The first solvation shell around O_1 corresponds to the first well-defined peaks, centered at 1.77 Å and 2.77 Å for the O_1-H_w and O_1-O_w distances , respectively. After the first peak the RDF has a no zero value, indicating that an exchange of water molecules occurs between the first and the second solvation shell during the simulation time of 10 ps. The integration of the first peaks suggests that the first solvation shell is on average composed by 1.5 water molecules establishing hydrogen bonds with O_1. The RDF of the acetate oxygen exposed to the solvent (O_2) (see figure 3.3 b) shows similar features. The peaks corresponding to the first solvation shell are centered at 1.77 Å and 2.74 Å and exchange of solvent molecules from the first

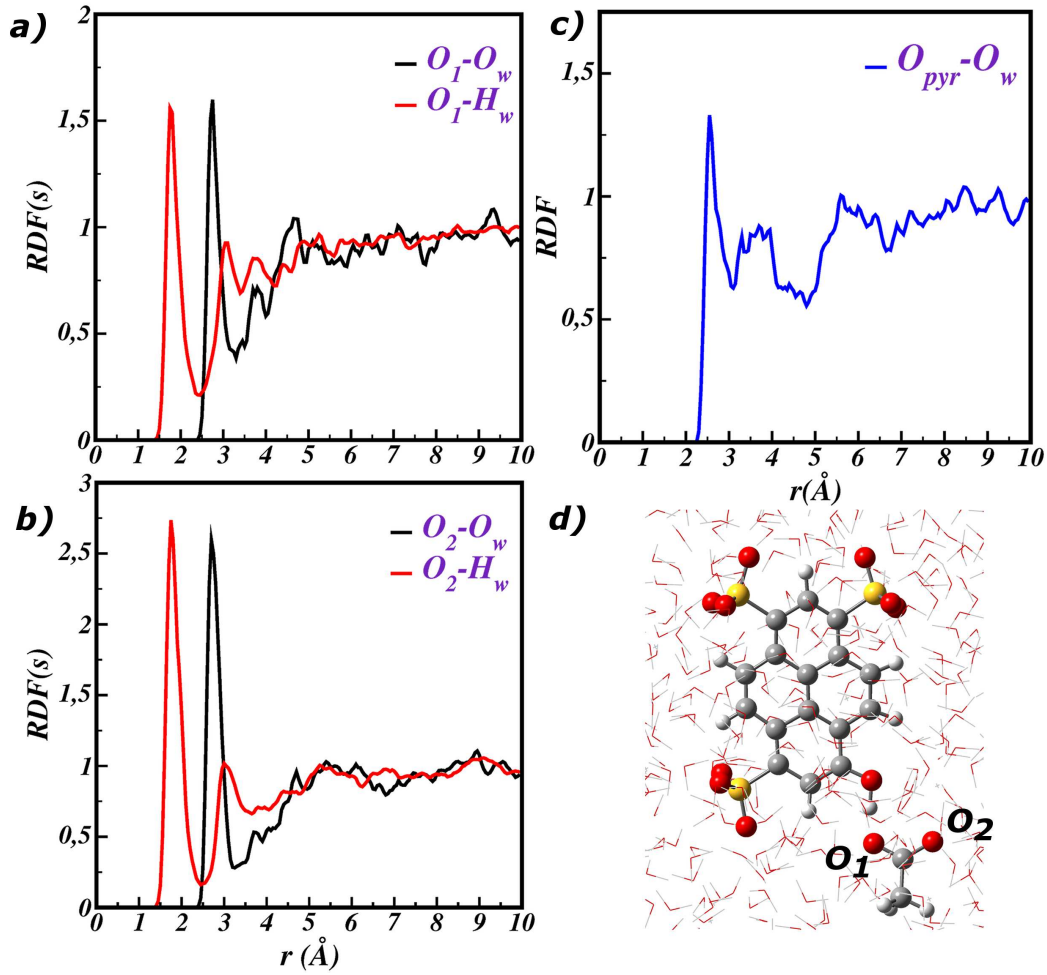

Fig. 3.3: a) RDFs between O_1 and the water molecules, O_1-O_{wat} (black) and O_1-H_w (red) distances are shown. b) RDFs between O_2 and the water molecules. c) RDF between O_{pyr} and the water molecules.

to the other solvation shells are monitored as well. The O_2 does not interact directly with pyranine molecule, so that it's completely surrounded by water molecules. The higher peaks of the first solvation shell report about an average number of 2.5 water molecules around the O_2. Lastly, RDF in figure 3.3c provides information about the solvation of the phenolic oxygen of pyranine O_{pyr} . The peak at 2.58 Å corresponding to the O_{pyr}-O_w distance suggests that on average one water molecule is strongly H-bound to this atom. This water plays a key role in the framework of the ESPT reaction, because it would be involved in a stabilization of the negative charge on the phenolic oxygen, once the proton moves to the acetate. The equilibrium picture points out the arrangement of the solvent molecules around the reactive cluster composed by the negative charged acetate and protonated pyranine. The arrangement is obviously subject to change during and after the ESPT reaction as response to the new charge distribution on the reactive cluster *pyranine-acetate*. Representative points of that equilibrium are chosen as starting points for the propagation of the excited state dynamics. Because the ESPT direct reaction of pyranine-acetate couple is very fast (sub-ps time), the starting point of the excited state trajectory can strongly affect the ESPT kinetic. In particular, the relative orientation of acetate and pyranine will be shown to be fundamental as structural parameter of the starting structure. In this context, the intermolecular dihedral angle CO_{pyr}-CO_{ac} (γ) depicted in figure 3.4 was found suitable to describe the orientation of acetate.

The pyranine is basically planar and the O_1 of acetate is H-bound to its phenolic

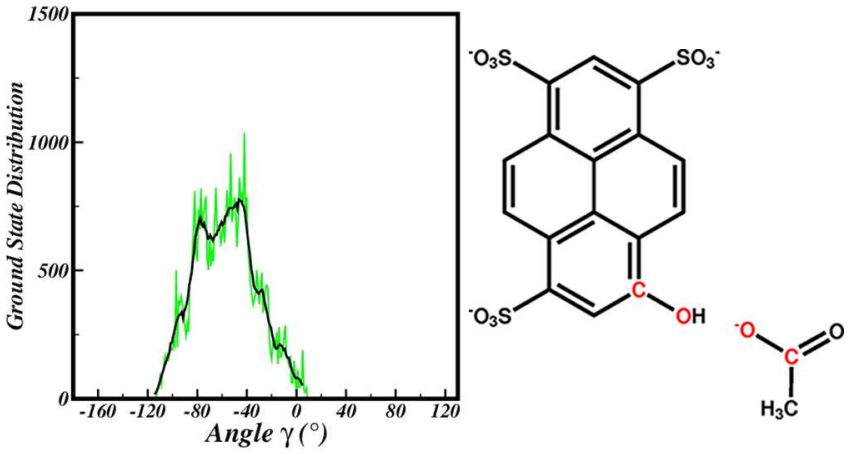

Fig. 3.4: Ground state average distribution of the γ dihedral angle.

group. Regardless of that constrained , the other acetate moiety is free to move around the solvent molecules and to assume different conformations with respect to the pyranine plane. In figure 3.4 is shown the average distribution of the values that the dihedral angle assumes in the ground state simulation. The sample range covers the values 0-113 °. Values around zero correspond to a situation of planarity between the four atoms defining the dihedral angle, but the points in -40-80 range are the most representative of the ground state equilibrium. The γ dihedral angle CO_{pyr}-CO_{ac} is defined by the heavy atoms that are directly involved in ESPT reaction. In the next section, it will be shown that the initial value of the γ dihedral angle will be one of the key factor affecting the ESPT kinetic.

3.2.2 Rationalizing photo-reactivity: direct ESPT reaction

The dynamics simulation of the excited state proton transfer reaction from pyranine (proton donor) to acetate (proton acceptor) will be discussed in this section.

Five excited state trajectories, in which the ESPT happens in different times, have been collected and are shown in figure 3.5. The graphs show the time evolution of intermolecular and intramolecular distances directly involved in ESPT reaction, namely: the OH_{pyr} bond that in excited state is subject to dissociate and H_{pyr}-O_{ac} intermolecular distance.

For the trajectories *1* and *2*, the ESPT reaction takes place within 100 fs and the proton remains bound to acetate for the rest of the dynamics, leading to the deprotonated pyranine. The trajectories *3* and *4* are characterized by a proton hop at the time of about 300 fs. Nevertheless, before the proton is definitely bound to acetate oxygen, it is possible to recognize some time ranges in which the proton is shared between the oxygen heavy atoms of pyranine and acetate. Trajectory *5* has the slowest kinetic, indeed the ESPT is observed around 650 fs. Different starting structures distinguish the five trajectories. In order to rationalize how the choice of the initial point affects the ESPT kinetic observed in the five trajectories, the main structural parameters characterizing each starting structure are analyzed and they are given in table 3.1. We considered as important factors in the initial structure: the solvation and structuration of the solvent around the proton donor-acceptor atoms, the hydrogen bond network of the bonds directly involved in the reaction (OH_{pyr}, H_{pyr}-O_{ac} and O_{pyr}-O_{ac}), the relative orientation of pyranine and acetate, represented by the γ dihedral angle. The ground state sampling already provides a picture of a strong hydrogen bond between the proton donor-acceptor couple, i.e.

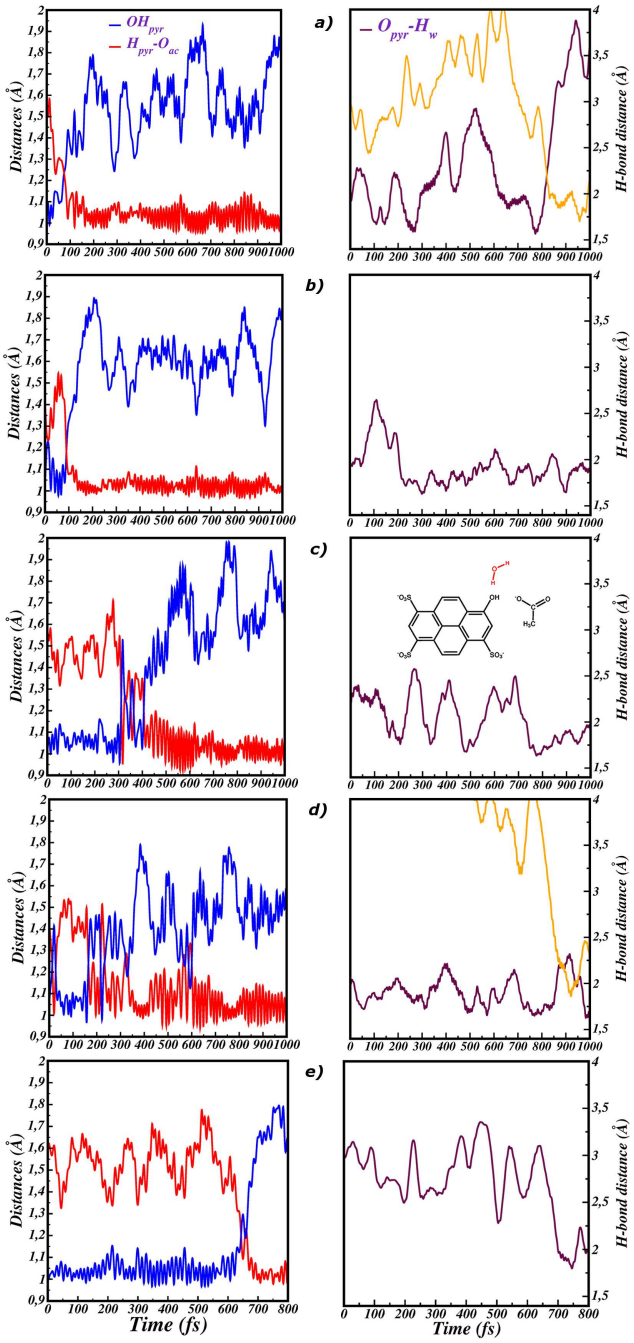

Fig. 3.5: Graphs of the ESPT reaction monitored in five trajectories. Each trajectory starts from a different initial structure. a) Trajectory *1*: left panel shows the time evolution of OH_{pyr} and H_{pyr}-O_{ac}, right panel indicates the time evolution of the intermolecular distance between phenolic oxygen of pyranine and the water molecule (indigo line).The orange line indicates the exchange with an other water molecule monitored during the dynamics. b) Trajectory *2*. c) Trajectory *3*. d) Trajectory *4*. e) Trajectory *5*.

			Starting point			
	ESPT (fs)	γ angle (°)	O_{pyr}-H_w (Å)	OH_{pyr} (Å)	H_{pyr}-O_{ac} (Å)	O_{pyr}-O_{ac} (Å)
Traj1	100	-9	1.92	1.0	1.57	2.57
Traj2	100	-14	1.95	1.03	1.42	2.42
Traj3	300	-48	2.19	1.06	1.41	2.46
Traj4	300	-52	1.99	1.01	1.57	2.57
Traj5	700	-62	/	1.01	1.59	2.57

Table 3.1: Main structural parameters characterizing the starting point of the five excited state trajectories.

pyranine and acetate, with an O_{pyr}-O_{ac} average value of 2.55 Å.

All the starting structures are characterized by an O_{pyr}-O_{ac} intermolecular distance within the range 2.42 -2.57 Å. In particular O_{pyr}-O_{ac} distance of 2.57 Å is the starting point of the trajectories *1*, *4* and *5* having ESPT kinetic of 100, 300 and 650 fs respectively. The contribution of the O_{pyr}-O_{ac} distance to the structure of the initial point cannot be considered crucial to rationalize the observed ESPT kinetics. The intermolecular dihedral angle γ is defined by the atoms CO_{pyr}-CO_{ac} as defined in figure 3.4, and it reports about the arrangement of the heavy atoms directly involved in ESPT reaction. According to the ground state distribution the most probable and representative γ values cover the -40-80 ° range. The trajectories *1* and *2*, with an ESPT kinetic within 100 fs, have γ value vary close to the planarity in their initial structure (γ of 9 and 14 ° respectively). The fastest ESPT kinetic are observed when the initial configurations extracted from the ground state sampling are already optimized to let the proton hop. Nevertheless, they are not representative configurations of the ground state sampling equilibrium, because the γ value of -9 and -14 ° are outside the probable range -40,80 °. Moreover, the ESPT reaction

at 100 fs showed in trajectories *1* and *2*, happens before the reported experimental time of 340 fs [61]. In the starting structure of the trajectories *3* and *4*, the γ dihedral angle is far from planarity, with values of -48 and -52 °. The ESPT reaction observed at about 300 fs is therefore slower. In both case the initial points have γ values (-48 and 53 °) within the representative range of the ground state equilibrium, and the ESPT kinetics are in nice agreement with the experimental time constant. The ESPT at 650 fs is the slowest dynamics among the five collected trajectories and it needs a deeper investigation. The γ dihedral of -62 ° characterizing the initial structure, is quite far from planarity, but it is part of the ground state most probable distribution. The γ dihedral angle of the starting point is not the only factor ruling the ESPT kinetic. The delay of the ESPT kinetic in trajectory *5* can be ascribed to the solvation around the phenolic oxygen of pyranine, i.e. the atom donating the proton. The RDF, between the phenolic oxygen of pyranine (O_{pyr}) and the solvent molecule, computed at the ground state, showed that on average one water molecule is hydrogen bound to O_{pyr} . In table 3.1, the H-bond distance O_{pyr}-H_w of the starting structures are given for the five trajectories. In the right column of figure 3.5 there are the graphs of the behavior over the time of the O_{pyr}-H_w distance for each trajectory.

The four trajectories already discussed have initial points in which the water is strongly H-bound to the phenolic oxygen of pyranine, and that water remains close for the rest of the dynamics. Nevertheless, for the trajectory *1* and *4* an exchange

with another water molecule is monitored. The effect of the water is fundamental to stabilize the negative charge on the phenolic oxygen once the proton has moved to acetate. In case of trajectory *5*, instead, there is no water molecule close to the phenolic oxygen in starting structure. That's why a delay of the ESPT reaction is detected. The water approaches the pyranine oxygen, when the proton moves to acetate, stabilizing the anionic pyranine. The trajectory *5* has a starting structure characterized by a dihedral angle representative of the ground state average, but the proton-donor oxygen lacks the water molecule necessary to make stable the ESPT product.

In conclusion, two important factor ruling the ESPT kinetic were identified: the relative configuration of the proton donor-acceptor couple represented by the dihedral γ and the solvation of the proton donor atom. Combinations of these two factors give rise to a starting configurations that can be more or less representative of the ground state equilibrium, making the ESPT reaction faster or slower.

3.2.3 Time resolved vibrational analysis

The ESPT reaction of pyranine becomes ultrafast when a base like acetate is present in water solution. Acetic acid has, indeed, a pKa value of 4.76, in middle of the pyranine pKa in ground and excited state (7 and 0 respectively). The energetic profiles already provide a picture of a barrierless ESPT direct reaction. The dynamics simulations showed how the proton hop takes place in excited state within 1 ps for different configurations. In this context, the negative charge of acetate, together

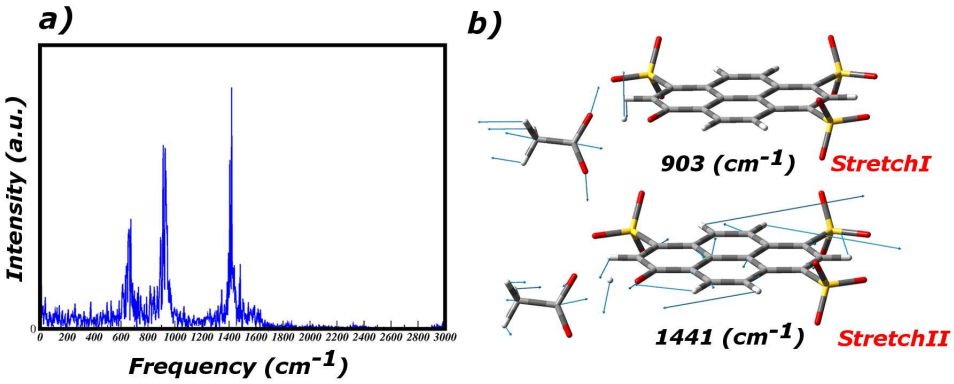

Fig. 3.6: a) Discrete Fourier transform of the CC_{ac} stretching extracted from dynamics. b) CC_{ac} stretching modes computed at the minium energy structure at B3LYP/6-31g(d,p).

with the charge transfer degree associated to the electronic transition of pyranine is sufficient to allow the proton hop in excited state. The peculiar activation of the vibrational modes discussed in case of pyranine in pure water solution is no longer necessary before the ESPT reaction, because the ground state sampling already provides starting configurations sufficiently optimized for the proton transfer. The extraction of the vibrational modes from dynamics is therefore not employed. Nevertheless, it's worth discussing a particular vibrational mode that can be used as fingerprint band to follow the ESPT reaction: the acetate CC stretching vibrational frequency. CC_{ac} stretching was experimentally found at the frequency of 928 cm^{-1}. Figure 3.6a shows the discrete fourier transform of the time dependent CC_{ac} distance extracted from the ground state dynamics.

It's possible to recognize two fundamental bands at 926 cm^{-1} and 1420 cm^{-1}. The transformation to the frequency domain by means of the discrete fourier transform was done on a structural parameter (CC distance), and not on a generalized mode

extracted from trajectory. The discrete fourier transform graph in figure 3.6 shows, therefore, the vibrational modes having as component the CC_{ac} stretching motion. In this case, the band at 926 cm^{-1} is the CC stretching mode (**StretchI**) experimentally recognized (928 cm^{-1}) [61]. The band centered at 1420 cm^{-1} is another kind of CC_{ac} stretching (**StretchII**). In order to investigate the nature of the two type of CC stretching, the composition of **StretchI** and **StretchII**, from frequencies computation at the minimum energy structure, is given in right panel of figure 3.6. Both of them have a strong CC_{ac} stretching component, but the **StretchI** is associated to an out of plane of the pyranine phenolic hydrogen, and **StretchII** involves, instead, some ring deformation mode. The static frequencies values (903 and 1441 cm^{-1}) are different from the corresponding dynamics (926 1420 cm^{-1}) and experimental values (928 cm^{-1}), because they are calculated within the harmonic approximation. The experimental reference spectrum [61] covers the frequency range 0-1350 cm^{-1}, and an experimental reference value to be compared with the 1420 cm^{-1} dynamics frequency is therefore not available. Our investigation, however, showed that the CC_{ac} stretching motion participates basically to two kind of vibrational modes at 926 cm^{-1} and 1420 cm^{-1}. The analysis can benefit from the employment of the wavelet transform, because it provides time resolved frequencies, so that it will be possible to follow the behavior of the modes over the time as the ESPT proceeds. In figure 3.7 and 3.8 the wavelet maps of the CC_{ac} stretching for the five excited state trajectories are given.

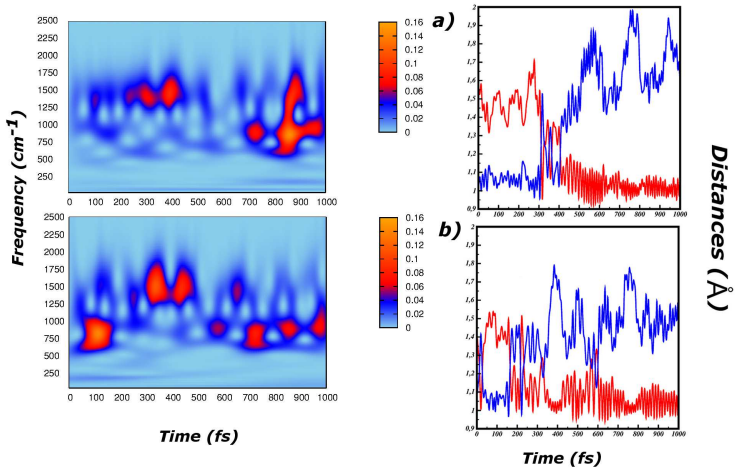

Fig. 3.7: a) Left panel: 2D wavelet map of the CC_{ac} stretching extracted from excited state trajectory *3*. Righ panel: ESPT of trajectory *3* b) Left panel: 2D wavelet map of the CC_{ac} stretching from trajectory *4*. Righ panel: ESPT of trajectory *4*

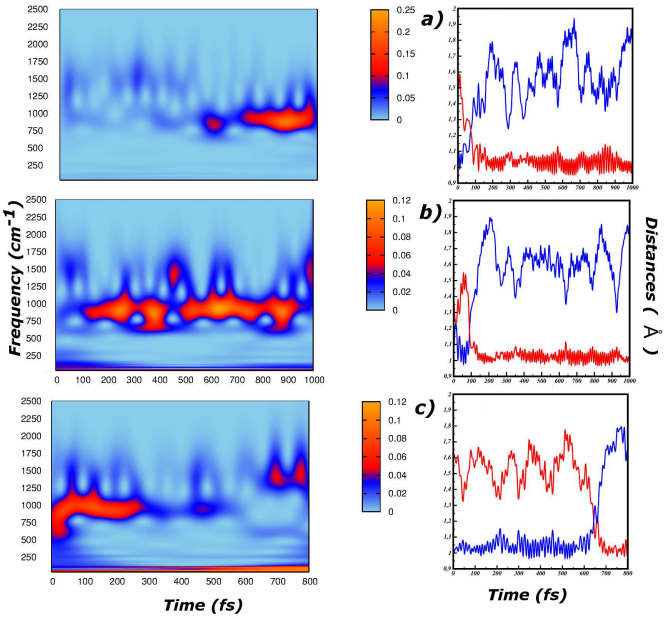

Fig. 3.8: a) Left panel: 2D wavelet map of the CC_{ac} stretching extracted from excited state trajectory *1*. Righ panel: ESPT of trajectory *1* b) Left panel: 2D wavelet map of the CC_{ac} stretching from trajectory *2*. Righ panel: ESPT of trajectory *2* b) Left panel: 2D wavelet map of the CC_{ac} stretching from trajectory *5*. Righ panel: ESPT of trajectory *5*

For the sake of clarity, the corresponding ESPT graphs are again shown. The discussion starts from trajectory *3* and *4*, when the ESPT reaction happens around 300 fs. The proton is not suddenly transferred from pyranine to acetate , but there are time ranges in which the proton is shared between the oxygen heavy atoms of pyranine and acetate. The corresponding 2D wavelet maps of the CC_{ac} stretching show that during the sharing time ranges, the CC_{ac} motion is ruled by **StretchII** mode (1420 cm^{-1}). On the other hand, when the proton is definitely bound to pyranine or acetate the **StretchI** (920 cm^{-1}) controls the CC_{ac} stretching motion. Rationalizing this peculiar behavior requires the analysis of the **StretchI** and **StretchII** composition. The **StretchI** is characterized, indeed, by an out of plane motion of the phenolic hydrogen, but if the proton is shared this motion is not allowed, because the proton is not bound to any oxygen atom. In that time ranges, the **StretchII** (1420 cm^{-1}) appears. The other dynamics are characterized by a sudden proton hop, without long-lasting proton shared periods. The result is that the **StretchII** never appears and the main contribution to the CC_{ac} stretching is basically from **StretchI** mode (926 cm^{-1}), as we can see from figure 3.8.

3.3 Modeling Pyranine-water-acetate cluster in aqueous solution

3.3.1 Ground state equilibrium sampling

In this section the ground state sampling of *pyranine-water-acetate* cluster in aqueous solution will be discussed. The molecular system is separated according to the

hybrid QM/MM scheme already applied to pyranine and *pyranine-acetate* cluster in water. The main difference is that the QM subspace consist of pyranine , acetate and a water molecule between them, as shown in figure 3.9. The QM system lies at the center of a sphere of water molecules explicitly treated. These molecules are free to establish hydrogen bond interaction with the *pyranine-water-acetate* cluster, that have more solvation sites. Indeed, in addition to the acetate oxygen atoms (final proton acceptor) and the phenolic oxygen of pyranine (initial proton donor), the central water can interact with the other solvent molecules as well. In a context of a no-direct ESPR reaction, the solvation around around the central water is essential to correctly describe the double proton hop involving pyranine-water and water-acetate couples. In order to follow the double ESPT reaction, the intermolecular and intermolecular parameters that have to be monitored are: OH_{pyr}, H_{pyr}-O_w, OH_w and H_w-O_{ac}. The time evolution of these main parameters in the ground state dynamics is shown in figure 3.9.

During the simulation time of 7 ps no proton transfer is observed between pyranine-water or water-acetate pair. Moreover, whereas in case of *pyranine-acetate* cluster the grund state dynamics pointed out short proton hops, here, where a water molecule modulates the interaction with acetate, the proton is strongly bound to pyranine. The ground state dynamics of the *pyranine-acetate* and *pyranine-water-acetate* clusters already showed different features, suggesting that the intervening water molecule makes the PT slower. The radial distribution functions (RDF) be-

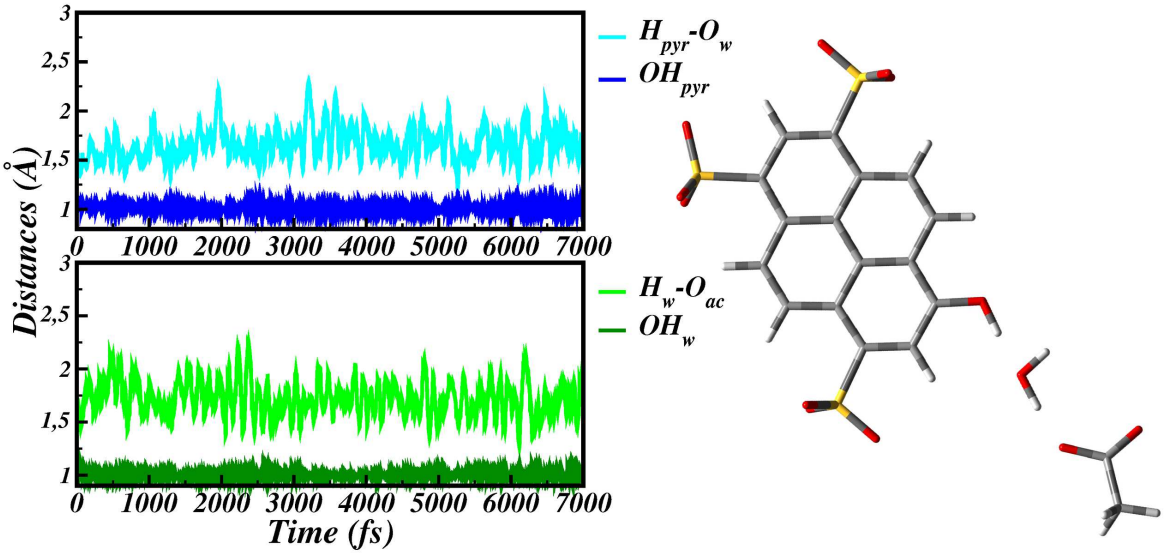

Fig. 3.9: Time evolution of OH_{pyr} (blue), H_{pyr}-O_w (cyan), OH_w (dark green), H_w-O_{ac} (green).

tween the polar and charged groups of the QM cluster and the solvent molecules were calculated and depicted in figure 3.10. The oxygen atoms of acetate are again labelled as O_1 and O_2 , for the oxygen directly bound to the QM water and completely surrounded by MM water respectively.

The RDFs of the oxygen atoms of acetate are quite similar; the peaks corresponding to the first solvation shells ate centered at 2.76 Å and 2.75 Å for O_1-O_w and O_2-O_w respectively. The peaks representing the solvation around the O_2 are clearly higher, indicating that a greater number of water molecules makes up the first solvation shell. Indeed, the integration of the first peaks suggests that O_1 and O_2 are solvated on average by 1.5 and 2.5 water molecules respectively. In both case, after the first peak, there is a pronounced minimum that however does not reach zero value, indicating that solvent molecules exchange are possible from first

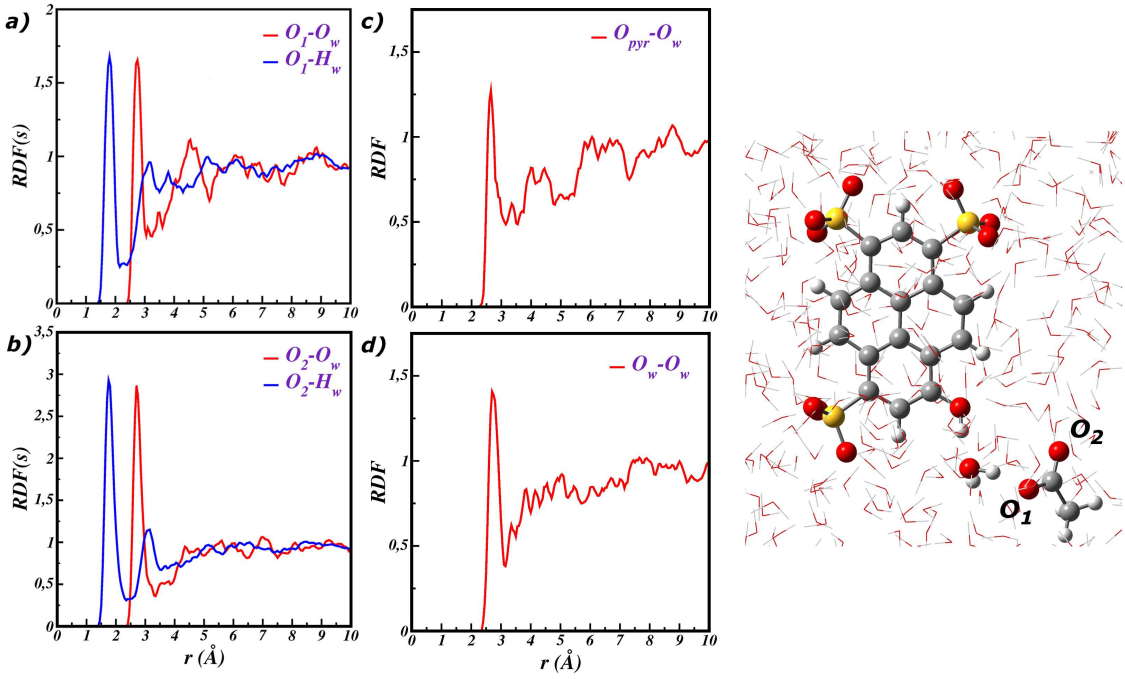

Fig. 3.10: a) RDFs between O_1 and the water molecules, O_1-O_w (black) and O_1-H_w (red) distances are shown. b) RDFs between O_2 and the water molecules. c) RDF between O_{pyr} and the water molecules. d)RDF between O_w belonging to the QM cluster and the water molecules.

to the other solvation shells during the simulation time of 7 ps. The structuration of the solvent around the phenolic oxygen of pyranine and the water belonging to the QM region, is described by RDFs in figure 3.10. The peaks highness and shape indicates that one water molecule is on average H-bound to these atoms. In particular the peak centered at 2.65 Å for the O_{pyr}-O_w distance suggests that an especially strong hydrogen bond is established between the solvent molecule and the phenolic oxygen of pyranine. Indeed, it was already shown the importance of that hydrogen bond in affecting the ESPT kinetic for the direct proton transfer. Here in case of an intervening water making the ESPT slower the accurate description of the hydrogen bonds solute-solvent interaction seems to be even more important for the correct characterization of the ESPT reaction. Indeed, it is unclear how the double ESPT proceeds, if a concerted mechanism occurs or if the central water, accepting the proton from pyranine, becomes an hydronium ion. The solvent molecules could therefore be involved in a stabilization of the reaction intermediate. The problem of the solute-solvent edge interactions and its accurate description will be discussed in next section. As conclusion of the *pyranine-water-acetate* cluster equilibrium sampling, it has to be discussed the relative orientation of the three molecules in solution. Pyranine molecule is basically planar and the oxygen of the central water (H-bound to pyranine) lies in same plane. The acetate molecule instead, with one oxygen hydrogen bound to the central water, is quite free to move in solution. During the ground state sampling, some conformations are explored, in

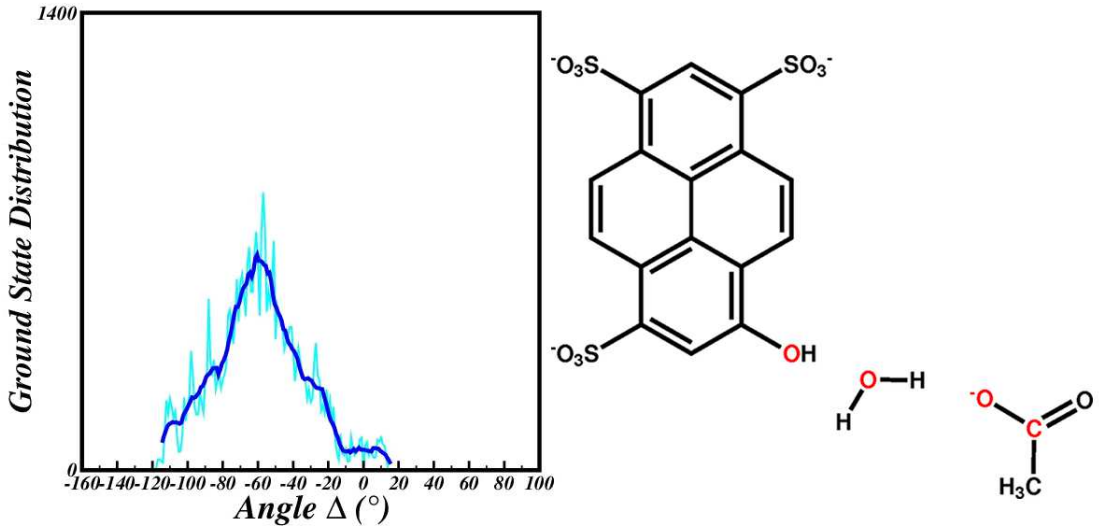

Fig. 3.11: Ground state average distribution of the δ dihedral angle..

which the acetate is more or less planar respect to the pyranine-water plane. The intermolecular dihedral angle O_{pyr}-O_w-OC_{ac} (δ) (in figure 3.11) was identified as key parameter to describe the orientation of acetate. In figure 3.11 the ground state average distribution of the δ dihedral is shown. In ground state, δ assumes values from 0-100° and the most probable and representative points of the ground state equilibrium fall within the 40-80° range. The dihedral angle δ is composed by a network of the heavy atoms directly involved in ESPT reaction.

Values of δ around 0° describe a planar structure promoting the ESPT reaction, but they belong to the tail of the gaussian function describing the average distribution. As already seen in case of the direct ESPT between pyranine and acetate, the structure of the initial point of the excited state trajectories affects the ESPT kinetic. Starting structures with a planar arrangement of the heavy atoms involved in

the reaction (O_{pyr}-O_w-O_{ac}) make the ESPT faster but they can be not representative of the ground state equilibrium.

3.3.2 Rationalizing photo-reactivity: double ESPT reaction

The subject of section is the excited state dynamics simulation of the ESPT reaction involving *pyranine-water-acetate* system. A double proton transfer is meant to happen from pyranine to water first, then from water to acetate. Open issues remain on the reaction mechanism, in particular the reaction can proceeds with a double and concerted proton transfer or in sequential manner. In this latter case, an hydronium ion can be formed as result of the proton hop from pyranine to the water molecule. The ESPT reaction is accompanied by a charge redistribution and the solvent molecules can strongly interact with the reaction intermediate. The solute-solvent interactions has to be accurately taken into account, to provide reliable description of ESPT reaction. The hydrogen bonds network established between the solvent water and the three molecules directly involved in proton transfer reaction (*pyranine-water-acetate*) is described by interactions between an electronic density (QM part) and the charges of the force field (MM part), according to the adopted QM/MM partition. Understanding how accurate is the treatment of the QM/MM solute/solvent interactions is not a simple task. In case of a reaction site embedded in a refined network of hydrogen bonds, it can be required to extend the QM space. Following this logic five excited state trajectories were collected starting from the same initial structure but employing different QM/MM partition. As reference,

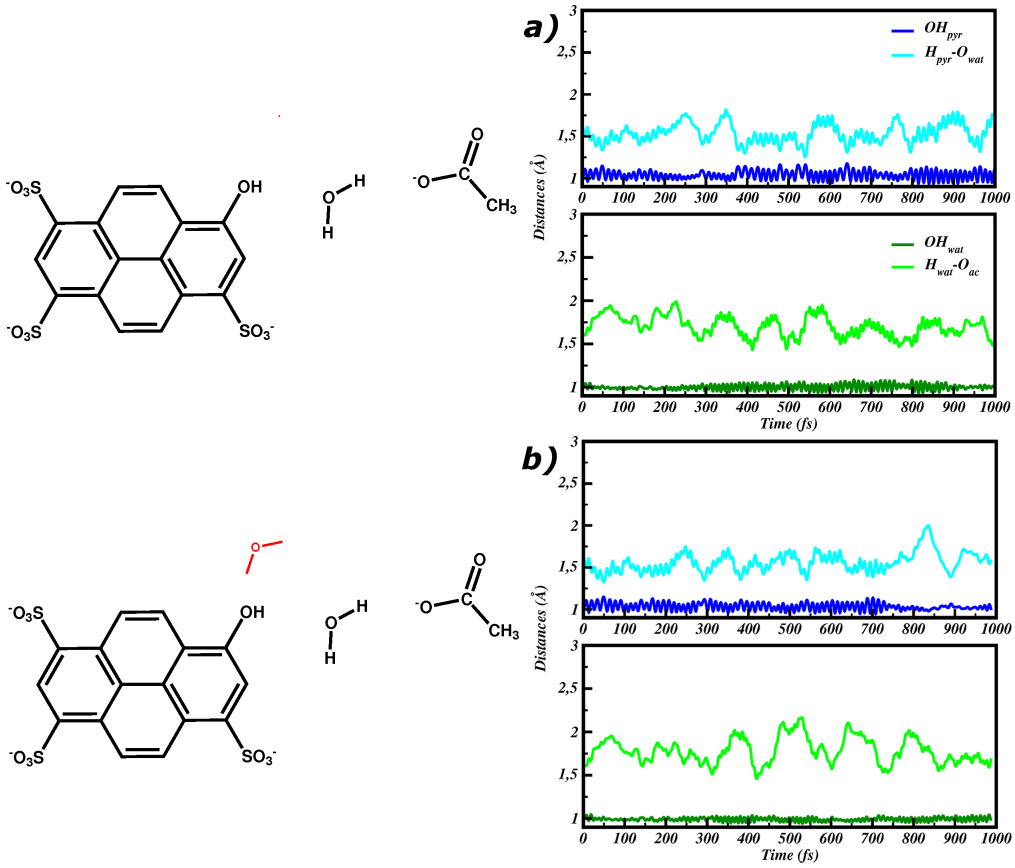

Fig. 3.12: Time evolution of OH_{pyr} (blue), H_{pyr}-O_w (cyan), OH_w (dark green) and H_w-O_{ac} (green) in excited state. The left panels show the QM region. a) **Trajectory 1** in which the minium partition is adopted. b) **Trajectory 2**, the water hydrogen bound to the phenolic oxygen of pyranine is included in QM region

the first trajectory was collected with the minimum partition, namely the ground state QM/MM separation. The other four, in addition to the *pyranine-water-acetate* cluster, include in the QM region one, two, three and five water solvent molecules respectively, as reported in left column of figure 3.12 and 3.13.

The right column of figure 3.12 and figure 3.13 shows the corresponding trajectories, namely the time evolution of the main intermolecular and intramolecular distances directly involved in the reaction: OH_{pyr}, H_{pyr}-O_w, OH_w and H_w-O_{ac}. The

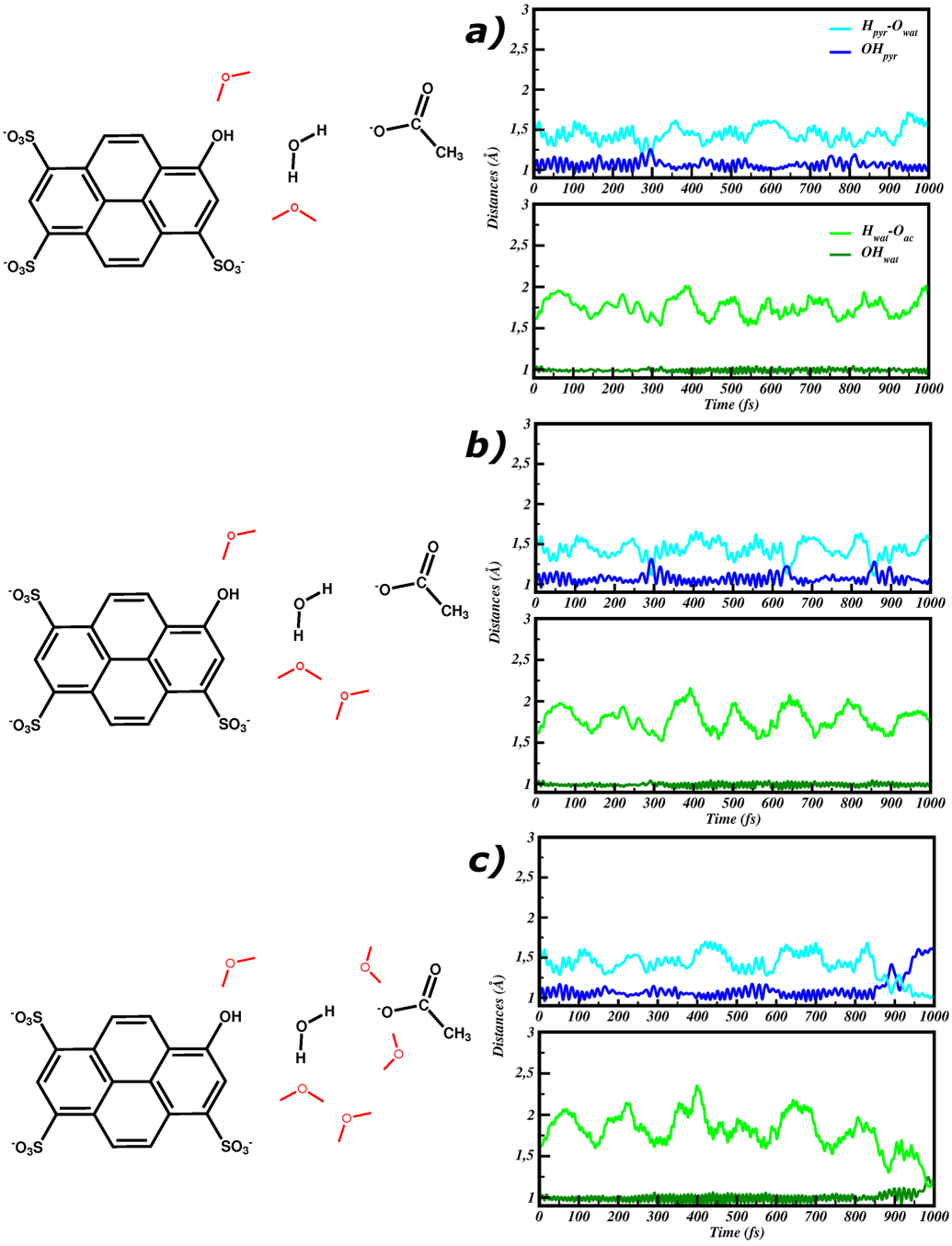

Fig. 3.13: Time evolution of OH_{pyr} (blue), H_{pyr}-O_w (cyan), OH_w (dark green) and H_w-O_{ac} (green) in excited state. The left panels show the QM region. The water molecules included in QM region in addition to the minimum partition cluster, are highlighted in red. a) **Trajectory 3**. b) **Trajectory 4**. c) **Trajectory 5**.

trajectory *2* (see figure 3.12b) includes in QM cluster the water molecule H-bound to phenolic oxygen of pyranine. There are not big differences with the trajectory *1* (figure 3.12c) of the minimum partition. In both cases, indeed, the ESPT is not monitored, and despite the phenolic hydrogen approaches the water molecule, the pyranine remains basically protonated during the simulation of 1 ps. The trajectories *3* and *4* (figure 3.13a,b) are instead characterized by a QM part composed by two and three solvent molecules respectively. The first and partially the second solvation shell of the central water is therefore included on QM subspace. It's possible to observe short proton jump over the time between pyranine-water couple. In particular for trajectory *4* at the time of 300, 620 and 850 fs the proton moves briefly on the water, but a permanent ESPT leading to a stable anionic pyranine does not occur. Moreover, the water-acetate couple does not seem to be affected by the proton hops between pyranine and water. The central water acts both as proton acceptor and donor toward pyranine and acetate respectively, and its solvation at quantistic level seems to promote the first proton transfer event, but no the final proton transfer toward acetate. The final trajectory has the biggest QM partition, including two more water molecules around the oxygen of acetate (see figure 3.13c). The excited state dynamics shows that at the time of 900 fs the proton moves from pyranine to water, leading to the formation of hydronium ion. The proton transfer to acetate is not simultaneous, but the hydronium ion has a lifetime of about 100 fs. Nevertheless, the proton moves to acetate at 1 ps, even if the trajectory is not so

long to observe the stable formation of acetic acid. The five trajectories show a clear trend toward promoting the ESPT reaction with increasing the number of solvent molecules included in QM/MM partition. The first important effect is reached with inclusion of the first and second solvation shell of the central water (trajectories *3* and *4*) when short proton hops are observed between pyranine-water couple. The difference is that the oxygen atoms of the water, now included in QM region, are described accurately by means of the two electron pairs and no longer with the MM charge. That allows for having optimal H-bond orientation and interaction toward the first proton-acceptor atom, i.e. the oxygen of the central water. On this way, the inclusion of the solvent water around the second proton-acceptor atom (oxygen of acetate) makes possible to observe the double ESPT.

The experimental time of ESPT of pyranine in presence of acetate are 340 fs, 1 ps and 6 ps [61]. The fastest kinetic of 340 fs is associated to the direct ESPT from pyranine to acetate, and in the previous sections, a good agreement was found when representative points of the ground state equilibrium were chosen. The time of 1 ps was instead ascribed to the ESPT between pyranine and acetate with the modulation of water molecules. The last dynamics discussed seems to be in fair agreement with the ESPT experimental time constant of 1 ps. It's necessary to know how the initial structure (called **ConfA**) of the trajectory *5* is representative of the ground state equilibrium. Moreover, a comparison with an excited state trajectory, keeping the same partition but starting from a different initial structure (called **ConfB**), was

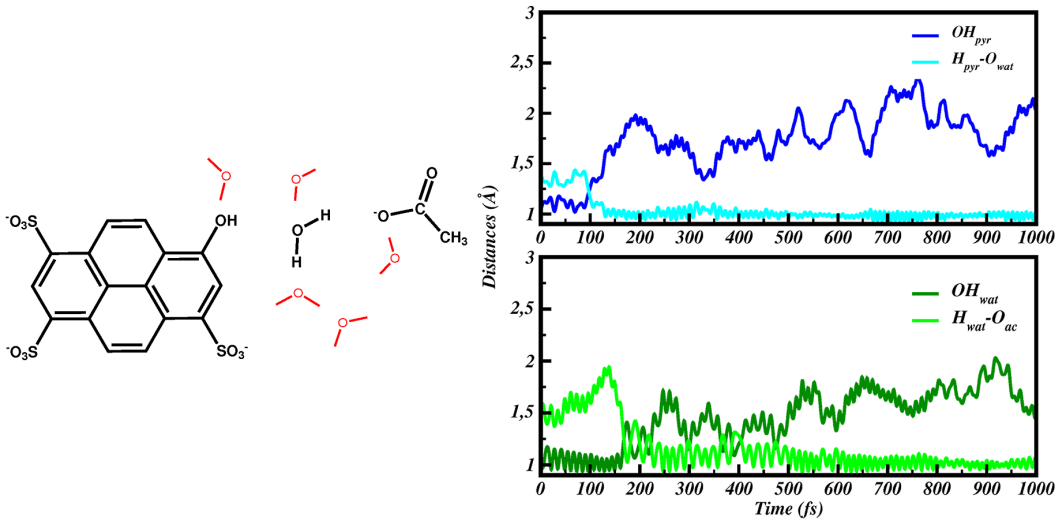

Fig. 3.14: Excited state trajectory starting from **ConfB**. In the left panel are shown the molecules included in QM partition. The right panel shows the time evolution of OH_{pyr} (blue), H_{pyr}-O_w (cyan), OH_w (dark green) and H_w-O_{ac} (green) in excited state.

	Starting point				
	N° of QM water	ESPT (fs)	δ angle (°)	O_{pyr}-O_w (Å)	O_w-O_{ac} (Å)
ConfA	5	1000	-45	2.60	2.54
ConfB	5	300	9	2.45	2.56

Table 3.2: Main structural parameters characterizing the starting point of the two excited state dynamics with the same QM/MM partition.

also done. In table 3.2, the features of both the dynamics (**ConfA** and **ConfB**) are summarized and in figure 3.14, it's reported the excited state trajectory having as starting point **ConfB**.

It was adopted the same partition, including five water molecules in QM region, in addition to the reactive cluster *pyranine-water-acetetate*. Figure 3.14 shows that the first proton hop, from pyranine to water, happens at 100 fs, leading to hydronium ion. It has a lifetime of about 100 fs, after that the proton moves to acetate at the time of 200 fs. Nevertheless, in a time range of about 300 fs the proton is not

completely bound to acetate, but it is instead shared between the heavy atoms O_w-O_{ac}. From 500 fs, the formation of a stable acetic acid is monitored and maintained for the rest of the trajectory. Despite **ConfA** and **ConfB** share the same QM/MM partition, **ConfB** shows an early ESPT reaction. The main reason is the different initial structure featured by **ConfA** and **ConfB**. From table 3.2 , it is possible to see that the intermolecular distances O_{pyr}-O_w and O_w-O_{ac} suggest a strong H-bonds network in both cases. **ConfA** is instead characterized by a dihedral δ value of -45° , that falls within the range of the ground state most probable values. The initial structure of **ConfB** has a δ value of 9° that is very close the planarity condition, but it falls within the tail of the gaussian function describing the ground state δ distribution. This configuration is basically characterized by a planar arrangement of the atoms O_{pyr}-O_w-OC_{ac}, defining the dihedral δ. As already seen for direct ESPT of pyranine-acetate couple, here it was found that initial point characterized by a planar disposition of the heavy atoms of the reactive site promotes and accelerates the excited state proton transfer reaction.

3.3.3 Time resolved vibrational analysis

The excited state proton transfer reaction involving the *pyranine-water-acetate* cluster is an intermediate situation between pyranine in pure water and pyranine-acetate. In the first case, before the ESPT event the sequential activation of low frequencies vibrational modes is necessary to induce a structural optimization between the proton donor-acceptor pair. On the other hand for the *pyranine-acetate* system

the reaction is basically barrierless and the nuclear rearrangement is not required. The presence of acetate, for the *pyranine-water-acetate* cluster, obviously makes the ESPT faster, but the central water suggests that low frequencies skeleton modes have to optimize as well the structural arrangement of the reactive site. The procedure of the extraction of generalized vibrational modes is here employed together with the multiresolution analysis based on the wavelet transform, as already done in chapter 2 for pyranine in water solution. The analysis is performed on trajectory *5* (called **ConfA**), because it is representative of the ground state equilibrium and realistic for comparison with experiment. It must be said that the comparison with the experimental spectroscopic data is quite complex in this case. In case of pyranine and acetate together in water solution, the experimental spectra are the result of all the possible mechanisms: direct ESPT pyranine-acetate or no-direct ESPT with the modulation of one or more water. All the ESPT time constant are available, 340 fs associated to the direct ESPT, 1 ps and 6 ps, with intervening water. A comparison with the experimental rise and decay times of the vibrational modes would be not allowed. Nevertheless, the frequency values are actually comparable, and we can looking for some key vibrational modes that in time window of one picosecond seem to be important in promoting the reaction. In particular we will focus on two vibrational low frequencies skeleton modes, already identified for pyranine in pure water, namely: the four-ring out of plane wagging at the AIMD frequency of 110 cm^{-1} and the collective breathing with AIMD frequency of 198 cm^{-1}. Their composition, as well

as the 2D wavelet maps, are given in figure 3.15. They are collective modes involving the whole nuclear skeleton. In both cases, a nice agreement with the experimental frequency [61] is found (experimental frequencies of 106 and 195 cm^{-1} for wagging and breathing respectively). The wagging mode is basically an out of plane motion, as it is possible to see from the composition of the mode extracted from AIMD (see figure 3.15). In particular, the out of plane motion is localized on CCOH phenolic group, and it can be involved in a structural optimization between pyranine-water couple. The phenolic CCOH out of plane motion defines actually the planarity between the pyranine proton-donor group and the proton-acceptor oxygen of water. The 2D wavelet map of the wagging mode is given in figure 3.15 and it shows just the wagging contribution at the frequency of 110 cm^{-1}. The band appears quickly following the electronic excitation, earlier of the experimental rise time constant of 680 fs [61]. The breathing mode is, instead, an in plane collective motion having an O_{pyr}-O_w intermolecular stretching component. The breathing motion provokes the stretching of the whole molecule and the approaching of the heavy atoms O_{pyr} and O_w. The corresponding 2D wavelet map, in figure 3.15 shows the contribution at about 200 cm^{-1} , associated to the breathing mode. It appears immediately and decays at about 700 fs, in nice agreement with the experimental time decay of 680 fs. The wagging and breathing modes were already identified and discussed in case of photoexcited pyranine in pure water, and it was found that within the time window of 1 ps they were essential to optimize the structural the structural arrangement of

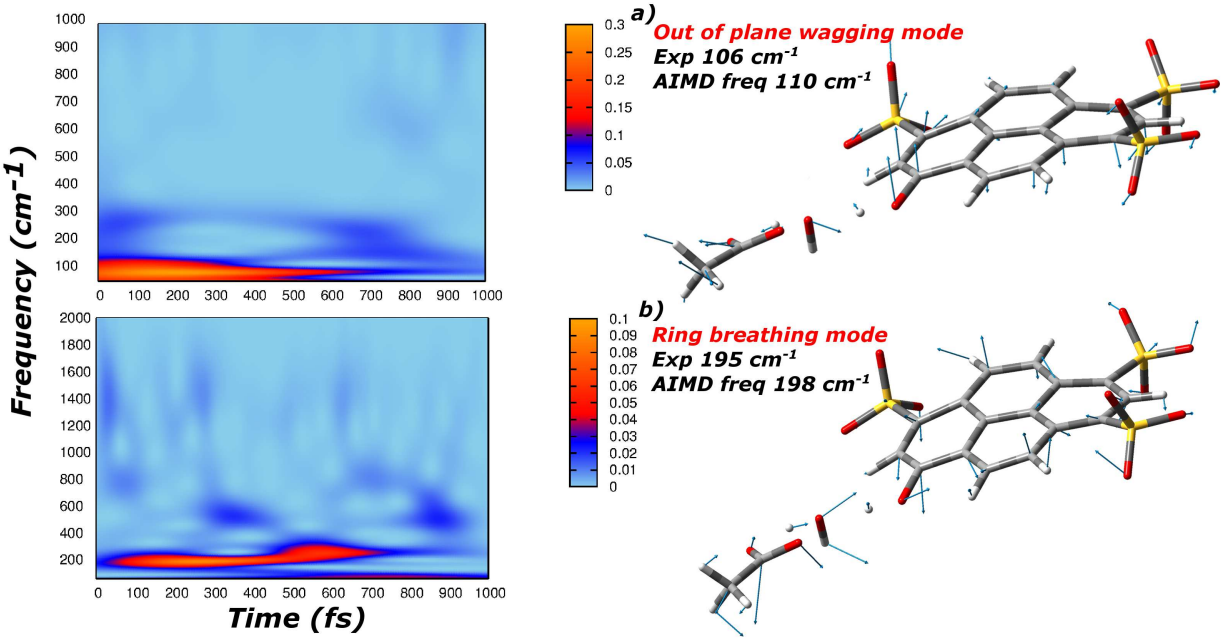

Fig. 3.15: Left panels 2D wavelet maps of the wagging (a) and breathing vibrational modes (b). Their composition is instead shown in right panles.

pyranine-water before the ESPT event. In case of *pyranine-water-acetate* cluster, the two low frequency modes have the same key role, but the presence of acetate makes, obviously, the reaction faster. The analysis was performed on trajectory *5* where the proton transfer from pyranine to water takes place at 900 fs. The wavelet maps highlight that wagging and breathing modes decay just before the proton hop toward water, confirming their key role in promoting the ESPT reaction.

Chapter 4

Unveiling anharmonic coupling by means of excited state ab-initio dynamics: application to diarylethenes photoreactivity

4.1 Introduction to diarylethenes photoreactivity

Diarylethenes molecules are an important class of compounds known to have photochromic properties [128]. Photochromism is defined as the reversible interconversion, triggered by irradiation, of a chromophore between two or more isomers with different absorption spectra [129]. Phytochrome or rhodopsin are renowned examples of biological systems showing photochromic activity [130]. Aiming at mimic the efficiency of the natural biological macromolecules, a great number of synthetic photochromic molecules has been produced so far. These include: azobenzene, spiropyran and diarylethenes classes.

The change of the spectroscopic properties is always ascribed to the alteration of the electronic-nuclear structure upon photoexcitation. Therefore, molecules with

photochromic activity find many applications as light-driven molecular machines, photoswitching devices or molecular sensors [131, 132] . Many efforts were devoted to synthetize photochromic system with the desired properties, namely: thermal stability of the isomers, resistant properties to side-reactions, sensitivity, rapid response. In this context, diarylethenes family, due to the excellent performances, has attracted growing attention, more than others classes of photochromic chromophores [133]. In principle, photochromic reactions should be fully reversible and for some diarylethenes derivatives the coloration/decoloration cycles can be repeated more than 105 times. Figure 4.1 shows a popular diarylethene, 1,2-bis(2,4-dimethyl-5-phenyl-3-thienyl) perfluoro-cyclopentene (F-CHD), one of the most used photochromic molecule in practical applications. Upon photoexcitation, F-CHD undergoes an opening ring reaction, involving the central cyclohexadiene ring, so that a photoisomerization converts the closed and open ring isomer. It's reported that the cycloreversion quantum yield is reduced from around 50% to below 5% for more π conjugated diarylethenes derivatives [134]. The open ring isomer π conjugation is localized to each thiophene ring, while in the closed ring isomer π conjugation is delocalized throughout the molecule and the absorption spectrum shifts to longer wavelength [133].

The closed isomer has an absorption spectrum at visible wavelength ($\approx$ 600 nm), while the absorption of the open ring specie is instead localized in UV range ($\approx$ 300 nm). Therefore, the photoexcitation with VIS wavelength radiation induces

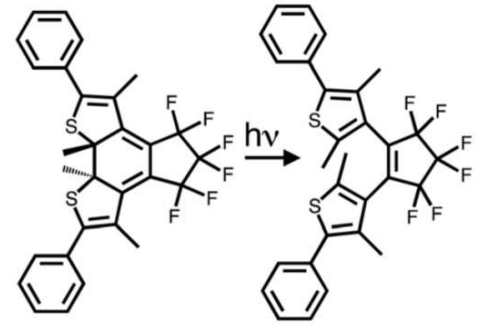

Fig. 4.1: Open and closed structure of 1,2-bis(2,4-dimethyl-5-phenyl-3-thienyl)perfluorocyclopentene (F-CHD).

the opening ring reaction, while the opposite closing ring reaction takes place when the open ring product is excited with UV light [133]. The photochromic activity of diarylethenes is recognized to be controlled by non-adiabatic decay by means of a conical intersection (CI) seam [135,136]. More closely, the ground (S_0) and first (S_1) excited electronic state become degenerate somewhere along the reaction coordinate and the photoexcited molecular system decays to the ground state in a radiationless manner. F-CHD was the subject of several experimental studies [131, 132] devoted to the applications, exploiting its photochromic properties, but also of spectroscopic experiments [134,137,138] aiming at the elucidate the electronic nuclear dynamics at the origin of the F-CHD photoreactivity. Unveiling the driving forces controlling the F-CHD photoreactivity could be helpful to plan a rational design of photochromic system with better performances. In particular, FSRS experiment [134] revealed characteristic oscillations of some time resolved frequencies. Oscillation in vibrational bands are ascribed to anharmonic coupling between high and low frequency modes in excited state. Quantitative measure of the anharmonic coupling remains

a challenging but fascinating task, because gives information about the shape of the PES(s) and the energy flow between vibrational normal modes.

The experimental hypothesis is that vibrational modes (mainly stretching and bending motions) localized to the central 4-ring system are anharmonically coupled to low frequency methyl wagging mode. These modes are defined as reactive because of that coupling would lead to the open ring product. Vibrational modes localized on the phenyl moiety are instead labeled ad unreactive, leading the system back to the ground state. Theoretical studies of F-CHD are quite unusual, due to the size of the system. Moreover the non-adiabatic photoreactivity does not permit to use single reference electronic structure methods, such as DFT and TD-DFT to characterize the whole PES(s). On the other hand, Multi-configurational SCF (MCSCF) methods are suitable for the characterization of the PES region when the crossing between the two electronic surfaces takes place, but it is not feasible for a molecular system of such dimension. MCSCF was employed for the study of the cyclohexadiene unity and some F-CHD model system involving three or four rings [139,140]. In this context is important to know the regions of the PES(s) in which the ground and excited state surfaces are well separated, namely the BO approximation still holds and DFT and TD-DFT based investigations are valid. Within adiabatic approximation, we may always run single surface excited state dynamics and get information about the evolution of the vibrational properties following the procedure developed and applied in the previous chapters. The focus of the work is twofold: in

the first part, the static and dynamics characterization of the F-CHD photoreactivity will be discussed. TD-DFT will be used, where it's allowed, namely to describe the vertical excitation, the relaxation on excited state PES, and the excited state minimum sampling. In the second part, we will deal with a F-CHD model, keeping just the four central rings, i.e. without the phenyl groups. Complete active space SCF (CASSCF) [141, 142] will be employed to characterize the conical intersection structure, and to get more insights about the electronic and nuclear processes leading the system toward the non-adiabatic region and the subsequent evolution to the open ring product throughout the crossing of the electronic surfaces.

4.2 TD-DFT picture of the potential energy surfaces

In the following the focus will be on the direct opening ring reaction, namely the photo-isomerization that starting from the closed ring reagent leads to the open ring product. The vertical excitation energy (VEE) is obtained from the ground state minimum geometry of the F-CHD close ring form. The computed value of the VEE is 2,12 eV in gas phase, that is nice agreement with the experimental absorption spectrum at 2,21 eV in cyclohexane. In principle, this discrepancy could be reduced including the effect of the solvent. Nevertheless, the difference of 0.09 eV, corresponding to the little gap of 2 kcal/mol, is considered negligible and the effect of the cyclohexane unimportant. The kind of transition leading to the S_1 excited state has π-$\pi*$ nature involving the frontier orbitals shown in Figure 4.2. Great part

of charge redistribution concerns the π conjugation localized on the central rings, namely thiophene rings, central cyclohexadiene and the fluorinated cyclopentane, this latter acting as electron acceptor. On the other hands the peripheral phenyl rings are not so involved in charge rearrangement associated to the excitation. A side perspective of the orbitals (see Figure 4.2) makes possible to see the new electronic arrangement on the central CC bond, i.e. the bond that is subject to break in excited state. The electronic charge is strongly reduced along the CC bond going from the ground to the first excited state. According to this depletion, it is predictable that in excited state the CC bond, responding to the new electronic structure, become more stretched and more inclined to break.

In order to get a first picture of the potential energy surfaces involving in the open ring reaction, a constrained potential energy profiles along a suitable reaction coordinate were calculated at the ground (S_0) and first excited state (S_1), by means of DFT and TD-DFT. In principle, DFT and its time dependent version, as single reference electronic structure theory, are not able to characterize the crossing points between two electronic surfaces. Nevertheless, this procedure aims at understanding where the two surfaces start to be degenerate along the reaction coordinate, so that it will be possible to identify some regions of the PESs that can be treated in adiabatic way. The ground and excited state energetic profiles are shown in Figure 4.3 and are built starting from the close ring F-CHD at the ground state minimum, choosing the central CC bond as reaction coordinate. The CC distance was scanned from 1.54

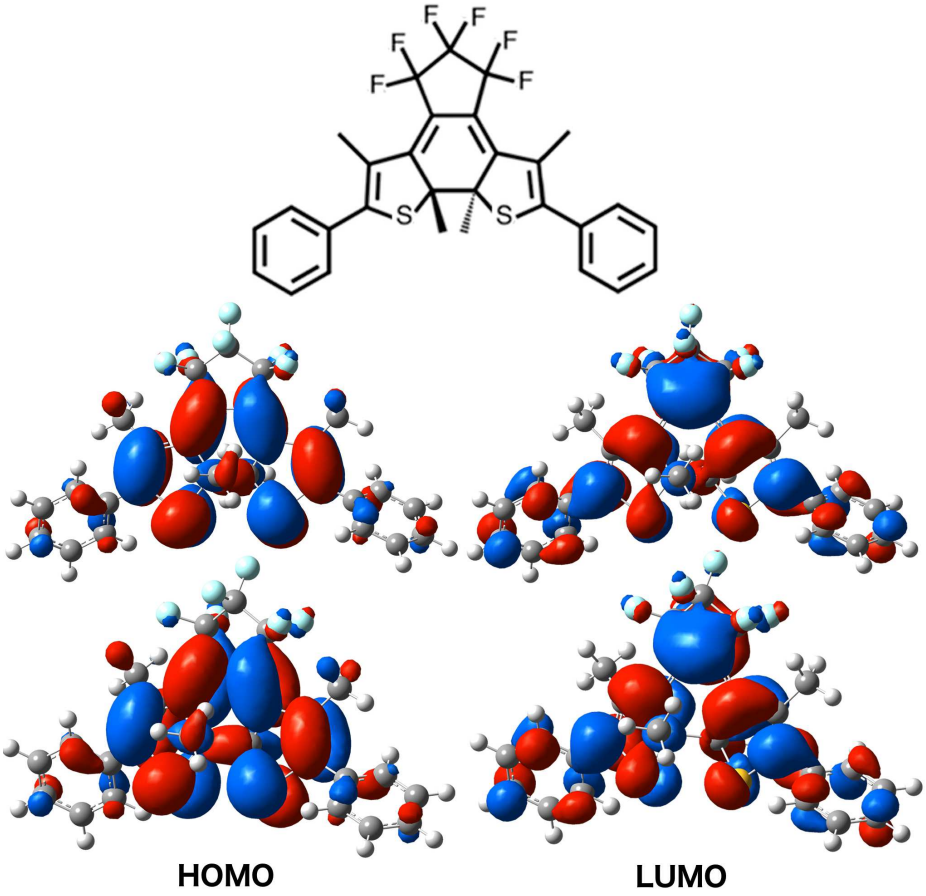

Fig. 4.2: HOMO and LUMO contour plots computed for F-CHD in the ground-state minimum energy structure computed at B3LYP/6-31g(d,p).

Å to 3.98 Å, which correspond to the values that the *CC* bond assumes respectively in the close and open ring isomer in their ground state minimum (green circles in Figure 4.3). The intermediate points were obtained keeping fixed the *CC* distance, while relaxing on the ground state all the others degrees of freedom. The excited state profile was instead computed vertically on that points. The profiles represent relative energies respect to the energy of the closed ring F-CHD, that was instead set to zero. At the ground state the transformation between the closed and open ring form requires an energetic barrier of about 50 kcal/mol. Instead, when the molecule is photoexcited the scenario dramatically changes. A little barrier of 6 kcal/mol separates the excited state minimum from the non-adiabatic region where the energy levels of the ground and the first excited state are degenerate (black lines in Figure 4.3). The excited system drops down to the ground state throughout this conical intersection point. The radiationless decay to the ground state leads to the open ring isomer, that is about 13 kcal/mol more stable than the closed one.

As already mentioned above, the DFT doesn't allow to characterize the intersection points, but we can get information about the region of PESs in which the ground and excited state surfaces are well separated and the adiabatic approximation still holds. More closely, within the range of values of the *CC* bond from 1.54 to 1.75 Å the two electronic surfaces are clearly non degenerate. According to the given level of theory, the two surfaces become too close in energy at the distance of 1.80 Å of *CC* bond. As a matter of fact, in Figure 4.3, the ground-to-excited state

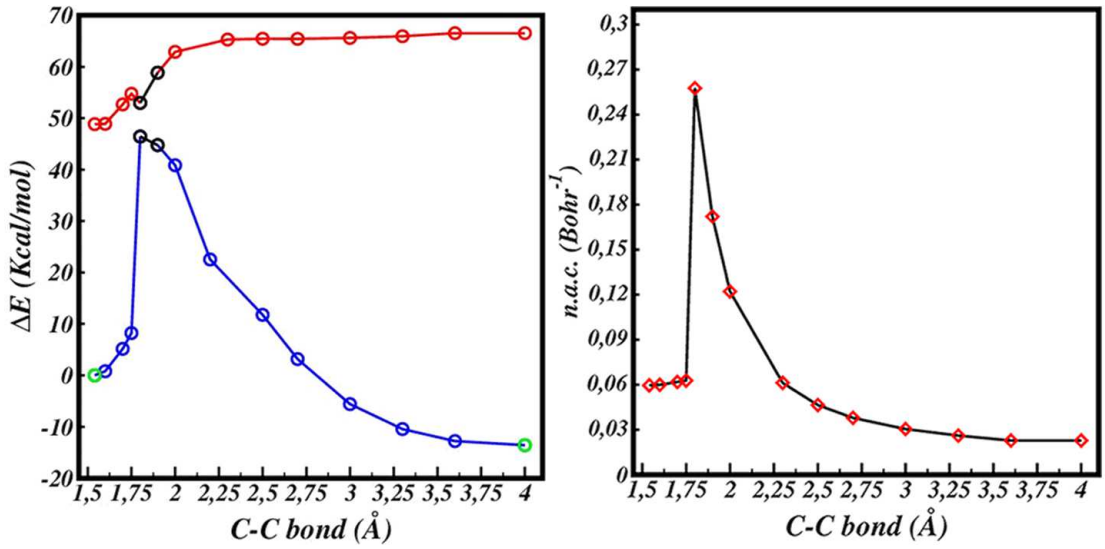

Fig. 4.3: Left panel: Ground (blue) and Excited (red) constrained energy profiles calculated for the opening ring reaction at B3LYP/6-31g(d,p) level of theory. The black lines indicate the non-adiabatic regions, while the green circles are the energy of the fully optimezed open and closed ring structures. Right panel: Non-adiabatic couplings computed along the profiles

non-adiabatic couplings (*nac*) [143] along the constrained profiles are shown. The first order non-adiabatic coupling matrix elements, can be written as

$$\tau_{mn}^{\xi} = \frac{\langle \Psi_m | \frac{\partial}{\partial \xi} \hat{V}_{ne} | \Psi_n \rangle}{E_n - E_m} \tag{4.1}$$

where E_n and E_m are the energy eigenvalues of the states Ψ_n and Ψ_m, $\hat{V}_{ne}$ denotes the operator of the electron-nuclear interaction and ξ indicates a cartesian nuclear coordinate.

In this implementation [143], first order *nac* are computed in the framework of the linear response TD-DFT, namely the excited state wavefunction is not computed, since all information about excited state properties are contained in the time evolution of the ground reference state. *NAC* computation is here employed to report

about the coupling between the ground and first excited state along the constrained PES, with the *CC* bond as reaction coordinate. The maximum value of *nac* corresponds to a *CC* distance of 1.80 Å, that probably is point of conical intersection. In the distances range 1.54-175 Å, *nac(s)* undergo little variations and are always low. That's the region of the vertical excitation energy from the ground state minimum of the closed ring isomer and the relaxation on the excited state surface reaching the minimum geometry. Excited state structure corresponding to the distance of 1,75 Å could be a transition state separating the S_1 minimum from the non-adiabatic region of the conical intersection. The adiabatic sampling of that region will be the subject of the section 4.4.

4.3 MC-SCF study of M-CHD

4.3.1 Justifying the model

The theoretical investigation of the F-CHD is not an easy task. The non-adiabatic photoreactivity does not allow to employ TD-DFT for the characterization of the conical intersection between the ground and excited state surfaces. On the other hand, due to the big size, a MC-SCF method is not feasible to characterize the full system. Some model were proposed, keeping three or four rings without the phenyl and methyl groups [139, 140]. The model (M-CHD) subject of the present investigation, is given in Figure 4.4. The model does not include the phenyl groups, but it keeps the methyl groups and the fluorinated cyclopentane. In order to justify how reasonable the model is, the nature of the electronic transition leading to the

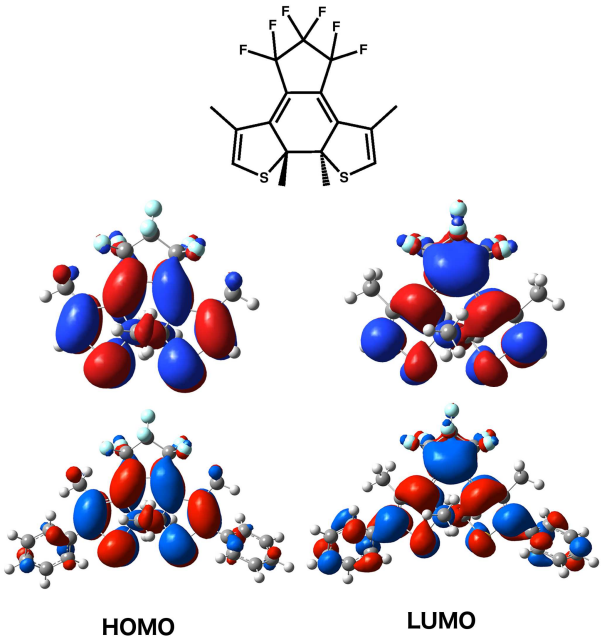

Fig. 4.4: Comparison between the HOMO-LUMO of the F-CHD and the model proposed (M-CHD), computed at B3LYP/6-31g(d,p) level of theory.

excited state should be studied and compared to the original one. In particular, HOMO-LUMO are involved in the electronic transition leading to the first excited state as well. The comparison of the frontiers orbitals, calculated at the same level of theory, of F-CHD and M-CHD (see Figure 4.4) shows that the electronic re-distribution on the central four ring system is definitely the same in M-CHD and F-CHD. It's possible to hypothesized that the nuclear response to the new electronic arrangement would be approximately the same.

4.3.2 CAS-SCF investigation of M-CHD

The complete active space SCF (CAS-SCF) [65,66,141,142,144] belongs to the family of the MC-SCF methods, because multiple electronic configurations are taken

into account and combined to forming the electronic wavefunctions. The total orbitals space of the molecular system is decomposed into three subspace: core orbitals, active orbitals and virtual orbitals. A CAS-SCF calculation is conceptually a combination of an SCF computation with a full configuration interaction (full CI) calculation involving just a subset of orbital. The active space is composed by the orbitals involved in CI calculations. The active space includes both occupied and virtual orbitals, and all possible occupations of the orbitals are taken into account. CAS-SCF is useful to characterize the PES(s) points in which the ground and excited state are degenerate and it's here applied to the study of M-CHD. Stationary points on the ground and first excited state were determined at CAS(10,10)/6-31g(d) level of theory. The active space is composed by ten orbitals occupied by ten electrons. In particular four π-$\pi*$ pairs and one σ-$\sigma*$ pair were chosen. The bonding and antibonding σ-$\sigma*$ orbitals are localized on the central CC reactive bond and are included to correctly describe the breaking reaction. The orbitals for the active space are selected based on occupation criteria, according to the natural bond orbitals population analysis [145]. In figure 4.5 it is shown the energetic diagram of the stationary points along the reaction coordinate, i.e. the reactive CC bond. The energy of the optimized closed ring isomer was set to zero.

The point represented by a red star corresponds to the optimized conical intersection point, where the intersection between the ground and excited state surface takes place [146]. At the conical intersection point the eigenvalue of the electronic

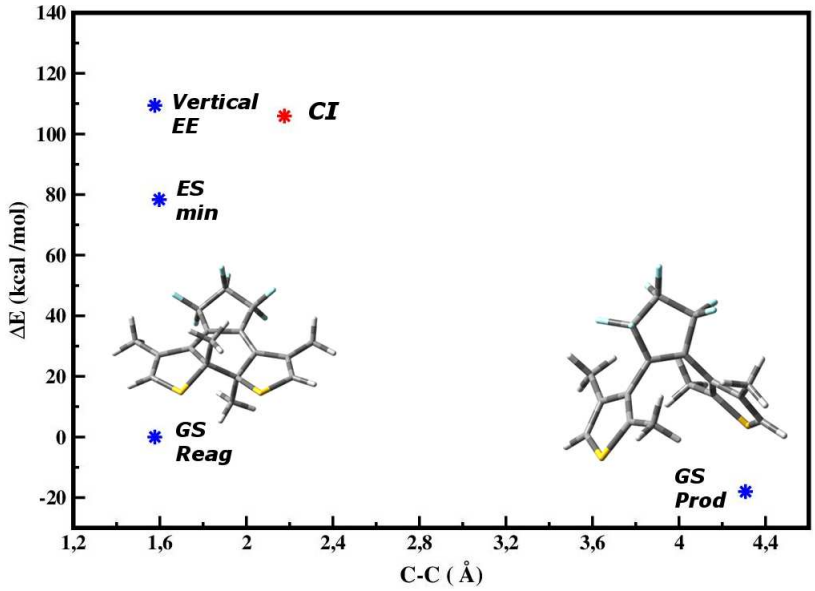

Fig. 4.5: Energies of the stationary points optimized at cas(10,10)/6-31g(d) level of theory.

state are degenerate and the non-adiabatic coupling terms, that are usually small in the hamiltonian expression, become non-negligible. If the energies are plotted against two special internal coordinates, defining the so-called branching space ,the two potential energy surfaces assume the double cone shape. In particular, the two coordinates correspond to the gradient difference vector and derivative coupling vector. Motion on the branching plane lifts the degeneracy between the electronic states. The optimization of the conical intersection [147] is carried out with the constrain that the energy difference between the ground and excited state is minimized.

Once photoexcited, the closed ring M-CHD undergoes a relaxation reaching a minimum energy structure on excited state surface. The relaxation pathway does not involve the *CC* reactive bond, but it regards mainly the *CC* bonds chain shown in red in Figure 4.6. The main structural parameters of the stationary points are reported

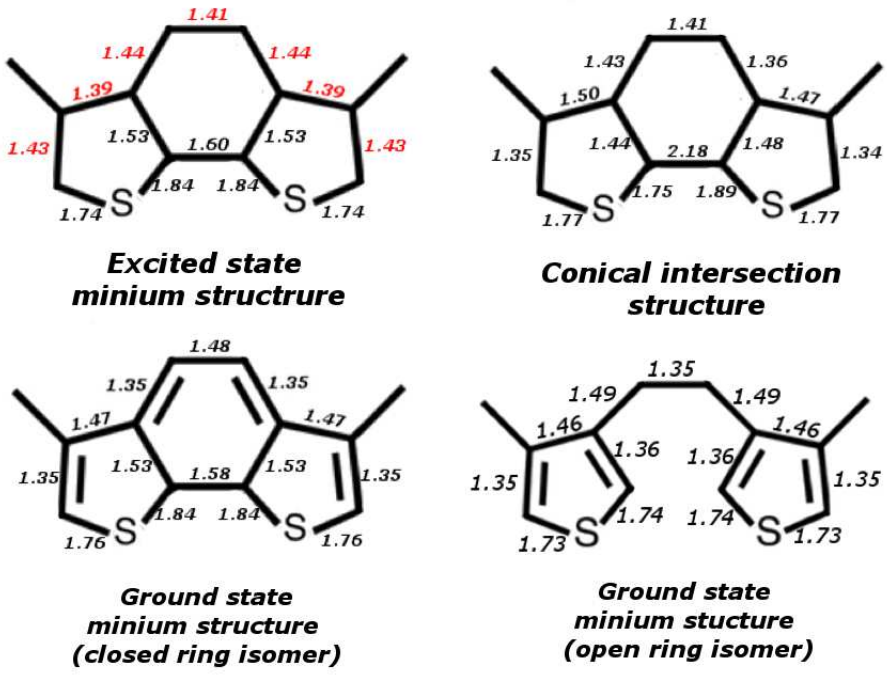

Fig. 4.6: Main distances (Å) of the structures involved in opening ring reaction.

in Figure 4.6. The variations on fluorinated cyclopentane in all the structures are negligible.

In spite the nuclear relaxation, the M-CHD structure at the minimum of the excited state surface keeps the symmetry. On the other hand, the symmetry of the CI structure is completely broken. An energetic barrier separates the conical intersection point from the excited state minimum, that is about 20 kcal/mol more stable. The CI represents the crossing point between the ground and first excited state surfaces. The system evolves in the open ring product throughout this point. The structure is characterized by the CC reactive distance of 2.18 Å that is going to break. The thiophene rings resemble their ground state structure, but it has to be

noted that one *SC* bond with a distance of 1.89 Å tends to break. This is probably the origin of a side reaction involving the dissociation of the C-S bond [140]. The system drops down again to the ground state forming the open ring product, that is about 18 Kcal/mol more stable than the closed isomer.

4.4 Excited state AIMD: extending the time resolved vibrational analyisis

Upon excitation F-CHD undergoes a strong vibrational activity depicting the nuclear evolution on the excited state PES. Time resolved vibrational bands were the subject of a deep experimental investigation aiming at the understanding how the evolution of the normal modes could be responsible of the barrier crossing toward the conical intersection point [134]. Two groups of vibrational modes were identified as strongly coupled to each other. In particular, the first group is composed by *CC* stretching (1181 cm^{-1} and 1333 cm^{-1}) and *CCC* bending (467 cm^{-1}) localized on cyclohexadiene and thiophene rings and they are coupled to the low frequency wagging motions of the methyl groups on cyclohexadiene ring (191 cm^{-1}). On the other hand, *CC* stretching and *CCC* bending modes of the peripherical phenil rings belong to the second group and are supposed to be coupled with the low frequency asymmetrical whole molecule bending. The modes belonging to the first group were labeled as 'reactive', because of that coupling would be responsible of the barrier crossing and the subsequent opening ring reaction throughout the conical intersection. The modes of the second type were instead recognized as 'unreactive' The

coupling was proven by means of the analysis of the intensity and frequency oscillation of the time resolved vibrational bands. More closely, high frequency motions (stretching and bending) have oscillating behavior modulated by the low frequency modes (i.e. methyl wagging) [134]. The oscillation period corresponds to the frequency of the modulating modes. In the following discussion, the focus will be on the modes belonging to the first 'reactive' group and the coupling between them. The adopted strategy, as usual, includes excited state ab-initio molecular dynamics, together with the time resolved vibrational analysis based on the wavelet transform. This procedure allowed us to follow in real time the sequential activation of some key normal modes in case of photoactivated pyranine in water solution. The next step will be the quantitative analysis of the time resolved signals coming from the wavelet maps, to get information about the anharmonic coupling. The method developed and applied in the previous chapters is here extended and tested to the challenging case of photoexcited F-CHD. A first insight about the response of the nuclei to the photoexcitation and to the new electronic arrangement can be obtained analyzing the average values in both ground and excited state of some key bonds of the central moiety. Following the labels appointed in Figure 4.7, the average values of all the bonds of the central four ring system, in both the ground and excited state, are shown in Table 4.1. It's worth comparing the ground and excited state behavior considering the contours of the frontiers orbitals (HOMO-LUMO in Figure 4.2) involved in the transition leading to the electronic state of interest. Going

from the ground to the excited state, *CC5-CC6* bonds of the cyclohexadiene ring and *CC9-CC10* of the thiophene rings become more stretched from a typical double bond value in the ground state (1.37 Å) to average values of 1.42 -1.40 Å in excited state (*CC5-CC6* and *CC9-CC10* respectively). It happens according to a depletion of electronic density on that bonds, as it's possible to see from the frontier orbitals (see Figure 4.2). On the other hand, an increase of density on bonds *CC2*, *CC3*, *CC4* (cyclohexadiene) and *CC7*, *CC8* (thiophenes) is observed, making the bonds shorter in excited state. It's interesting to note that the excited state nuclear arrangement makes on average the bond chain *CC7-CC5-CC2-CC6-CC8* of the same length 1.42 Å, in the middle of a single and double bond value. The variations around the fluorinated cyclopentane are negligible, so that great part of the nuclear rearrangement involves the conjugated three rings system. As already mentioned, the depletion of electronic density on *CC1* bond, makes it more stretched in excited state (from average value of 1.55 Å in ground state to 1.60 Å in excited state).

The *CC1* bond is therefore more subject to break in excited state just as result of the new electronic arrangement. Figure 4.8 shows the time evolution of the *CC1* in both ground and excited state. Greater oscillations are observed in excited state, and the maximum value reached corresponds to a *CC* distance of 1.75 Å. As already shown for the energetic profiles in the precious section, the *CC* distance of 1.75 Å represents a threshold value in which the non-adiabatic coupling between the electronic states remains low. Beyond this, the electronic surfaces become too close

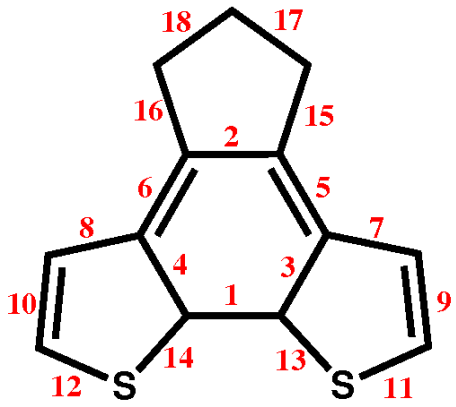

Fig. 4.7: Numeration used to tag the central moiety of F-CHD

Bond	GS (Å)	ES (Å)
CC1	1.55	1.60
CC2	1.47	1.42
CC3	1.54	1.52
CC4	1.54	1.52
CC5	1.37	1.42
CC6	1.37	1.42
CC7	1.45	1.42
CC8	1.45	1.42
CC9	1.37	1.40
CC10	1.37	1.40
CC11	1.77	1.76
CC12	1.77	1.76
CS13	1.87	1.84
CS14	1.87	1.84
CC15	1.51	1.50
CC16	1.51	1.50
CC17	1.56	1.56
CC18	1.56	1.56

Table 4.1: Main distanced (Å) averaged from the ground and excited state AIMD simulations

and a dynamical sampling based on a single reference electronic method would be no longer suitable. The excited state average values are computed on a trajectory that starting from the Franck-Condon region describes the nuclear relaxation, the fluctuations around the excited state minimum and the sampling of the barrier toward the CI (until a CC distance of 1.75 Å, but no further). The oscillations of the *CC* bond affect strongly the energetic gap between the ground and the first excited state. In Figure 4.8 the overlap between the excited state fluctuations of the *CC* distance and the S_0-S_1 energy difference is shown. The maxima of the energy difference (blue line) correspond to the minima of *CC* distance (red line) over the time. This means that the larger the *CC* distance, the smaller the energy gap between the electronic surfaces. The *CC1* oscillations with minima and maxima

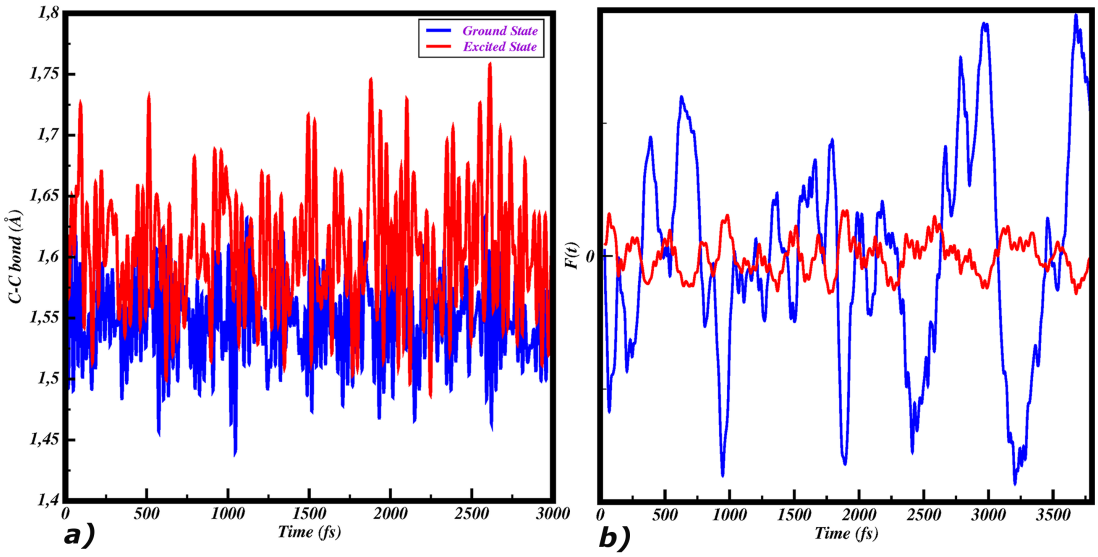

Fig. 4.8: a) Time evolution of the *CC1* distance in both ground (blue) and excited state(red). b) Comparison between the normalized fluctuactions of the *CC1* distance in excited state (red line) and the energy gap between the ground and excited state (blue line).

over the time, are associated to other nuclear motions, in particular to the modes of methyl groups on *CC1* bond.

In the closed ring specie, the methyl groups are basically perpendicular to the thiophenes ring plane. The open ring product is instead characterized by the methyl groups in the plane of thiophenes rings. The methyl wagging normal mode reports about this motion, and it was experimentally identified at the frequency of 191 cm^{-1} [134]. The 2D wavelet maps of the methyl wagging extracted by the excited state trajectory is shown in Figure 4.9. The time resolved band of the wagging wag is centered at 200 cm^{-1}, in fair agreement with the experimental one. The methyl wag is the low frequency mode recognized as coupled and modulating of the higher frequency modes localized on the central rings. These high frequency modes are:

CC stretching on cyclohexadiene ring (experimental frequency of 1181 cm^{-1}) [134], the *CC* stretching localized on thiophenes (exp 1333 cm^{-1}) and the *CCC* bending of cyclohexadiene and thiophenes (exp. 467 cm^{-1}). The corresponding wavelet 2D maps are reported in Figure 4.10, 4.11 and 4.12 respectively. Two kind of *CC* stretching are analyzed: the *CC* stretching on the central ring and on the thiophenes rings, with AIMD frequencies of 1186 cm^{-1} and 1380 cm^{-1} respectively. The wavelet maps of the two type of stretching (see Figure 4.10a and 4.11a) shows intensity and frequency oscillations over the time. In order to unveiling the coupling with the methyl wagging mode, a quantitative analysis of the time dependent frequencies is performed. In particular, the frequencies corresponding to the maximum intensity are extracted from the time resolved wavelet output (in Figure 4.10c and 4.11c). A discrete fourier transform is then performed on the oscillations of the maximum intensity in order to reveal the frequency ruling the oscillations. The discrete fourier transform of the time resolved maximum intensity associated to the *CC* stretching modes are shown in Figure 4.10d and 4.11d. In both cases, the FT shows that the main frequency modulating the intensity oscillation of the *CC* stretching mode is at 190 cm^{-1}, matching the methyl wags frequency.

The 2D wavelet maps of the *CCC* bending of the cyclohexadiene and thiophenes is quite complex (Figure 4.12a). The signal of interest is centered at the frequency of 469 cm^{-1} (AIMD frequency), but it is not the only contribution to the spectrum. The *CCC* bending involving cyclohexadiene and tiophenes ring participate to another

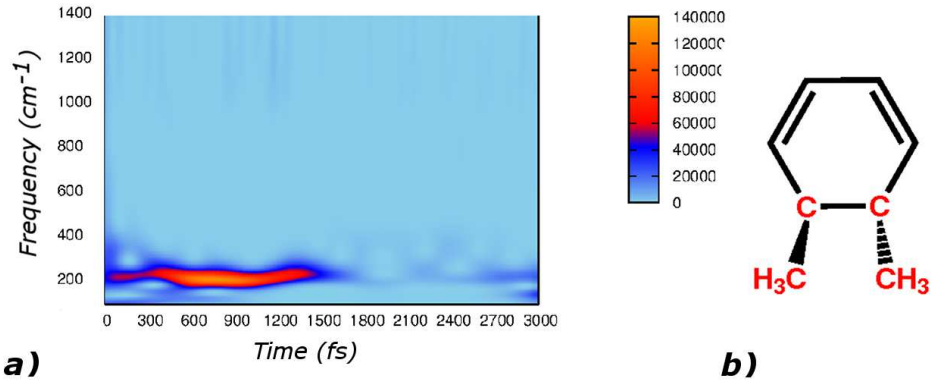

Fig. 4.9: a) 2D wavelet map of the methil wagging motion in excited state. b) Cyclohexadiene unity of F-CHD, with the atoms partecipating to the methil wag (AIMD Frequency 200 cm^{-1}) highlighted in red

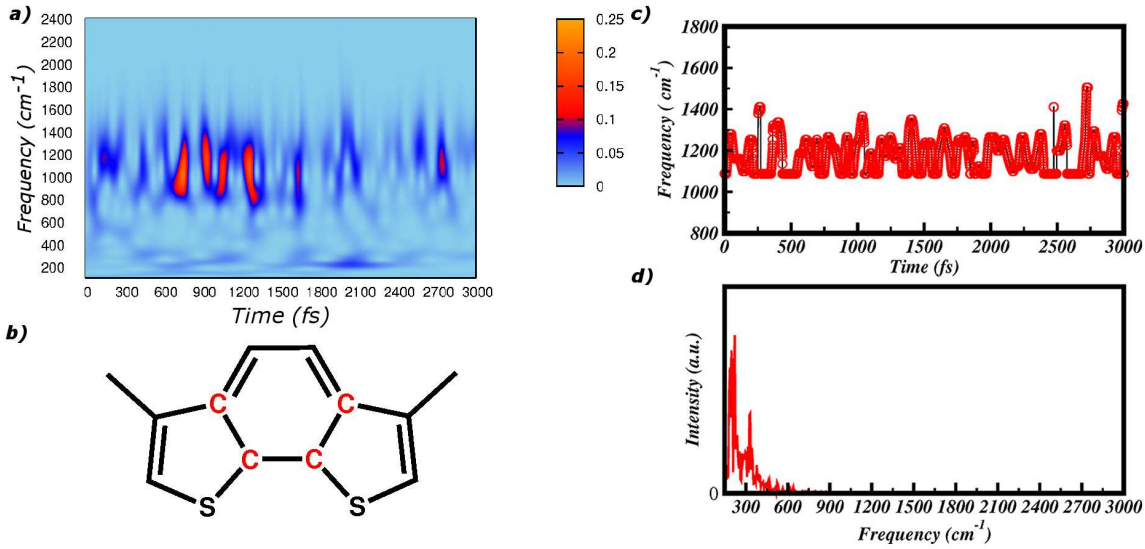

Fig. 4.10: a) 2D wavelet map of the *CC* stretching localized on cyclohexadiene unity. b) Atoms in red participate to the *CC* stratching (AIMD Frequency 1186 cm^{-1}). c) Oscillations of the frequencies correspondig to the maximum intensity over the time. d) Discrete Fouried Tranform of the intensity oscillation.

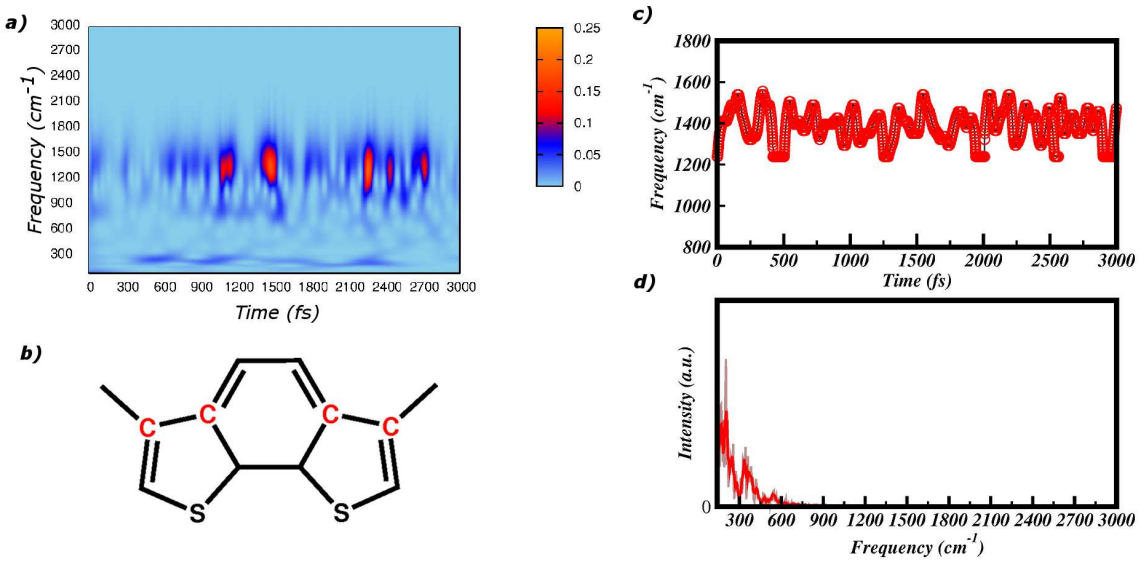

Fig. 4.11: a) 2D wavelet map of the *CC* stretching localized on thiophene rings. b) Atoms in red participate to the *CC* stratching (AIMD Frequency 1380 cm^{-1}) c) Oscillations of the frequencies correspondig to the maximum intensity over the time. d) Discrete Fouried Tranform of the intensity oscillation.

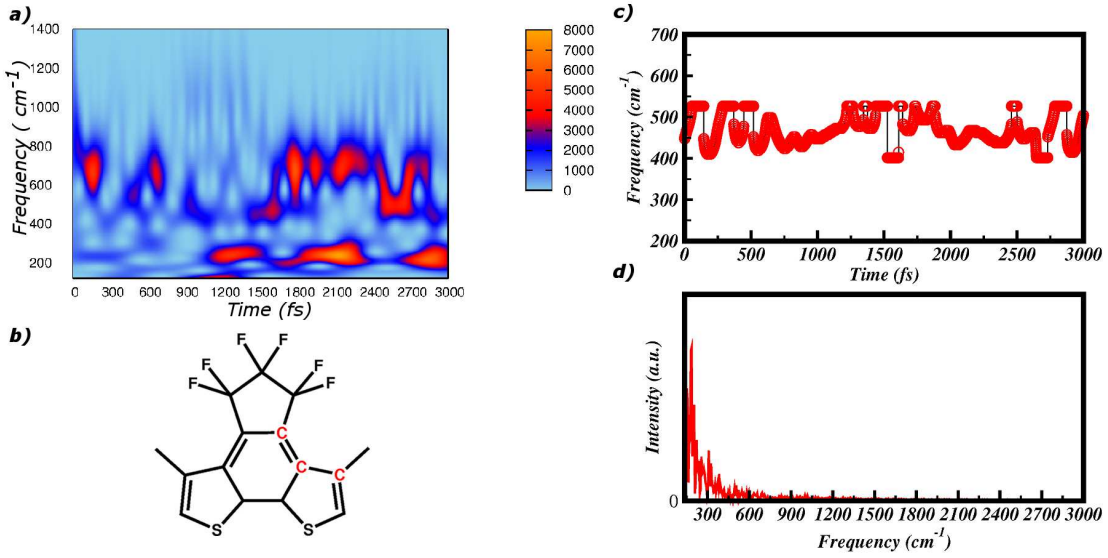

Fig. 4.12: a) 2D wavelet map of the *CCC* stretching localized on cyclohexadine and thiophene rings. b) Atoms in red participate to the *CCC* bending (AIMD Frequency 469 cm^{-1}) c) Oscillations of the frequencies correspondig to the maximum intensity over the time. d) Discrete Fouried Tranform of the intensity oscillation.

deformation mode at 690 cm^{-1}. Extracting a structural parameter from a trajectory and analyzing it in the frequency domain, allows to see all the vibration modes having it as component. In this case, the *CCC* bending is a component of both the vibrational modes at 469 cm^{-1} and 690 cm^{-1} and the wavelet map ends up to show both of them. In spite of the complexity, the wavelet map of the *CCC* bending has interesting features, because it shows also a contribution at about 200 cm^{-1}. Because the *CCC* bending does not participate to any modes around 200 cm^{-1}, the signal appears as result of the anharmonic coupling with the methyl wags. Moreover, the intensity oscillation corresponding to the frequency centered at 469 cm^{-1} are extracted and analyzed. The TF of the maximum intensity over the time (Figure 4.12d) shows the signal at 191 cm^{-1}, confirming the coupling with the methyl wags. Our findings are in agreement with the experimental evidences [134] of a coupling between the methyl wags (as modulating mode) and the *CC* stretching and *CCC* bending modes. The quantitative analysis of the time resolved bands has been applied for the first time and it has provided satisfactory results. The procedure will be definitely subject of improvements aiming in particular at the computation of the anharmonic constant.

Concluding remarks

The target of the Ph.D project was the development and the validation of an integrated computational protocol for the study of ultrafast dynamics in photochemistry. In particular, we have dealt with the simulation and the analysis of the nuclear dynamics induced by the photoexcitation, trying to reconstruct reaction mechanisms, with atomistic details and dynamical insight. Many efforts were devoted to combine ab-initio molecular dynamics scheme with a rational vibrational analysis. According to the adopted recipe, vibrational modes are defined from ab-initio dynamics trajectories, collected in both ground and excited state. This approach shows some advantages: 1) It opens up the possibility of getting vibrational information studying molecules in their realistic environment, such as chromophore in solution 2) The anharmonicity effects are naturally taken into account 3) we can extract time dependent functions, on which we can perform time resolved analysis by means of the wavelet transform. Moreover, in this work of thesis, the vibrational analysis procedure was extended to the study of nuclear relaxation induced by the photoexcitation. Indeed, for the first time, the wavelet transform was employed on vibrational modes defined by means of the excited state dynamics. The time resolved analy-

sis is definitely fundamental to the investigation of far-for equilibrium events, i.e. events having intrinsically a lifetime. For instance, in our case, the multiresolution wavelet analysis allows for recognize when and where vibrational modes rise and decay. This means that we can follow in real time how a photochemical reaction proceeds. The theoretical-computational procedure was applied and tested an two popular molecules, that find many applications in the photochemistry field: the photoacid pyranine molecule and a photochromic molecule belonging to the class of diarylethenes.

The main actor of the first part of the work was the 8-hydroxypyrene-1,3,6-trisulfonic acid or pyranine. Within the class of photoacids molecules, pyranine is classified as weak photoacid. The origin of pyranine photoreactivity cannot be simply interpreted and explained in terms of the electronic density redistribution responding to the external perturbation, but rather the subsequent nuclear dynamics turned out to be essential in promoting the ESPT reaction. Our findings support the idea that the nuclear photorelaxation of pyranine is finely controlled by the sequential activation of transient vibrational modes. Starting from the photoexcitation, the time window of 1 ps is a suitable time to watch the low frequency modes lifetime. All the modes have a quite complex composition, involving all the molecular skeleton. The wavelet maps reproduce the sequential activation of the main vibrational modes, in fair agreement with the experimental findings. The method employed is able to provide an accurate picture about the time evolution of the photoactivated vibrational

modes, matching in all cases the kinetics time constants of the experimental signals. Moreover, they have the key role of optimizing the structural arrangement with the hydrogen bonded water molecule. In particular, some low frequency modes such as the ring breathing mode (190 cm^{-1}), ring out of plane wagging (113 cm^{-1}) or the ring deformation mode (280 cm^{-1}) are involved in modulation of intermolecular distances and orientation with the water solvent molecule hydrogen bonded to phenolic group of pyranine.

HPTS chromophore is very sensitive to the environment, and if a base like acetate is present in water solution the reaction became faster (sub-ps). Depending on the acetate concentration, different ESPT mechanisms can be modelled, in particular a direct ESPT reaction from pyranine to acetate is promoted at high concentration of acetate base. Otherwise, one or more intervening water molecules can directly modulate the proton hop from pyranine to acetate. The direct ESPT reaction from pyranine to acetate occurs in sub-ps time scale and it strictly depends on the choice of the starting point. In particular, the solvation around the phenolic oxygen of pyranine and relative orientation of pyranine-acetate are the two factors that strongly affect the ESPT kinetic. The excited state proton transfer reaction involving the pyranine-water-acetate cluster is an intermediate situation between pyranine in pure water and pyranine-acetate. In the first case, before the ESPT event the sequential activation of low frequencies vibrational modes is necessary to induce a structural optimization between the proton donor-acceptor pair. On the

other hand for what regards the pyranine-acetate system the reaction is basically barrierless and the nuclear rearrangement is not required. The presence of acetate, for the pyranine-water-acetate cluster, obviously makes the ESPT faster, but the central water suggests that low frequencies skeleton modes have to optimize as well the structural arrangement of the reactive site. Ring breathing and out of plane wagging modes have been identified and recognized again as a key modes coupled to the motion of hydrogen bonded water molecule.

In the last part of the work, the time resolved analysis was extended and tested to study the anharmonic coupling between vibrational modes. The case study is represented by a diarylethenes photochromic molecule, that in excited state undergoes an opening ring reaction. The characteristic intensity oscillations of some vibrational signals appear clearly in the wavelet maps. This suggests an anharmonic coupling with some low frequency modes. In particular, we found that the coupling between high and low frequency modes localized on the central cyclohexadiene ring would promote the opening reaction. The quantitative analysis of the time resolved bands has been applied here for the first time, providing satisfactory results. It is a promising approach, that can be further improved, in particular for the calculations of anharmonic constants.

We presented a theoretical-computational procedure that allows for the simulation and investigation at atomistic level of complex photoinduced reactions on the time scale of nuclear motions. It makes possible to follow in real time the nuclear

dynamics in terms of vibrational modes, allowing a direct comparison with the experiments of time resolved time resolved vibrational spectroscopy. The vibrational analysis associated to the ab-initio molecular dynamics scheme has given excellent results, in fair agreement with experimental data. It could be very promising in supporting the advanced time resolved spectroscopic techniques. In next step, the quantitative analysis of the time resolved vibrational bands of the wavelet maps, could be extended and improved. For example, it could be interesting to understand how the coupling between vibrational modes changes over the time or from the ground to excited state surface. In general, the anharmonicity provides information about the shape of the PES(s) and it is essential to improve our knowledge about the structure/reactivity of the molecules.

Appendix A

Pyranine Dynamics: Computational details

The pyranine solute was located at the center of a water molecules sphere of a radius 19 Å; the structureless solvent surrounding the explicit sphere completes the hybrid explicit/implicit solvation model. Non periodic boundary conditions accounts for the interactions between the explicit molecular system and the implicit bulk solvent with both the electrostatic and dispersion-repulsion interactions [125–127]. The solvent molecules are explicitely represented by the TIP3P water model [148], while the implicit bulk solvent by the polarizable continuum model, in conductor-like version (C-PCM) [149, 150]. The explicit system itself is treated at different levels of theory according to the hybrid QM/MM ONIOM extrapolation scheme [45, 46]. In particular, the pyranine molecule is described by DFT and TD-DFT [41] in the ground and S_1 excited state, respectively, by adopting the global hybrid B3LYP [151–153] functional and the 6-31g(d,p) basis set. The so- built energy potential ruled the AIMD simulations in both ground and excited state. The ground state sampling was performed by means of the atom-centered density matrix propagation (ADMP) method [91]. After 5 ps of equilibration, the trajectory was collected for

10 ps with a time step of 0.2 fs. From the ground state trajectory, a configuration representative of the equilibrium was chosen as starting point of the excited state dynamics. In order to collect an excited state trajectory a Born-Oppenheimer ab-initio dynamics [83] was instead employed, where the excited state energies and gradients were calculated on-the-fly by linear response TD-DFT formalism.

The same level of theory and dynamics scheme were employed for modeling the direct pyranine-acetate and modulated pyranine-water system. The only difference is that the QM region is defined by pyranine and acetate and pyranine, water and acetate molecules respectively. In case of the pyranine-water-acetate cluster the QM/MM partition was extended for collecting the excited state trajectory. In particular four excited state trajectory include one, two, three and five solvent water molecules in addition to the QM cluster of the ground state. All the calculations were carried out with the Gaussian program suite.

F-CHD Dynamics: Computational details

F-CHD was treated at density functional theory level, adopting the global hybrid functional B3LYP [151–153], in combination with the 6-31g(d,p) basis set. The excited state potential energy surface was explored by the time-dependent DFT (TD-DFT) at the same level of theory. The ground state sampling was performed by means of the atom-centered density matrix propagation (ADMP) method [91]. After 2 ps of equilibration, the trajectory was collected for 5 ps with a time step of 0.2 fs. From the ground state trajectory, a configuration representative of the

equilibrium was chosen as starting point of the excited state propagation according to the BOMD/TD-DFT [83] dynamics scheme.

List of Figures

List of Tables

Bibliography

[1] V. Balzani, P. Ceroni, and A. Juris, *Photochemistry and Photophysics: Concepts, Research, Applications* (John Wiley & Sons, 2014).

[2] V. Balzani, A. Credi, and M. Venturi, ChemSusChem **1** (1-2), 26 (2008).

[3] V. Balzani, Photochem. Photobiol. Sci. **2** (5), 459 (2003).

[4] R. Improta, F. Santoro, and L. Blancafort, Chem. Rev. **116** (6), 3540 (2016).

[5] M. R. Wasielewski, Chem. Rev. **92** (3), 435 (1992).

[6] S. Dadashi-Silab, S. Doran, and Y. Yagci, Chem. Rev. **116** (17), 10212 (2016).

[7] G. Bergamini and S. Silvi, *Applied Photochemistry: When Light Meets Molecules*, vol. 92 (Springer, 2016).

[8] M. Natali and F. Scandola, in *Applied Photochemistry* (Springer, 2016), pp. 1–66.

[9] A. W. Jasper, C. Zhu, S. Nangia, and D. G. Truhlar, Faraday Discuss. **127**, 1 (2004).

[10] C. Xie, J. Ma, X. Zhu, D. R. Yarkony, D. Xie, and H. Guo, J. Am. Chem. Soc **138** (25), 7828 (2016).

[11] M. Ben-Nun and T. J. Martınez, J. Chem. Phys. **108** (17), 7244 (1998).

[12] K. Ramasesha, S. R. Leone, and D. M. Neumark, Annu. Rev. Phys. Chem. **67**, 41 (2016).

[13] H. Zhu, Y. Yang, K. Wu, and T. Lian, Annu. Rev. Phys. Chem. **67**, 259 (2016).

[14] F. Calegari, D. Ayuso, A. Trabattoni, L. Belshaw, S. De Camillis, S. Anumula, F. Frassetto, L. Poletto, A. Palacios, P. Decleva *et al.*, Science **346** (6207), 336 (2014).

[15] N. L. Gruenke, M. F. Cardinal, M. O. McAnally, R. R. Frontiera, G. C. Schatz, and R. P. Van Duyne, Chem. Soc. Rev. **45** (8), 2263 (2016).

[16] M. D. Fayer, *Ultrafast Infrared Vibrational Spectroscopy* (CRC Press, 2013).

[17] M. Thämer, L. De Marco, K. Ramasesha, A. Mandal, and A. Tokmakoff, Science **350** (6256), 78 (2015).

[18] A. A. Hassanali, J. Cuny, V. Verdolino, and M. Parrinello, Philos. Trans. R. Soc., A **372** (2011), 20120482 (2014).

[19] J. C. Tully, J. Chem. Phys. **93** (2), 1061 (1990).

[20] J. Tully, Faraday Discuss. **110**, 407 (1998).

[21] R. R. Frontiera and R. A. Mathies, Laser Photonics Rev. **5** (1), 102 (2011).

[22] P. Kukura, D. W. McCamant, S. Yoon, D. B. Wandschneider, and R. A. Mathies, Science **310** (5750), 1006 (2005).

[23] P. Kukura, D. W. McCamant, and R. A. Mathies, Annu. Rev. Phys. Chem. **58**, 461 (2007).

[24] D. R. Dietze and R. A. Mathies, ChemPhysChem. **17** (9), 1224 (2016).

[25] S.-Y. Lee, D. Zhang, D. W. McCamant, P. Kukura, and R. A. Mathies, J. Chem. Phys. **121** (8), 3632 (2004).

[26] C. Fang, R. R. Frontiera, R. Tran, and R. A. Mathies, Nature **462** (7270), 200 (2009).

[27] M. Ormo, A. B. Cubitt, K. Kallio, and L. A. Gross, Science **273** (5280), 1392 (1996).

[28] A. Petrone, P. Caruso, S. Tenuta, and N. aega, Phys. Chem. Chem. Phys. **15** (47), 20536 (2013).

[29] M. Di Donato, L. J. van Wilderen, I. H. Van Stokkum, T. C. Stuart, J. T. Kennis, K. J. Hellingwerf, R. van Grondelle, and M. L. Groot, Phys. Chem. Chem. Phys. **13** (36), 16295 (2011).

[30] A. Petrone, P. Cimino, G. Donati, H. P. Hratchian, M. J. Frisch, and N. Rega, J. Chem. Theory Comput. **12** (10), 4925 (2016).

[31] D. P. Hoffman, S. R. Ellis, and R. A. Mathies, J. Phys. Chem. A **118** (27), 4955 (2014).

[32] S.-H. Shim, D. B. Strasfeld, Y. L. Ling, and M. T. Zanni, Proc. Natl. Acad. Sci. USA **104** (36), 14197 (2007).

[33] P. Mukherjee, I. Kass, I. T. Arkin, and M. T. Zanni, Proc. Natl. Acad. Sci. USA **103** (10), 3528 (2006).

[34] M. Khalil, N. Demirdöven, and A. Tokmakoff, J. Phys. Chem. A **107** (27), 5258 (2003).

[35] J. A. Fournier, W. Carpenter, L. De Marco, and A. Tokmakoff, J. Am. Chem. Soc. **138** (30), 9634 (2016).

[36] M. Ben-Nun, J. Quenneville, and T. J. Martínez, J. Phys. Chem. A **104** (22), 5161 (2000).

[37] J. D. Coe, B. G. Levine, and T. J. Martínez, J. Phys. Chem. A **111** (44), 11302 (2007).

[38] H. R. Hudock, B. G. Levine, A. L. Thompson, H. Satzger, D. Townsend, N. Gador, S. Ullrich, A. Stolow, and T. J. Martinez, J. Phys. Chem. A **111** (34), 8500 (2007).

[39] H. Langer, N. L. Doltsinis, and D. Marx, ChemPhysChem **6** (9), 1734 (2005).

[40] C. Jamorski, M. E. Casida, and D. R. Salahub, J. Chem. Phys. **104** (13), 5134 (1996).

[41] E. Runge and E. K. Gross, Phys. Rev. Lett. **52** (12), 997 (1984).

[42] M. Cossi and V. Barone, J. Chem. Phys. **115** (10), 4708 (2001).

[43] M. Martinez, M.-P. Gaigeot, D. Borgis, and R. Vuilleumier, J. Chem. Phys. **125** (14), 144106 (2006).

[44] N. Rega, G. Brancato, A. Petrone, P. Caruso, and V. Barone, J. Chem. Phys. **134** (7), 074504 (2011).

[45] T. Vreven, K. S. Byun, I. Komáromi, S. Dapprich, J. A. Montgomery Jr, K. Morokuma, and M. J. Frisch, J. Chem. Theory Comput. **2** (3), 815 (2006).

[46] M. Svensson, S. Humbel, R. D. Froese, T. Matsubara, S. Sieber, and K. Morokuma, J. Phys. Chem. **100** (50), 19357 (1996).

[47] M. Farge, N. Kevlahan, V. Perrier, and K. Schneider, Wavelets in Physics pp. 117–200 (1999).

[48] A. Petrone, G. Donati, P. Caruso, and N. Rega, J. Am. Chem. Soc. **136** (42), 14866 (2014).

[49] G. Donati, D. B. Lingerfelt, A. Petrone, N. Rega, and X. Li, J. Phys. Chem. A **120** (37), 7255 (2016).

[50] N. Agmon, D. Huppert, A. Masad, and E. Pines, J. Phys. Chem. **95** (25), 10407 (1991).

[51] M. Rini, B.-Z. Magnes, E. Pines, and E. T. Nibbering, Science **301** (5631), 349 (2003).

[52] H.-S. Chou, M.-H. Hsiao, W.-Y. Hung, T.-Y. Yen, H.-Y. Lin, and D.-M. Liu, J. Mater. Chem. B **2** (38), 6580 (2014).

[53] G. Panzarasa, A. Osypova, C. Toncelli, M. T. Buhmann, M. Rottmar, Q. Ren, K. Maniura-Weber, R. M. Rossi, and L. F. Boesel, Sens. Actuators, B **249**, 156 (2017).

[54] M. Schäferling, T. Lang, and A. Schnettelker, J. Lumin. **154**, 458 (2014).

[55] O. F. Mohammed, D. Pines, J. Dreyer, E. Pines, and E. T. Nibbering, Science **310** (5745), 83 (2005).

[56] T.-H. Tran-Thi, T. Gustavsson, C. Prayer, S. Pommeret, and J. T. Hynes, Chem. Phys. Lett. **329** (5), 421 (2000).

[57] R. Simkovitch, S. Shomer, R. Gepshtein, and D. Huppert, J. Phys. Chem. B **119** (6), 2253 (2014).

[58] F. Han, W. Liu, and C. Fang, Chem. Phys. **442**, 204 (2013).

[59] W. Liu, L. Tang, B. G. Oscar, Y. Wang, C. Chen, and C. Fang, J. Phys. Chem. Lett. **8** (5), 997 (2017).

[60] B. G. Oscar, W. Liu, N. D. Rozanov, and C. Fang, Phys. Chem. Chem. Phys. **18** (37), 26151 (2016).

[61] W. Liu, F. Han, C. Smith, and C. Fang, J. Phys. Chem. B **116**, 10535 (2012).

[62] M. Irie and K. Uchida, Bulletin of the Chemical Society of Japan **71** (5), 985 (1998).

[63] M. Irie, O. Miyatake, and K. Uchida, J. Am. Chem. Soc. **114** (22), 8715 (1992).

[64] C. Wiebeler, C. A. Bader, C. Meier, and S. Schumacher, Phys. Chem. Chem. Phys. **16** (28), 14531 (2014).

[65] B. O. Roos, P. R. Taylor, P. E. Si *et al.*, Chem. Phys. **48** (2), 157 (1980).

[66] B. O. Roos, Advances in Chemical Physics: Ab Initio Methods in Quantum Chemistry Part 2, Volume 69 pp. 399–445 (2007).

[67] I. Tavernelli, U. F. Röhrig, and U. Rothlisberger, Mol. Phys. **103** (6-8), 963 (2005).

[68] E. Tapavicza, I. Tavernelli, and U. Rothlisberger, Phys. Rev. Lett. **98** (2), 023001 (2007).

[69] S. Hammes-Schiffer and J. C. Tully, J. Chem. Phys. **101** (6), 4657 (1994).

[70] P. V. Parandekar and J. C. Tully, J. Chem. Phys. **122** (9), 094102 (2005).

[71] A. D. MacKerell, N. Banavali, and N. Foloppe, Biopolymers **56** (4), 257 (2000).

[72] V. Hornak, R. Abel, A. Okur, B. Strockbine, A. Roitberg, and C. Simmerling, Proteins: Struct., Funct., Bioinf. **65** (3), 712 (2006).

[73] J. Wang, R. M. Wolf, J. W. Caldwell, P. A. Kollman, and D. A. Case, J. Comput. Chem. **25** (9), 1157 (2004).

[74] W. D. Cornell, P. Cieplak, C. I. Bayly, I. R. Gould, K. M. Merz, D. M. Ferguson, D. C. Spellmeyer, T. Fox, J. W. Caldwell, and P. A. Kollman, J. Am. Chem. Soc. **117** (19), 5179 (1995).

[75] D. Marx and J. Hutter, Modern methods and algorithms of quantum chemistry **1** (301-449), 141 (2000).

[76] D. Marx and J. Hutter, *Ab initio molecular dynamics: basic theory and advanced methods* (Cambridge University Press, 2009).

[77] R. G. Parr and W. Yang, *Density-functional theory of atoms and molecules*, vol. 16 (Oxford university press, 1989).

[78] N. C. Handy, in *Quantum Mechanical Simulation Methods for Studying Biological Systems* (Springer, 1996), pp. 1–35.

[79] W. Koch and M. C. Holthausen, *A chemist's guide to density functional theory* (John Wiley & Sons, 2015).

[80] X. Li, J. C. Tully, H. B. Schlegel, and M. J. Frisch, J. Chem. Phys. **123** (8), 084106 (2005).

[81] C. M. Isborn, X. Li, and J. C. Tully, J. Chem. Phys. **126** (13), 134307 (2007).

[82] W. Liang, C. M. Isborn, A. Lindsay, X. Li, S. M. Smith, and R. J. Levis, J. Phys. Chem. A **114** (21), 6201 (2010).

[83] R. N. Barnett and U. Landman, Phys. Rev. B **48** (4), 2081 (1993).

[84] X. Li and H. B. Schlegel, J. Phys. Chem. A **108** (3), 468 (2004).

[85] U. Raucci, M. Savarese, C. Adamo, I. Ciofini, and N. Rega, J. Phys. Chem. B **119** (6), 2650 (2015).

[86] R. Car and M. Parrinello, Phys. Rev. lett. **55** (22), 2471 (1985).

[87] M. E. Tuckerman and M. Parrinello, J. Chem. Phys. **101** (2), 1302 (1994).

[88] D. Marx, M. E. Tuckerman, J. Hutter, and M. Parrinello, Nature **397** (6720), 601 (1999).

[89] M. E. Tuckerman, D. Marx, M. L. Klein, and M. Parrinello, Science **275** (5301), 817 (1997).

[90] H. B. Schlegel, J. M. Millam, S. S. Iyengar, G. A. Voth, A. D. Daniels, G. E. Scuseria, and M. J. Frisch, J. Chem. Phys. **114** (22), 9758 (2001).

[91] S. S. Iyengar, H. B. Schlegel, J. M. Millam, G. A. Voth, G. E. Scuseria, and M. J. Frisch, J. Chem. Phys. **115** (22), 10291 (2001).

[92] H. B. Schlegel, S. S. Iyengar, X. Li, J. M. Millam, G. A. Voth, G. E. Scuseria, and M. J. Frisch, J. Chem. Phys. **117** (19), 8694 (2002).

[93] S. S. Iyengar, H. B. Schlegel, G. A. Voth, J. M. Millam, G. E. Scuseria, and M. J. Frisch, Isr. J. Chem. **42** (2-3), 191 (2002).

[94] N. Rega, S. S. Iyengar, G. A. Voth, H. B. Schlegel, T. Vreven, and M. J. Frisch, J. Phys. Chem. B **108** (13), 4210 (2004).

[95] R. E. Stratmann, G. E. Scuseria, and M. J. Frisch, J. Chem. Phys. **109** (19), 8218 (1998).

[96] M. E. Casida and M. Huix-Rotllant, Annu. Rev. Phys. Chem. **63**, 287 (2012).

[97] M. E. Casida and T. A. Wesołowski, Int. J. Quantum Chem. **96** (6), 577 (2004).

[98] M.-P. Gaigeot, M. Martinez, and R. Vuilleumier, Mol. Phys. **105** (19-22), 2857 (2007).

[99] P. Carbonniere, A. Dargelos, I. Ciofini, C. Adamo, and C. Pouchan, Phys. Chem. Chem. Phys. **11** (21), 4375 (2009).

[100] B. R. Brooks, D. Janežič, and M. Karplus, J. Comput. Chem. **16** (12), 1522 (1995).

[101] T. Ichiye and M. Karplus, Proteins: Struct., Funct., and Bioinf. **11** (3), 205 (1991).

[102] N. Rega, Theor. Chem. Acc. **116** (1-3), 347 (2006).

[103] A. Strachan, J. Chem. Phys. **120** (1), 1 (2004).

[104] C. Torrence and G. P. Compo, Bull. Am.. Meteorol. Soc. **79** (1), 61 (1998).

[105] M. Farge, Annu. Rev. Fluid Mech. **24** (1), 395 (1992).

[106] O. Rioul and M. Vetterli, IEEE Signal Processing Magazine **8** (4), 14 (1991).

[107] M. Pagliai, F. Muniz-Miranda, G. Cardini, R. Righini, and V. Schettino, J. Mol. Struct. **993** (1), 438 (2011).

[108] F. Muniz-Miranda, M. Pagliai, G. Cardini, and V. Schettino, J. Chem. Theory Comput. **7** (4), 1109 (2011).

[109] H. Weng and K. Lau, J. Atmos. Sci. **51** (17), 2523 (1994).

[110] I. Daubechies, IEEE Trans. Inform. Theory **36** (5), 961 (1990).

[111] L. M. Tolbert and K. M. Solntsev, Acc. Chem. Res. **35** (1), 19 (2002).

[112] S. J. Formosinho and L. G. Arnaut, J. Photochem. Photobiol. A **75** (1), 21 (1993).

[113] E. Pines, D. Huppert, and N. Agmon, J. Chem. Phys. **88** (9), 5620 (1988).

[114] P. Leiderman, L. Genosar, and D. Huppert, J. Phys. Chem. A **109** (27), 5965 (2005).

[115] N. Agmon, Chem. Phys. Lett. **244** (5), 456 (1995).

[116] B. J. Siwick and H. J. Bakker, J. Am. Chem. Soc. **129** (44), 13412 (2007).

[117] J. T. Hynes, T.-H. Tran-Thi, and G. Granucci, J. Photochem. Photobiol. A **154** (1), 3 (2002).

[118] J. L. Pérez-Lustres, F. Rodriguez-Prieto, M. Mosquera, T. A. Senyushkina, N. P. Ernsting, and S. A. Kovalenko, J. Am. Chem. Soc. **129**, 5408 (2007).

[119] O. F. Mohammed, J. Dreyer, B.-Z. Magnes, E. Pines, and E. T. Nibbering, ChemPhysChem **6** (4), 625 (2005).

[120] M. J. Cox, R. L. Timmer, H. J. Bakker, S. Park, and N. Agmon, J. Phys. Chem. A **113** (24), 6599 (2009).

[121] R. Simkovitch, S. Shomer, R. Gepshtein, D. Shabat, and D. Huppert, J. Phys. Chem. A **118** (10), 1832 (2014).

[122] R. Simkovitch, S. Shomer, R. Gepshtein, M. E. Roth, D. Shabat, and D. Huppert, J. Photochem. Photobiol. A **277**, 90 (2014).

[123] Y. Wang, W. Liu, L. Tang, B. Oscar, F. Han, and C. Fang, J. Phys. Chem. A **117**, 6024 (2013).

[124] W. Liu, Y. Wang, L. Tang, B. G. Oscar, L. Zhu, and C. Fang, Chem. Sci. **7** (8), 5484 (2016).

[125] G. Brancato, N. Rega, and V. Barone, J. Chem. Phys. **125** (16), 164515 (2006).

[126] G. Brancato, N. Rega, and V. Barone, J. Chem. Phys. **128** (14), 144501 (2008).

[127] N. Rega, G. Brancato, and V. Barone, Chem. Phys. Lett. **422** (4), 367 (2006).

[128] H. Tian and S. Yang, Chemical Society Reviews **33** (2), 85 (2004).

[129] M. Irie, *Photochromism: Memories and Switches Introduction* (2000).

[130] S. H. Bhoo, T. Hirano, H.-Y. Jeong, J.-G. Lee, M. Furuya, and P.-S. Song, J. Am. Chem. Soc. **119** (48), 11717 (1997).

[131] C. Yun, J. You, J. Kim, J. Huh, and E. Kim, J. Photochem. Photobiol., C **10** (3), 111 (2009).

[132] M. Morimoto and M. Irie, J. Am. Chem. Soc. **132** (40), 14172 (2010).

[133] M. Irie, Photochem. Photobiol. Sci. **9** (12), 1535 (2010).

[134] D. T. Valley, D. P. Hoffman, and R. A. Mathies, Phys. Chem. Chem. Phys. **17** (14), 9231 (2015).

[135] M. Boggio-Pasqua, M. Ravaglia, M. J. Bearpark, M. Garavelli, and M. A. Robb, J. Phys. Chem. A **107** (50), 11139 (2003).

[136] C. L. Ward and C. G. Elles, J. Phys. Chem. A **118** (43), 10011 (2014).

[137] Y. Ishibashi, T. Umesato, M. Fujiwara, K. Une, Y. Yoneda, H. Sotome, T. Katayama, S. Kobatake, T. Asahi, M. Irie *et al.*, J. Phys. Chem. C **120** (2), 1170 (2016).

[138] H. Sotome, T. Nagasaka, K. Une, C. Okui, Y. Ishibashi, K. Kamada, S. Kobatake, M. Irie, and H. Miyasaka, J. Phys. Chem. Lett. **8** (14), 3272 (2017).

[139] A. Perrier, S. Aloise, M. Olivucci, and D. Jacquemin, J. Phys. Chem. Lett. **4** (13), 2190 (2013).

[140] D. Mendive-Tapia, A. Perrier, M. J. Bearpark, M. A. Robb, B. Lasorne, and D. Jacquemin, Phys. Chem. Chem. Phys. **16** (34), 18463 (2014).

[141] P. Celani, S. Ottani, M. Olivucci, F. Bernardi, and M. A. Robb, J. Am. Chem. Soc. **116** (22), 10141 (1994).

[142] M. Olivucci, F. Bernardi, P. Celani, I. Ragazos, and M. A. Robb, J. Am. Chem. Soc. **116** (3), 1077 (1994).

[143] R. Send and F. Furche, J. Chem. Phys. **132** (4), 044107 (2010).

[144] H. B. Schlegel and M. A. Robb, Chem. Phys. Lett. **93** (1), 43 (1982).

[145] E. D. Glendening, C. R. Landis, and F. Weinhold, Wiley interdisciplinary reviews: computational molecular science **2** (1), 1 (2012).

[146] M. A. Robb, Conical Intersections: Theory, Computation and Experiment **17**, 1 (2011).

[147] M. J. Bearpark, M. A. Robb, and H. B. Schlegel, Chem. Phys. Lett. **223** (3), 269 (1994).

[148] Y. Sun and P. A. Kollman, J. Comput. Chem. **16** (9), 1164 (1995).

[149] M. Cossi, N. Rega, G. Scalmani, and V. Barone, J. Comput. Chem. **24** (6), 669 (2003).

[150] M. Cossi, G. Scalmani, N. Rega, and V. Barone, J. Chem. Phys. **117** (1), 43 (2002).

[151] A. D. Becke, J. Chem. Phys. **96** (3), 2155 (1992).

[152] A. D. Becke, Phys. Rev. A **38** (6), 3098 (1988).

[153] A. D. Becke, J. Chem. Phys. **98** (2), 1372 (1993).